Impact strength of Friction Stir Weld-bonded joints

Bruno Miguel Doutel Figueira

Thesis to obtain the Master of Science Degree in

Mechanical Engineering

Supervisors: Prof. Virgínia Isabel Monteiro Nabais Infante

Dr. Daniel Filipe Oliveira Braga

Examination Committee

Chairperson: Prof. Luís Filipe Galrão dos Reis

Supervisor: Dr. Daniel Filipe Oliveira Braga

Member of the Committee: Dr. Pedro Miguel Guimarães Pires Moreira

May 2020

Acknowledgments

I would like to thank Prof. Virgínia Infante and Dr. Daniel F.O. Braga for the continuous availability and support given throughout this project.

Secondly to Eng. Ricardo Maciel for his constant support throughout this study and to Eng. Tiago Bento for his support in the manufacturing of the FSW and Hybrid joints.

Furthermore to Prof. Pedro Rosa and Eng. Pedro Santos for their availability to build a testing apparatus and to perform the necessary experimental work for the impact experiments.

I would also to thank to the Manufacturing and Process Technology Laboratory and to the Machining and Micromanufacturing Laboratory for the space availability to manufacture and perform the tests, respectively. Also, a thank you to the various laboratory technicians at IST that help to surpass the obstacles found along the away.

To the Formula Student Team (FST Lisboa) for providing some of the materials needed for the manufacturing of the adhesive joints at IST.

Lastly, I would like to express my sincere gratitude to my family, especially my father, my stepmother and my two sisters, for the all the support given along this journey.

RESUMO

A indústria dos transportes está constantemente à procura de novas soluções tecnológicas economicamente viáveis que visam a redução das emissões de poluentes e consumo de combustível. Uma das formas de atingir estes objetivos passa pela utilização de materiais mais leves como as ligas de alumínio. No entanto, estes materiais apresentam uma soldabilidade reduzida, o que leva à procura de novos processos de ligação que visam colmatar este problema. A Soldadura por Fricção Linear (SFL) é uma possível solução para obter juntas de elevada qualidade sem comprometer em demasia as propriedades mecânicas comparativamente ao material base, em juntas de topo-a-topo. No entanto, quando estas são utilizadas na configuração sobreposta, assiste-se a uma redução considerável das suas propriedades. Uma possível solução para ultrapassar este problema e melhorar o desempenho mecânico destas juntas pode ser conseguida através da combinação de SFL com adesivos estruturais. Neste estudo, três tipos de juntas distintos (SFL, adesivas e híbridas) foram produzidas, tendo como um dos objetivos estudar o seu desempenho mecânico em ensaios de tração e de impacto. Modelos numéricos foram também desenvolvidos de modo a prever o comportamento mecânico de cada junta sob as solicitações estudadas previamente. Em carregamentos quási-estáticos juntas híbridas apresentaram melhorias significativas em comparação com as juntas SFL. Contudo, juntas adesivas continuam a apresentar o melhor desempenho mecânico. Contribuição do adesivo nos ensaios de impacto nas juntas híbridas aumenta significativamente a absorção da energia proveniente do impacto em comparação com as juntas SFL, chegando a alterar o modo de fratura da junta.

Palavras-chave: Soldadura por Fricção Linear, Ligação híbrida, Juntas sobrepostas, Altas taxas de deformação, Modelação numérica

Abstract

The transport industry is constantly in search of new economically viable technological solutions aimed at reducing pollutant emissions and fuel consumption. One way to achieve these goals is to use lighter materials such as aluminium alloys. However, these materials have a reduced weldability, which leads to the search for new joining processes that aim to solve this problem. Friction Stir Welding (FSW) is a possible solution to achieve high quality joints without compromising significantly their mechanical properties when compared to the base material, for a butt joint configuration. However, when this technology is used in the overlap configuration, their properties are considerably reduced. In order to overcome this problem and improve the mechanical performance of these joints, a combination of FSW and adhesive is made. In this study, three different types of joints, using FSW, Adhesive Bonding (AB) and Friction Stir Weld-Bonding (FSWB), were produced. These joints were later studied in tensile and impact tests, to assess their mechanical performance at different loading rates. Numerical models were also developed in order to predict the mechanical behaviour of each joint under the previously studied loading. Hybrid joints showed significant improvements in comparison to the FSW joints when subjected to quasi-static loadings. Despite this, adhesive joints continue to perform better in general. In impact loadings, adhesive present on the Hybrid joints significantly increases the capacity to absorb the energy from the impact in comparison to the FSW joints, changing the fracture mode of the joint.

Keywords: Friction Stir Welding, Hybrid joining, Friction Stir Weld-bonding, Lap joining, High strain rate, Numerical modelling

Table of Contents

List of Figures

List of Tables

Acronyms and symbols

Acronyms

AA	Aluminium Alloy
AB	Adhesive Bonding
AC	Alternate Current
AS	Advancing Side
AWB	Adhesive Weld-Bonding
A-PFFSR	Active-Passive Filling Friction Stir Repairing
BM	Base Material
CAA	Chromic Acid Anodization
CAR	Center for Automotive Research
CTE	Coefficient of Thermal Expansion
CZM	Cohesive Zone Modelling
DC	Direct Current
DCB	Double Cantilever Beam
DoE	Design of Experiments
DIC	Digital Image Correlation
DLJ	Double Lap Joint
DW	Drop-Weight
ENF	End Notch Flexure
EST	Effective Sheet Thickness
FAA	Federal Aviation Administration
FEM	Finite Element Modelling
FSSW	Friction Stir Spot Welding
FSW	Friction Stir Welding
FSWB	Friction Stir Weld-Bonding
GTN	Gurson-Tvergaard-Needleman model
HAZ	Heat Affected Zone
HRSW	Hybrid Resistance Spot Welding
INEGI	Institute of Science and Innovation in Mechanical and Industrial Engineering
IST	Instituto Superior Técnico

LBW	Laser Beam Welding
LVDT	Linear Variable Differential Transformer
MIG	Metal Inert Gas
MPW	Magnetic Pulse Welding
NASA	National Aeronautics and Space Administration
NDT	Non-Destructive Technique
PAA	Phosphoric Acid Anodization
PAW	Plasma Arc Welding
PR	Pop Rifting
RS	Retreating Side
RSW	Resistance Spot Welding
SZ	Stir Zone
SAA	Sulfuric Acid Anodization
SHPB	Split Hopkinson Pressure Bar
SHTB	Split Hopkinson Tension Bar
SLJ	Single Lap Joint
SPR	Self-Piercing Rifting
TAST	Through Adherent Shear Test
TEM	Transmission Electron Microscopy
TMAZ	Thermo-Mechanical Affected Zone
TWB	Tailor Welded Blank
TWI	The Welding Institute
UTS	Ultimate Tensile Strength

Symbols

$\bar{\sigma}$	Von Mises equivalent stress
$\bar{\varepsilon}_p$	Equivalent plastic strain
δ_n	Mode I separation
δ_s	Mode II separation
$\dot{\varepsilon}_m^{pl}$	Plastic flow
$\dot{\varepsilon}^{\rho l}$	Plastic flow of fully dense matrix
σ_0	Yield stress
σ_h	Hydrostatic pressure
σ_u	Tensile strength
τ_u	Shear stress
ε_0	Yield strain

f_N	Nucleated voids volume fraction
f_F	Void volume fraction at fracture
f	Void volume fraction
f_c	Critical void fracture volume
E	Young's Modulus
G_I^c	Fracture toughness in mode I
G_{II}^c	Fracture toughness in mode II
G	Shear strength
D	Damage

Chapter 1

Introduction

1.1 Motivation

Transport industry, especially automotive and aeronautical, have always searched for new cost-effective ways of increasing the efficiency of their products while keeping or improving their reliability. Over the past years, automotive and aircraft manufacturers have been facing stricter norms and environmental regulations to limit greenhouse emissions and reduce the usage of fossil fuels. By reducing fuel consumption, not only will greenhouse emissions be reduced, but also a decrease in operational costs will be achieve, given the major role of fuel consumption on them.

One way to achieve this can be by targeting the weight of the structure, which is leading makers to continuously search for lighter material solutions without compromising the structural integrity of the all system. According to U.S. Department Of Energy [1], since 1996 there has been a significant increase in the usage of lightweight metals and composites on production cars structures, which corresponds to a weight saving of 10% on today's cars. In a McKinsey forecast [2], this increase in the use of lightweight materials shows no signs of slowing down, for both automotive and aeronautical industries, reach material usage shares of 67% and 85%, respectively, as seen in Figure 1.1.

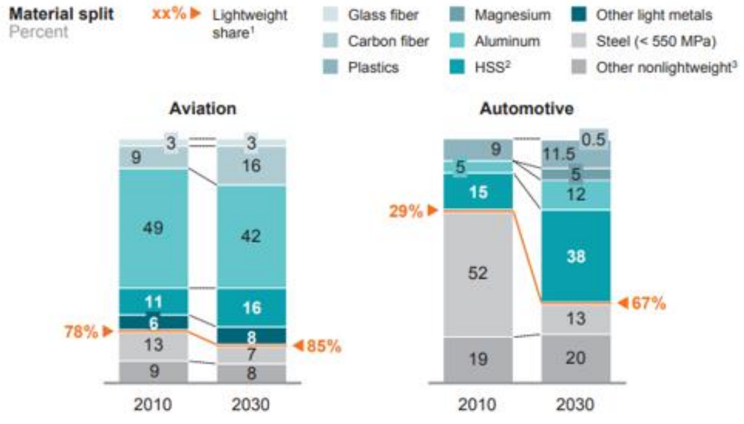

1 HSS, aluminum, magnesium, plastics (beyond current use), glass/carbon fiber
2 High-strength steel (> 550 MPa)
3 Mainly other metals, glass, fluids, interior parts for automotive, etc.

Figure 1.1: Use of lightweight materials in aeronautical and automotive industries, from [2].

Although this is a promising trend towards efficient lightweight structures, improvements of manufacturing processes can also lead to reduced production costs, while simultaneously increasing structural integrity of the vehicles. This opens a bridge to study viable alternatives for the current joining methods implemented in the transport industry. As an example, aeronautical industry still uses riveting despite some clear disadvantages related to this process such as stress concentration around the holes required for the rivet and significant added weight due to the fasteners, sealants and large overlap needed. Also, a study conducted by the Center for Automotive Research (CAR) [3] predicts a steep decrease in the usage of Resistance Spot Welding (RSW) in the automotive industry by 2030.

In this thesis, an innovative joining process capable of being a viable alternative to implement in these industries is going to be studied. The process is called Friction Stir Weld-Bonding (FSWB) aims to combine the advantages of both friction stir welding (FSW) and adhesive bonding (AB).

Given that Friction Stir Weld-bonding is still a recent method, there is gap in the literature which originates an extra motivation for this project. At impact events materials endure fast deformations and characterization of their properties is key to understand the capability of a structure to sustain damage and protect its occupants in case of crashworthiness events, like a car accident or a bird strike event. This work aims to characterize these events and be the bridge between the mechanical performance of FSWB joints at quasi-static and impact loadings.

1.2 Objectives

The main objectives of this thesis are:

- Assess lap shear strength of friction stir weld-bonded joints in quasi-static and impact loading;
- Benchmark mechanical behavior of friction stir weld-bonded joints against adhesive bonded and friction stir welding lap joints in quasi-static and impact loading;
- Model the behavior of the three joint types in both loading conditions.

1.3 Thesis outline

This thesis is divided in 6 chapters, including this one that intends to state the motivation and main objectives for the work developed in this thesis, as well as the content of the following chapters.

Chapter 2 reviews the most important topics addressed in the present work. It starts by reviewing the most common joining methods for metallic thin structures, with a special focus given to friction stir welding, adhesive bonding and Hybridization. Finally, different techniques to perform tests at higher strain rates than quasi-static are presented.

Chapter 3 details every step of the experimental works developed in this thesis, including material characterization, manufacturing of the joints and mechanical tests performed.

Chapter 4 presents the experimental results obtained. Firstly, characterization of the materials used is performed, followed by the discussion of the microstructural evolution of the joint with the help of macro and microscopic images and microhardness test results. Finally, a comparison of the mechanical performance of each joint is addressed, subjected to either quasi-static or impact events, respectively.

Chapter 5 starts by presenting the methods used to perform the numerical modelling simulations, which is followed by the parameters used to model the joints and perform the routines. Finally, a comparison between numeric and experimental results is done.

Chapter 6 provides an overall view of the results achieved in the conducted research, which is followed by suggestions on possible future works related to the technology studied.

Chapter 2

State of the Art

This chapter aims to present the joining techniques relevant for the work that will be further conducted. Special focus will be given to friction stir welding and adhesive bonding, including not only recent advances and relevant accomplishments on those subjects but also comparing them to techniques used for the same purpose. Types of Hybridization will also be discussed, focusing techniques that use adhesive bonding. Finally, a section about mid to high strain rate testing will be covered as well.

2.1 Friction stir welding

Solid state welding is a group of joining mechanisms heavily used in the automotive and aeronautic industries. This process is characterized by enabling the creation of a metallurgical bond between two separate parts. This occurs mainly due to plastic deformation and bellow the melting temperature point of the base material. There is no need to use a filler material. Pressure, heat or both are used as the energy source of the process [4]. This thesis will focus on one of these joining mechanisms: Friction stir welding.

Friction stir welding (FSW) was invented in 1991 by Wayne Thomas *et al* [5], at The Welding Institute (TWI Ltd). It represented an important breakthrough in joining technologies in a sense that it became possible to produce high integrity joints in difficult or even non-weldable designated materials, such as the aluminium of the series AA2XXX and AA7XXX, cooper and titanium. It is rapidly becoming the process of choice for manufacturing lightweight transport vehicles and other structures where high strength, good toughness, low weight, excellent fatigue life and improved fracture toughness are required [4].

Since there is no melting of material, mechanical properties of FSW are usually better when compared to fusion welding techniques.

2.1.1 Process description

FSW is a process that utilizes a tool composed by a non-consumable cylindrical shoulder with a plugged pin on the tip that penetrates the parts (from similar or dissimilar materials) to be joined.

The joining is accomplished through rotational and translational movement of the tool (Figure 2.1) which enables the pin to mix the material on the welding zone in an upward direction [6]. At the same time, the other element of the tool, the shoulder, is responsible to create and keep the heat beneath it as a result of the friction between the shoulder and the workpiece. The weld produced is asymmetrical due to the constant change in the tool rotational velocity vector when compared with the translational velocity vector. When the tool rotation and weld direction are similar on one side it is called advancing side (AS), whereas when the opposite occurs it is called retreating side (RS).

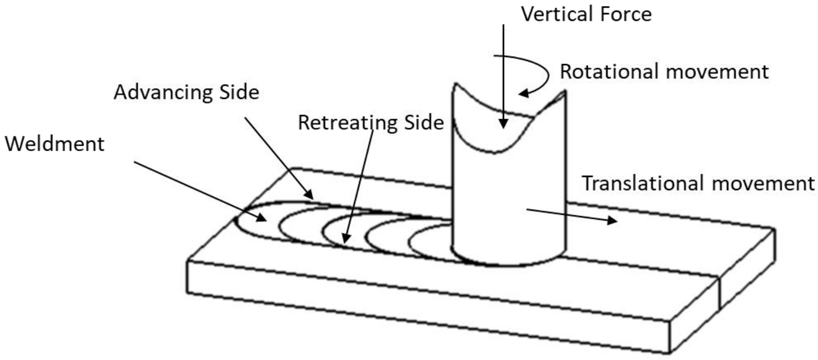

Figure 2.1: Principle of the FSW process in an overlap configuration.

This process includes four distinct phases [4]:

- Plunging phase: the rotating tool is slowly plunged into the material (due to a vertical force) until the shoulder is in contact with the upper surface of the material. This is the beginning of the plastic deformation.
- Dwelling phase: Once rotating tool reaches the point described above, the tool remains in that position, generating additional heat. This causes the material to soften making it easy for the tool to travel along the material. Plasticization of the workpiece happens at this point.
- Welding phase: After the previous phase is over, a force is applied in the direction to be welded, adding the translational movement to the tool. Heat generation along with the movement forces the plasticized material to displacement, extrusion and shearing mechanisms.
- Retracting phase: As the tool reaches the end of the weld, tool is retracted. At this point it is possible to observe a characteristic keyhole (pin hole) due to the removal of the tool from the workpiece.

The analysis of macrographs and micrographs allows to make a distinction of four zones, each one with different physical and mechanical properties. The microstructural evolution is what determines where each zone is delimited, being highly influenced by the parameters chosen. Figure 2.2 shows these zones identified on a cross sectional FSW joint.

The four zones are [4]:

- Base material (BM) where heating is not sufficient to cause changes in the microstructure and mechanical properties, keeping the original morphology.
- Heat affected zone (HAZ) where heating is sufficient to cause softening, changing the microstructure and the mechanical properties, with no plastic deformation.
- Thermo-mechanically affected zone (TMAZ) where plastic deformation and heat transfer are enough to change material properties. Material is softened and plastic flow is noticeable here

by the elongated and reoriented grains. Although a significant plastic strain occurs, it is not enough to cause recrystallization.

- Stir zone (SZ) where intense plastic deformation and heat transfer cause a recrystallization of the initial grain to a fine and equiaxed one. In this zone is possible to identify a characteristic onion ring structure that is influenced by the tool design and the flow of material around the pin.

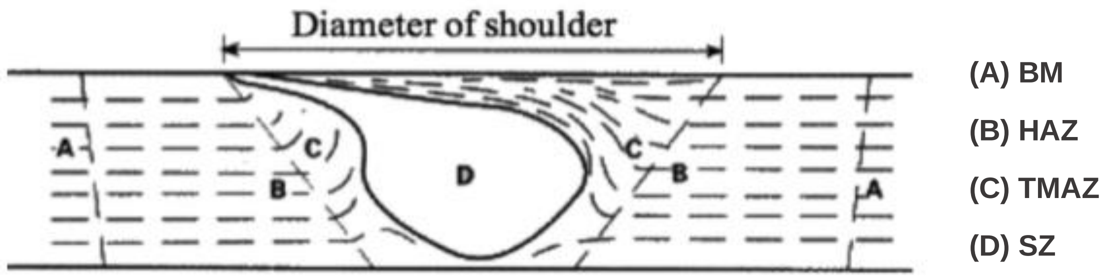

Figure 2.2: Schematic cross-section of a typical FSW weld showing the four distinct zones, adapted from [7].

It is also important to remark that some defects appear on the microstructure of the weld. The most common are the material voids, that usually occur near the edge of the SZ or beneath the top surface of the weld, and the joint line remnant, which is typically located in the SZ and it is composed by the remaining oxide particles from the original material surfaces. This latter flaw can be reduced by machining the surfaces previously to welding and controlling the welding speed [8].

For lap joints, the most recurrent defects are the hook defect in the advancing side and the top plate thinning in the retreating side, both represented in Figure 2.3. Shapes and sizes of the hook defects vary and are directly related to the material flow. These defects can be reduced or even mitigated through some techniques like double pass [4,9].

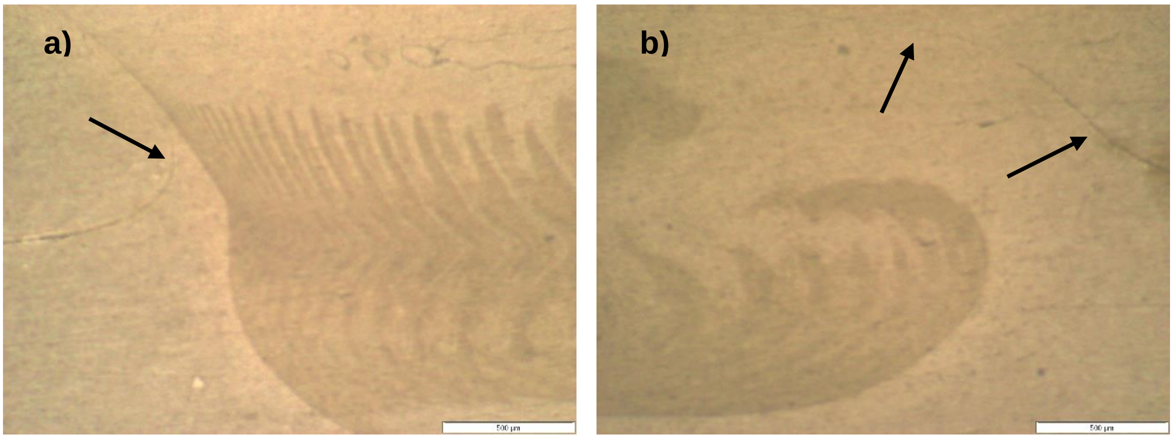

Figure 2.3: Some possible defects from FSW: a) Hook defect and b) Top plate thinning.

Point out that, although in the present work the focus is on overlap joints, FSW is a process capable of joining in a wide range of configurations, as demonstrated in the Figure 2.4.

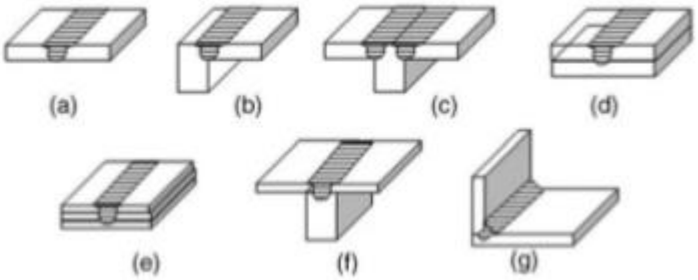

Figure 2.4: Joint configurations for friction stir welding: (a) square butt, (b) Edge butt, (c) T-butt joint, (d) Lap joint, (e) Multiple lap joint, (f) T-lap joint and (g) Fillet joint, from [4].

2.1.2 Temperature field

Material flow and heat distribution in the softened material area around the tool are considered to be the core of the FSW process, with almost every parameter leading to their control [4]. Material deformation generates heat, which is then propagated along the material, generating a temperature field.

According to Mishra *et al* [4], this temperature field is asymmetric around the pin tool, with slightly higher reported temperatures on the RS, being further proved on tensile tests where the failure occurs mainly on the RS in the HAZ region. Although in [10] the same occurs, in [11–14] the opposite happens, where the AS shows higher temperatures and the fracture occurs on the AS region, leading to the conclusion that the quality of the joint is highly affected by the welding parameters.

In FSW, heat generation is provided either by the friction generated between tool and material, based on their relative velocities, or by the plastic deformation that occurs during the stirring process. The amount of each one will be determined by the contact conditions at the tool/workpiece interface, being influenced by tool geometry, welding parameters and thermal conductivities of the workpiece. The heat is generated at the shoulder/pin and workpiece interface, with the last pair having an estimated contribution between 2% and 20% [4].

As the heat is generated at the shoulder/pin and workpiece interfaces, temperatures on the SZ are typically higher. One way to estimate these temperatures values can be done by comparing the microstructure of the weld with the aging curves of the material alloy used. Schneider *et al* [15] and Murr *et al* [16] conducted Transmission Electron Microscopy (TEM) studies on AA2195-T81 and AA6061-T6, respectively, and estimated peak temperatures around 425ºC.

A more accurate way to map the temperature field is by attaching thermocouples in the vicinity of the rotating tool. Maeda *et al* [13] experimentally reach the conclusion that peak temperatures occur near the SZ and top plate surface, with a following decrease on the direction from top to bottom plate and as distance to the centre increases. This was true even if dissimilar materials are being used, with the adding factor that temperature field will change depending on whether the material is on the AS or RS, even for the same tool rotation speed and welding speed, as seen in Figure 2.5.

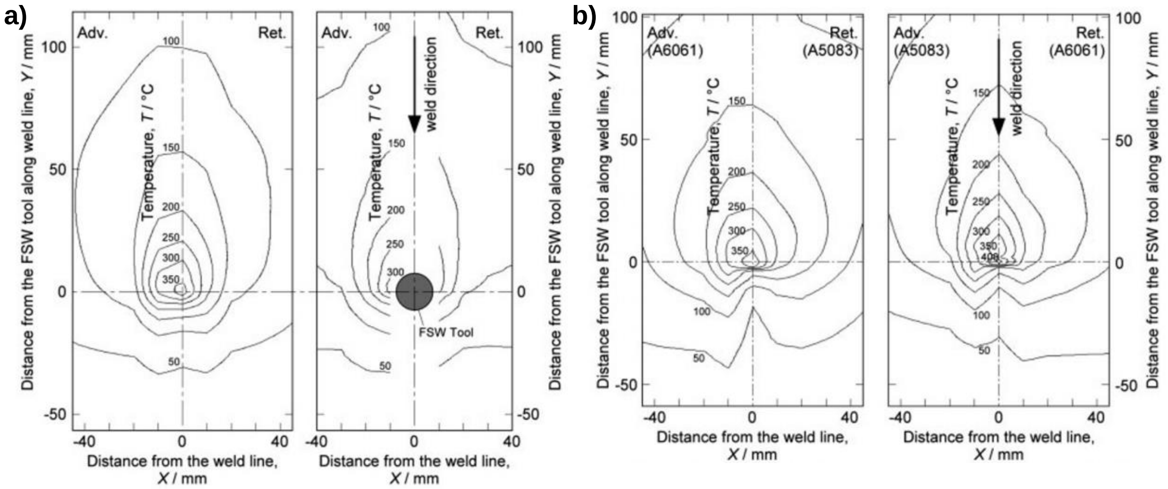

Figure 2.5: Temperature field on the vicinity of the FSW tool for a) AA7075 on bottom and top surfaces, respectively, and b) bottom surface for the dissimilar material AA6061 and AA5083, adapted from [13].

Wu *et al* [14] studied the temperature field in the welding zone and workpiece on 2A14-T6 aluminium alloy plates. It was shown that during the welding phase temperature at the shoulder is always higher than the temperature at the pin, which agrees with the literature.

2.1.3 Material flow

Material flow has a great influence on the microstructure formation, hence its importance when trying to optimize parameters and characterize weld properties. Although thorough research is being made to understand such an important key factor, it is still quite difficult to predict the microstructure development due to the vast number of pin geometries and materials available in this process.

There are two extreme boundary conditions between the tool and the rotating material. The first one is sliding condition in which the material does not rotate around the tool, being only extruded, and the second one is sticking condition, where material velocity around the pin is equal to the tool's velocity. Although a mixture of both conditions is what usually happens in the process, conditions can go up to extrusion dominant or mixing dominant depending on welding parameters, tool geometry, workpiece material, among others.

As mentioned before, temperature field and material flow are interconnected, which means that material flow around the pin is also asymmetric, which leads to the appearance of different characteristic zones mentioned in a previous section. The AS presents a higher material flow when compared to the RS, indicating a higher effective strain on the first one [14].

Colligan [17] and Huang *et al* [18] in their experimental works describe the flow path in the following way: on the advancing side stirred material is subjected to a high deformation, being pushed to the bottom of the stir zone (SZ) while on the retreating side flow has an upward direction, with the material being extruded and deposited behind the tool pin.

Notice that, as it is impossible to observe the material flow directly, material markers such as steel shots [17] or copper foil [19] can be used. These techniques are time consuming and costly and so numerical analysis [14] is a more effective and advantageous way to study FSW process.

2.1.4 Hardness

When performing hardness tests, it is possible to see clearly the influence that the FSW process has on the mechanical properties of a joint. A typical cross-section profile for a heat-treated aluminium is shown in Figure 2.6. It is possible to observe an abrupt decrease in hardness in the HAZ areas, meaning that the thermal cycle highly influences hardness, as well as the W shape curve characteristic of precipitation hardened aluminium alloys [20]. Note also that if the aluminium has not undergone through any heat treatment, the loss of mechanical properties is less accentuated.

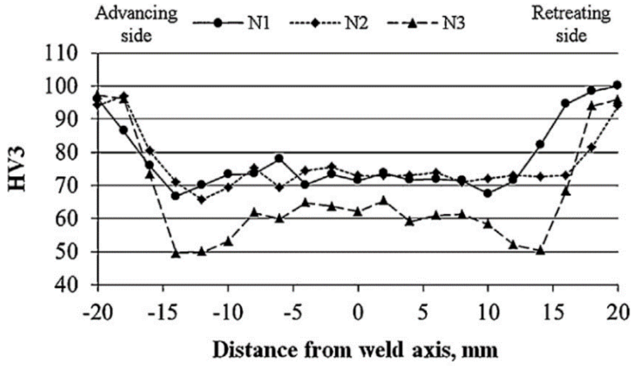

Figure 2.6: Hardness profile of FSW specimens using 3 different tools, from [20].

2.1.5 Residual stress

Residual stresses are stresses caused by thermal or mechanical application that stay in the component after all the external forces have been removed. In the case of welded joints, these stresses will reduce the ability to sustain an applied external force while maintaining structural integrity [7]. As in other processes, in FSW this happens due to the expansion and contraction during heating and cooling, respectively. However, in comparison to fusion welding, residual stresses in FSW are much lower mostly due to peak temperatures being around 80% of the melting point temperature, contrary to fusion were melting is required.

In Richter-Trummer *et al* [21], it is shown that clamping forces influence not only the residual stresses but also the distortion on the plates. It was reached the conclusion that, with no initial gap between the plates, a moderate but higher clamping force will lead to an overall lower distortion when compared to lower clamping forces, Figure 2.7.

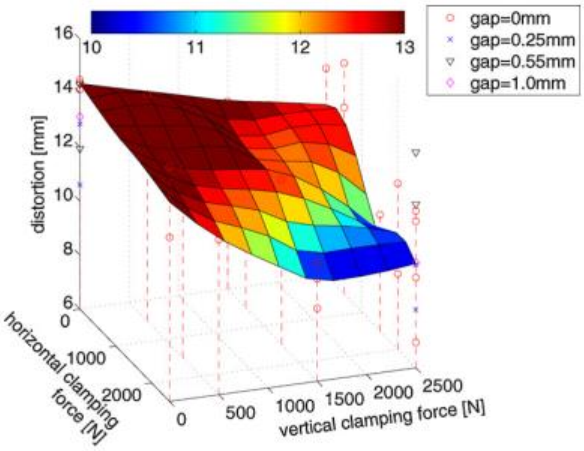

Figure 2.7: Overall distortion for surfaces with no initial gap obtain by changing clamping forces, from [22].

The same can be said to residual stresses, as Figure 2.8 points out. With the increase of the clamping force it is possible to have a better uniform stress distribution across the thickness of the specimen, with the tensile residual stresses concentrated in the weld bead. It should also be pointed out that tensile stresses can lead to catastrophic failure due to being a source of crack initiation [7], being one of the reasons why failure usually occurs on the HAZ and TMAZ.

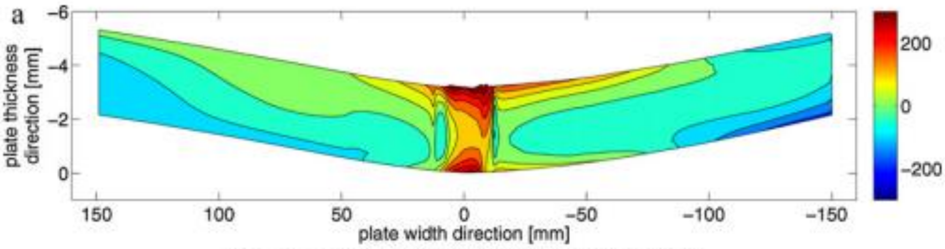

FSW102 - horizontal and vertical clamping forces: 0N; 0N

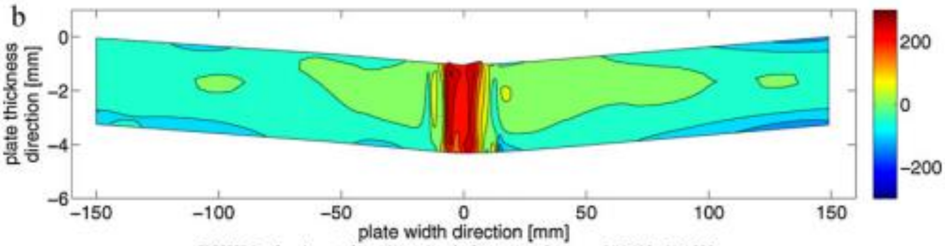

FSW86 - horizontal and vertical clamping forces: 2500N; 2500N

Figure 2.8: Residual stress distribution [MPa] in welding direction at a cross section through the centre of the plate. Two different clamping forces are considered, from [22].

2.1.6 FSW process parameters

Many variables, either direct or indirect, need to be considered when trying to define the optimal parameters of the welded joints to be developed. This is a crucial part of the project owing to the influence of parameters, such as tool geometry and welding speed, have on the quality of the produced welded joints.

The parameters that influence post weld properties are vast, being the main ones [4,22]:

- Rotational speed (rpm)

- Welding (traverse) speed (mm/s)
- Axial force (KN)
- Tool geometry
- D/d ratio of tool
- Pin length (mm)
- Tool shoulder diameter D (mm)
- Pin diameter d (mm)
- Tool tilted angle (°)
- Weld pitch ratio (rev/mm)

In this thesis, the parameters that will be used have already been well defined since there are literature that thoroughly discusses these aspects [9]. If optimization needed to be addressed such could be achieved using statistical methods like Taguchi and/or ANOVA.

Of all these parameters mentioned above, there are some that have been study more thoroughly, such as the rotational speed, welding speed, axial force and tool geometry, as they have a great impact on variables such as heat generation and material flow [7].

As an example of that, Lakshminarayanan and Balasubramanian [23], reached the conclusion that the contribution to the tensile strength of FSW RDE-40 aluminium of the rotational speed, welding speed and axial force is 41%, 33% and 21%, respectively. Note also that, according to Sreenivas *et al* [24], axial force does not influence heat input since precipitation and distribution of the strengthening precipitates stays unaffected.

Prasad *et al* [25], studied the influence of the rotational speed, welding speed and tool tilt angle to measure the influence of each on some mechanical properties, such as hardness, and reached the conclusion that major contributor to it at the welding zone was the welding speed, 67.52%, while the least one was rotational speed, with 4.39%. Although the contribution of rotational speed seems small, Wu *et al* [14] reach the conclusion that for high rotation speeds, material beneath the shoulder is prone to be extruded to the pin stirred zone (PSZ) after flowing back to the AS, causing turbulence on the flow path and possible appearance of defect in the welds.

The weld pitch ratio is an empirical value that allows to predict some effects and failures in the weld region. The value obtained in equation 2.1 will determine if the weld condition is cold, intermediate or hot. A typical value for aluminium alloys on the intermediate range is 4, which means that a higher value will define the weld condition as hot and lower one as cold. The difference between the two can be identified on the size of the HAZ and TMAZ zones, which for the hot condition, with high rotation speeds and low welding speeds, will result in a higher HAZ and a smaller TMAZ, and for the cold condition the opposite. In Nandan *et al* [7], one of the reasons for wormhole defect formation is connected to lower weld pitch ratios. Also, size of these wormholes increases with welding speed for the same rotational speed, suggesting a poor material flow near the bottom of the weld in which wormholes occur.

$$Weld\,pitch\,ratio\,(rev/mm) \;=\; \frac{\omega\,(rev/min)}{\upsilon\,(mm/min)} \tag{2.1}$$

Studies on tool geometry were also thoroughly conducted since this influences many variables, such as heat generation and material plastic flow. Verma *et al* [26], concluded that the geometry of the pin has a significantly effect on the thermal cycle of the FSW process. Also, the pin profile with the best tensile overall performance was the square one, due to its lower heat input and proper mixing of the SZ, which means a smaller grain size in this zone and leads the joint fracture to the HAZ. Same conclusion was drawn by Elangovan and Balasubramanian in [27], using a similar set of FSW tools, Figure 2.9.

However, when joints are made of thicker plates (above 12 mm on butt welds), conventional pin profiles are replaced for more complex shapes, such as the Whorl and the MX Triflute developed by TWI, due to their higher swept rate, given by the ratio between the swept volume during rotation and the volume of the pin, which allows for a reduction in the appearance of voids and more effective oxide surface disruption [28].

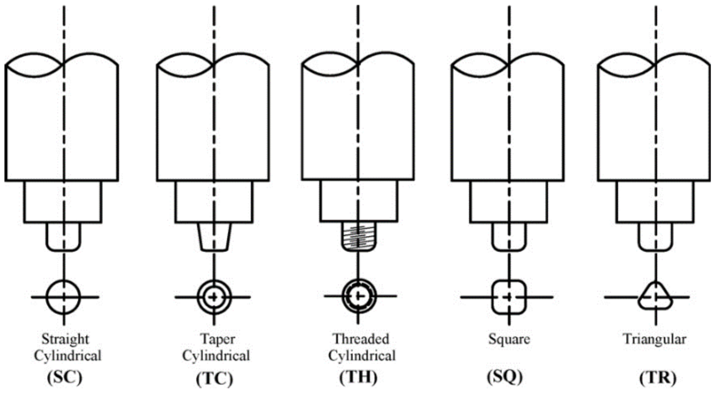

Figure 2.9: Conventional FSW tool pin profiles, from [27].

2.1.7 Benefits of FSW

This new process brings some advantages over fusion welding due to the absence of base material melting. Some key benefits of friction stir welding with respect to metallurgy, environment and energy are listed as follows [4,29,30]:

- **Metallurgical benefits**
  - Solid phase process
  - Low distortion and shrinkage of work piece
  - Good dimensional stability and repeatability
  - No loss of alloying elements
  - Excellent metallurgical properties in the joint area
  - Fine microstructure
  - Elimination of problems of hot cracking and porosity
  - Replace multiple parts joined by fasteners
  - Capability to weld aluminium alloys of the series AA2XXX and AA7XXX
  - Capability to join dissimilar alloys

- **Environmental benefits**
    - No shielding gas required
    - No surface cleaning required
    - Eliminate grinding wastes
    - Consumable materials saving (e.g. filler materials, gases)
    - No harmful emissions
- **Economic benefits**
    - Improved materials use (e.g., joining different thickness) allows reduction in weight
    - Low energy input (e.g. only 2.5% of the energy needed for a laser weld)
    - Decreased fuel consumption in light weight aircraft, automotive and ship applications

Despite all these advantages, there are still some drawbacks, namely [30]:

- Joints are not self-supporting, which will add up significant cost for designing and producing clamping systems that can restrain properly the joints;
- Existence of hole at the end of the weld can be seen as a disadvantage, although some solutions can be used, such as an auto-adjusting tool or a technique called Active-Passive Filling Friction Stir Repairing (A-PFFSR) [31];
- Lack of flexibility to weld fillets and complex shapes when compared to other conventional joining processes.

As FSW is a recent technology, there is still room to optimize the main welding parameters, overcoming the previous mentioned limitation giving more flexibility to the process, when compared to conventional joining processes.

2.1.8 Applications

The intense investigation around FSW and results obtained from it has produced a fast spread of these technologies to various industries, with a special focus on the transportation industry, such as aerospace, railway and automotive industries (Figure 2.10).

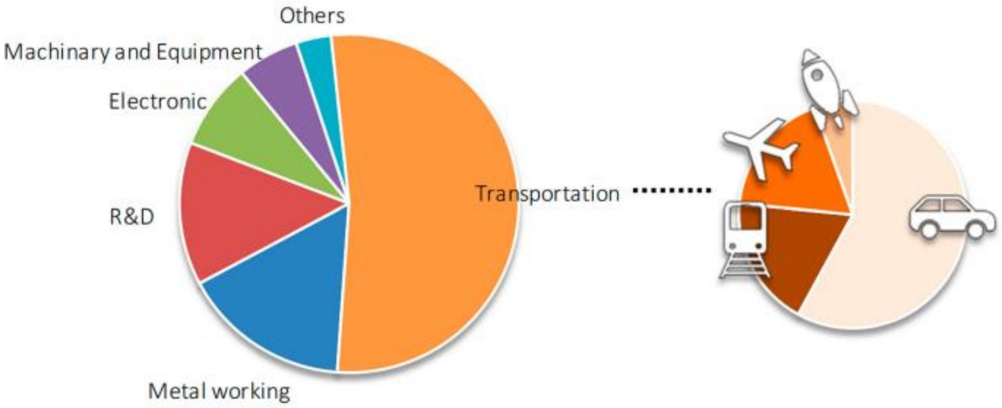

Figure 2.10: Application of FSW technology in different areas of the industry, from [32].

In the aerospace industry, usage of aluminium alloys from the AA2XXX and AA7XXX series was demanding a new manufacturing process other than conventional fusion welding, due to the difficulty in joining these materials, which resulted in poor quality joints from hot cracking [33]. FSW technology first investigation in the aerospace sector began in 1996 with the search for a manufacturing process capable of weld the AL-Li 2195 alloy used to produce the space shuttle external tank. This investigation culminated, in 2005, with the launch of the external tank 134 [33].

In 1999 Boeing became the first company to introduce FSW technology into space, with the application of FSW to the interstage modules of Delta II rockets and, later, for the common booster core tanks of the Delta IV which, in this case, resulted in a weld strength increase up to 50% and decrease in cycle time and manufacturing cost of 80% and 60%, respectively [33].

Space Exploration Technologies Corporation (Space X) implemented this technology to produce the tanks in their partially reusable vehicles Falcon 1 and Falcon 9, with the latter one claiming to be the largest fully FSW functional structure in the world (both dooms and walls are made with FSW) [33], Figure 2.11.

Figure 2.11: Falcon’s 9 tank manufacture with circumferential and longitudinal friction stir welds, from [33].

In aviation industry, FSW started to appear first in military applications and only later in commercial applications since the latter ones needed Federal Aviation Administration (FAA) certification. Boeing introduced FSW technology to produce the toe nails of the C-17 cargo ramp, reporting later, in 2006, a zero scrap rate after all the first manufactured components had successfully passed non-destructive inspection [33]. Airbus first applied FSW in the floor panels of their A400M military aircraft.

In 2002, Eclipse Aviation received approval from the FAA to introduce FSW in the manufacturing of their Eclipse 500 business jet. Implementation of friction stir welding in the body skin and airframe allowed not only a replacement of around 7000 rivets but also a reduction in assemble time and cost. Airbus and Embraer followed this trend, manufacturing fuselage panels with FSW on their A380 aircrafts and Legacy 450 and 500 Jets, respectively [34].

Automotive industry has also been using FSW and its variants, such as friction stir spot welding (FSSW), in the most various automobile components, such as suspension systems, engine blocks, drive shafts and wheel rims.

Aluminium suspension links used in 2003 Lincoln Town Car L were produced by using FSW to join two identical extrusions, which allowed to maintain geometric tolerance lost when bigger extrusions are made. In 2006, Riftec started to supply a tailored welded blank used in the Audi R8 centre closing panel, achieving a reduction of 20% in this component on the material used and reduction in the manufacturing process [33]. Mercedes-Benz also uses friction stir welding to join blanks with different thicknesses to form the centre tunnel of the Mercedes SL R231 model, allowing a reduction of unnecessary weight while maintaining high levels of stiffness [35], Figure 2.12.

Figure 2.12: Centre tunnel of the Mercedes-Benz SL R231, from [35].

Honda Motor Company applied FSW to the subframe of the 2013 Honda Accord, Figure 2.13. This allowed not only to reduce the weight of the frame by 25%, since it was possible to combine a higher amount of aluminium with steel, but also to increase stiffness of the mounting points by 20%, previously joined by bolts [36].

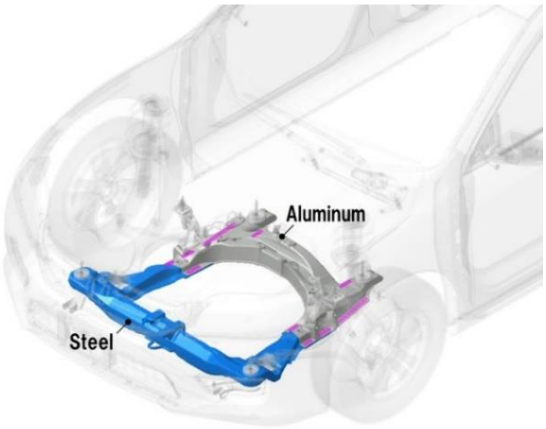

Figure 2.13: Front subframe of the Honda Accord 2013 model, from [36].

As previously state, transportation industry is not the only one using FSW. As an example, Apple used FSW to join the front and back case components of the iMac 2012 [37], which allowed not only to decrease the thickness of the monitor to 5 mm but also keeping a seamless strong joint.

2.2 Adhesive bounding

Adhesive bounding is another joint technology that has been rising in the aerospace and aeronautical industries since the 1970's due to the increase usage of composites in those industries. Its use is also progressively being adopted in the automotive and railway industry. Despite showing potential to be implemented in safety critical applications, it has not happened yet since more evidence of its performance is needed when it comes to long term strength [38,39].

Many advantages can show the attractiveness of this technology when compared to conventional mechanical fasteners [40], namely the capability of providing a better load distribution (Figure 2.14), increase fatigue life, weight savings, reduction of machining costs and good energy absorption.

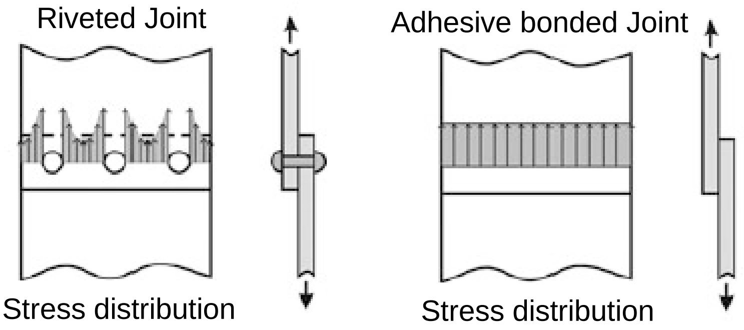

Figure 2.14: Stress distribution in rivet and adhesive bonded joints, adapted from [40].

In the automotive industry, adhesives play a huge role when dissimilar materials are found in the frame of the car, such as in the BMW 7 series [41], since they can act as an insulator and prevent galvanic corrosion. At the same time, it also allows to enhance body stiffness and its crashworthiness.

As in any other process, adhesive bonding as its own disadvantages too. To ensure maximum performance, adherent surfaces require a special treatment, depending on the material, as it can be seen in the next subsection. The objective of this treatment is to get the joint to fail in a cohesive way, representing this the perfect adhesion situation. Figure 2.15 shows the possible failures on adhesive bonded joints. Note also that joint behaviour is extremely sensitive to load direction, being peel and cleavage stresses preferably avoided due to the fragility of this type of joints to these stresses.

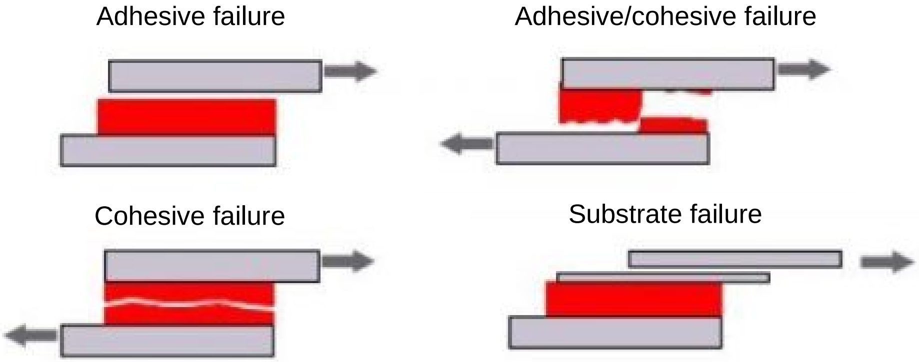

Figure 2.15: Failure types in bonded joints, adapted from [42].

The performance of these joints is highly affected due to exposure to hostile environments. In [40], it is referenced an experiment where joints were exposed to humidity environmental during a period of time. It was found out that, with a contamination level of 0.62 mg/cm^2, a 45% decrease in strength was observed. This moisture absorption from the adhesive occurs due to water migration to the interface between the adhesive and the adherent or to water diffusion.

Another critical aspect to have into account is the temperatures at which the adhesive is subjected, whether it is during curing or operation, since it may induce residual stresses and affect the mechanical performance of the joint. This situation is even more important when dissimilar materials are used due to their different coefficient of thermal expansion (CTE) [40].

Curing is a pivotal point for adhesives. An incorrect curing is enough to compromise the integrity of the joint since these materials are polymeric and need an adequate cure to transfer the loads between substrates [40]. The type of cure and subsequent mechanical properties depends extremely on the adhesive characteristics [43] and, although there is a large number of adhesives that can cure at room temperature, studies conduct by Braga in [9] suggest that room temperature is not enough to fully cure the adhesive, with a reduction of around 20% on tensile strength, although it keeps an higher ductility due to the higher number of cross-linking polymeric chains present at higher temperatures.

Inspecting quality of the joints once manufactured and during service life through non-destructive tests (NDT) is also a difficult topic. Most of the tests available require the use of ultrasounds, being time consuming for large swept areas and only detecting debonding and poor cohesive properties, leaving monitorization of interfacial properties difficult to achieve [40].

2.2.1 Impact behaviour

Although much research was carried out to characterize adhesive joints subjected to quasi-static loading, research on high loading rates is still quite limited. Performing experiments on that matter is of extreme importance so that performance of the adhesives can be fully understood. Adhesives as polymeric materials have a viscoelastic behaviour, hence the importance to characterize them in a wide strain range.

Although it is important to know adhesive intrinsic properties by performing bulk tests, this can only be seen as an estimative to how the adhesive joint could perform since adhesive joints do not depend exclusively from the adhesive but also from the adherent. Also, it is worth mentioning that joint loading is more complex than the uniaxial case. Additional tests need to me done to take into account the interfacial properties between adherent and adhesive.

Harris and Adams [44] performed a series of tests on single lap joints (SLJ) using a modified Izod pendulum impact machine. Four types of adhesive and three types of aluminium alloy adherent were used, and it was found that high rates of loading do not affect joint strength significantly, Figure 2.16 a). They also reach the conclusion that the energy absorption came mainly from the deformation of the adherent, leading to the find that adherent materials with a lower yield strength (ductile) are keener to absorb the energy from the impact.

Yokoyama and Nakai [45] used a modified split Hopkinson pressure bar to perform tensile test on butt joints. Joint tensile strength in this case increased significantly with the growth of the loading rate, Figure 2.16 b). It was also pointed out that the rate dependency of the joint is entirely caused by the inherent rate dependency of the epoxy in use, showing a much higher fracture force (brittle behaviour) on impact than on static but with an inverse trend on the extension, with a much smaller one on impact. Variations in the adhesive thickness of approximately up to 180 μm were tried and it was verified a decrease in the joint strenght with the increasing of the adhesive thickness, explained by the stress concentration at the inner free edges.

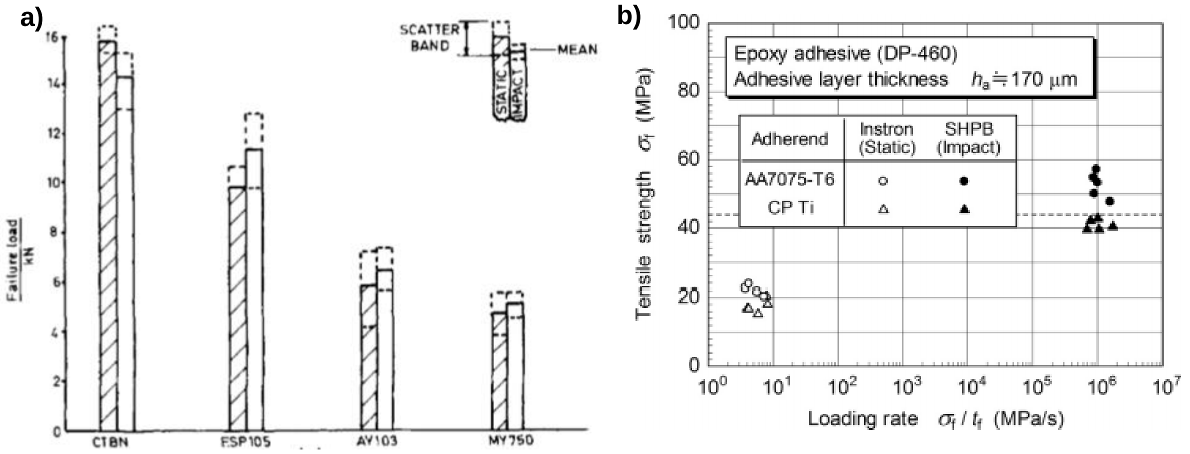

Figure 2.16: Static vs impact comparison: a) from Harris and Adams [44] and b) from Yokoyama and Nakai [45].

Goglio and Rossetto [46] used an instrumented Charpy pendulum to perform tensile loads on SLJ and reach the conclusion that joint strength in dynamic conditions is higher when compared with static conditions, showing the highest values for a thickness of 0.5 mm of the adhesive layer when compared to a layer of 1 mm. Goda and Sawa [47] with a split Hopkinson pressure bar apparatus reach the conclusion that a thickness of 0.2 mm of adhesive would provide the highest joint strength under dynamic conditions.

Yildiz *et al* [48] performed a characterization of the adhesive properties under mode I loading on a large scale shock tube for strain rates up to around 14000 s^{-1}. In these tests, as strain rates increases, adhesive behaves like a brittle material, as expected from previous experiments, leading to an abrupt drop on the capacity to absorb energy. That behaviour can be seen by comparing a quasi-static test with a dynamic one with a strain rate of 13567 s^{-1} on an aluminium-epoxy adhesive joint, with the latter having a yield strength nine times higher while reducing the strain failure to half.

Adhesive joint’s performance, both in quasi-static and impact loadings, can be enhanced by adhesive mixing. Silva *et al* [49] did a series of experiments and compared adhesive bonded joints with single and mixed adhesive, reaching the conclusion that a mix of ductile adhesive at the end of the joints with a brittle adhesive increases joint performance overall by retaining or even slightly improving static strength of the brittle adhesive and the impact strength of the ductile one.

2.2.2 Surface treatment

As said previously, one of the drawbacks of using adhesive is the need to use surface treatments to make the surface receptive to it. This treatment will help minimize possible sources of external damage, such as corrosion, ageing or continuous stress, and promote a better adhesion between the adhesive and the adherent by providing a good interfacial strength [40]. Although the type of surface treatment is dependent on the mechanical requirements of the joint, the previous goals are achieved by [40]:

- Preventing the formation of any weak boundary layer on the adherend surface (machine oils, weak oxides or hydroxides);
- Maximizing the degree of the intimate molecular contact between the adhesive and the adherent during the bonding and the curing processes by creating a high-surface free energy;
- Passivating the surface in order to offer protection against organic and inorganic contamination after bonding.

Contamination can be divided in two groups: organic and inorganic. Choosing and applying the right surface treatment is essential to prevent contamination of the joint, either by using only a degrease, in case of organic contamination, or by adding also a deoxidizing solution, in case of inorganic contamination. Jeenjitkaew *et al* [50], reaches the conclusion that any sort of contaminant present in the joint is enough to cause a reduction in strength of up to 27%.

The three main types of surface preparation are: degreasing, mechanical abrasion and chemical treatments.

Degreasing is the simplest form to achieve a clean surface. This is a wide category and it can go from a simple whipping to ultrasonic cleaning. Although it can sometimes be seen as a good stand-alone option, mechanical and chemical treatments are a better option to improve levels of adhesion and durability [40].

Mechanical abrasion allows the removal of the weak layer by roughening the surface of the adherent. This will allow mechanical interlocking, facilitating the energy dissipation and distributing the stress away of the interphase region, increasing its performance [40]. This treatment can range from a manual abrading, using pads or abrasive papers, to grit-blasting.

Chemical treatment can be etchant or chemical conversion coating. Etchant type use strong acids to remove the weak organic and inorganic layer, enhancing adherents' surface by providing a higher surface energy, while chemical conversion coating creates a film on the adherents' surface, creating the desired roughness on it. Usually for aluminium, the best treatment is the electrochemical one, which is a complex and time consuming anodization process [40]. The most used ones are the ones that use direct current (DC) and alternate current (AC) electrodes, like Chromic Acid Anodization (CAA), Phosphoric Acid Anodization (PAA) and Sulfuric Acid Anodization (SAA). Currently, PAA and CAA are progressively being discontinued due to health safety related issues [51].

In [9] Braga conducted a study to understand the influence that surface treatment had on the mechanical properties of the joints. Adhesive bonded joints and Hybrid bonded joints (FSW+AB) were manufactured with sandblasting and with PAA as surface treatments and the latter treatment showed a significant increase in ductility for both type of joints, as stated in Figure 2.17.

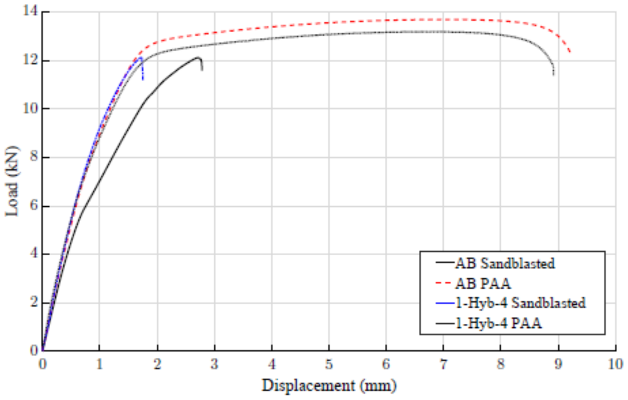

Figure 2.17: Influence of surface treatment on adhesive and Hybrid joints, from [9].

2.3 Hybrid Welding and bonding

Hybridization processes are the way to incorporate the advantages of adhesive bonding by associating them, at the same time, with other joint techniques capable of suppressing the downsides brought by the first one. The most common methods are a combination of adhesive with bolts, riveting, clinching and welding, with the latter one showing generally better results despite demanding a more intense manufacturing procedure [52].

2.3.1 Bolt-bonded joints

One of the most widely spread and simple techniques used is the bolt-adhesive joints, a combination of mechanical fastening and adhesive bonding. This method has a good performance when loaded from different directions since the adhesive carries the shear stresses and the bolt carry the transverse ones. Also, using a fastened joint allows prediction of long-term performance, one of the previously state reasons on why the adhesive type of joint is not trusted for structural design. For example, in case of an environmental attack, such as fire hazard, while the adhesive softens due to the elevate temperatures, bolts will act as a fail-safe mode, helping to carry the loads through the joint and allowing to maintain joint's stiffness and, possibly, preventing the immediate failure of it [39].

Kelly [53] investigated quasi-static strength of hybrid (bolted and bonded) composite SLJ (Figure 2.18) and reach the conclusion that, when using a ductile adhesive, Hybrid joints shown an increase of 11% in ultimate tensile stress (UTS) when compared to the bonded joints. It was also noticed that for lower loads, adhesive was the main load bearing mechanism and, once 50% of the UTS was reached, an increase in stiffness was noticed, suggesting that the bolt started to also bear loading along with the adhesive, preventing the relative displacement of the adherents.

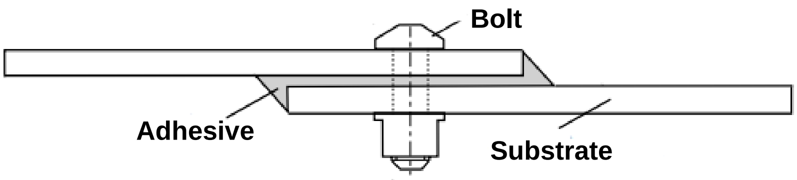

Figure 2.18: Representative Bolt-adhesive system, adapted from [53].

Kweon *et al* [54] evaluated the tensile strength of a carbon composite and aluminium joint joined through bolt and adhesive and stated that the utilization of an hybrid joint technique would only achieve the desired increase in performance, when compared the solo joint methods, if the bolt is stronger than the bonding.

Lotus used threaded fasteners with adhesive bonding in its Lotus Elise (Series 1), allowing the use of thinner aluminium sections instead of steel, which end up saving 50% of the spaceframe's weight while maintaining a high torsional stiffness [55].

2.3.2 Rivet-bonded joints

Hybrid riveted technology is usually done by adding adhesive to the faying surfaces and then use one of the two basic riveted following techniques:

- Pop Riveting (PR), where a hole is previously made in the parts to be joined. In this case, plastic deformation only occurs on the rivet, allowing the use of almost any materials for the joint.
- Self-Piercing Riveting (SPR), where plastic deformation occurs in both the rivet and the parts. Although brittle materials cannot be used, SPR are usually chosen when mechanical performance is a must.

Rivet-bonded joint's objective is to combine the strength achieved in adhesive bonding with the reduced manufacturing time of the rivet joining. It was reported in [52] that rivet-bonded joints indeed have a similar strength when compared to adhesive bonded joints, since rivet stops peeling of the adhesive and adhesive contributes with an increase shear performance, while reducing manufacturing time up to 40% when compared to arc welding processes.

Sadowski *et al* [56] studied this hybrid process and compared it with riveting and bonding only, on double lap joints (DLJ) of aluminium (Figure 2.19). The Hybrid joints performance was significantly better than the riveted only, with an increase of 130% in tensile strength. Comparatively to adhesive bonded only, Hybrid joints achieved a tensile strength 11% higher. It is also important to notice that energy absorption of the Hybrid joints was equal to the sum of the two simple joints.

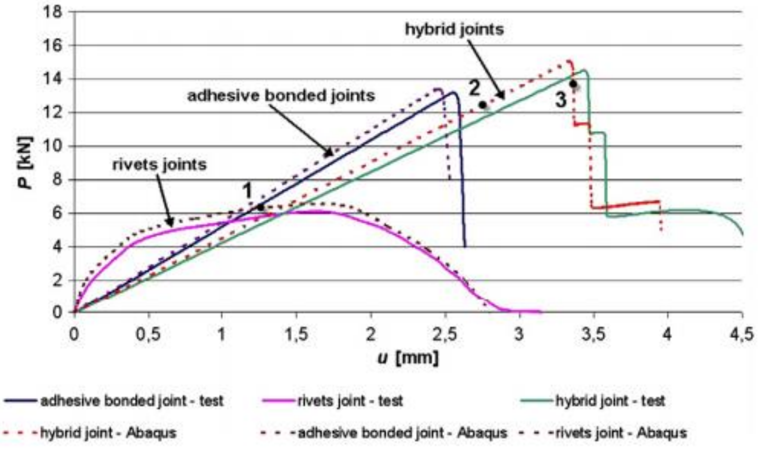

Figure 2.19: Comparation of rivet, adhesive and Hybrid joints, experimentally and numerically [56].

Body structure of the Jaguar's XJ (X350) model was the first industrial appearance of the rivet-bonded joints technology, allowing an extensive use of aluminium and not only a reduction of 200 kg comparatively to the predecessor but also an increase in stiffness of 60% [57].

2.3.3 Clinch-bonded joints

Clinching is a joint technique that started to be industrialized in the automotive industry in 1985 by Audi. This is a method used to join two metal parts with the help of a punch and a die, which deforms the metal sheets and locks the parts through force locking, material locking and "S" shape locking [52], Figure 2.20. Adding the adhesive layer on one of the faying faces will try to surpass the downsides of each single technique, namely the corrosion resistance and shear strength of the clinching technique and the peeling resistance and clamping systems of the bonded method.

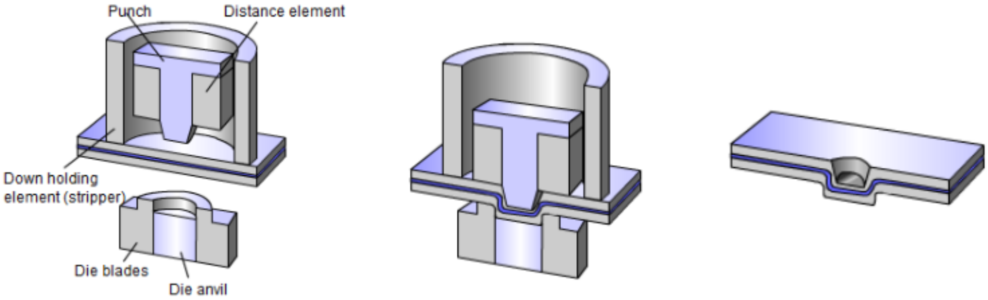

Figure 2.20: Clinch-bonded joints manufacturing process schematic, from [55].

Sadowski *et al* [58] studied the influence that the adhesive has when added to clinched joints and stated that the adhesive use increased strength of the joint up to 40%, with best results happening when clinching was done previously the adhesive cure. Ductility of the joint greatly increased also, with its performance being highly dependable of the type and surface are of adhesive.

Although the advantages brought by this technique, clinch-bonding is not quite as strong as spot welded or rivet joining, meaning that, in automotive industry, this technology will be used for parts were high structural performance is not critical.

2.3.4 Weld-bonding joints

First appearance of weld-bonding is reported to have been in 1959 when USSR's airplane Antonov AN-24 took its first flight [59]. At the time, this technology replaced conventional riveting, improving not only structural strength but also its durability. It consisted in using resistance spot welding first, followed by an application of a low viscosity adhesive on the overlap. This method is called "flow-in" method since the adhesive flows to the overlap interface. However, as this method is not suitable for mass production, a different variation was introduced. This new method of name "weld-through", the most used of this type, consisted in applying first the adhesive and only later spot welding it. This method also gives less thermal stresses when compared to flow in technique [60].A schematic of both methods is present in Figure 2.21.

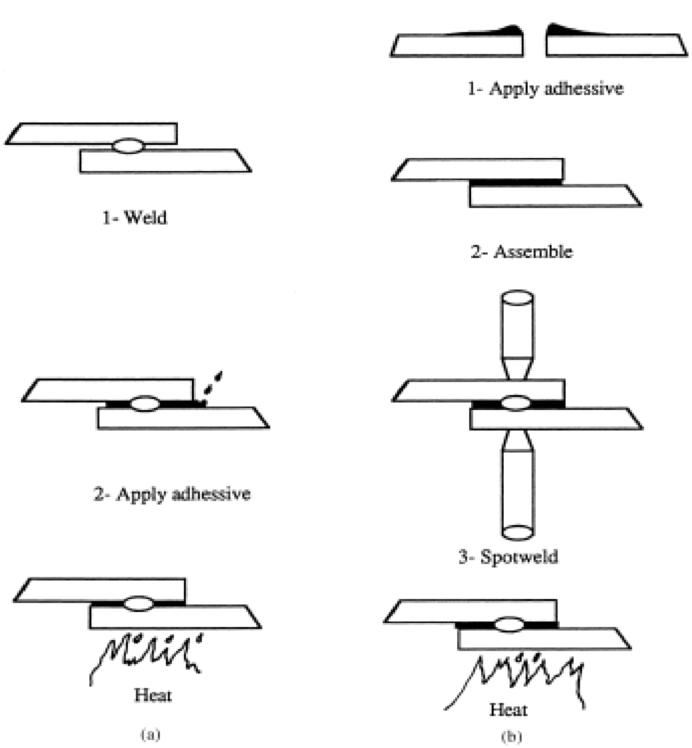

Figure 2.21: Weld-bonding techniques: (a) Flow-in and (b) Weld-through, from [60].

The use of this technology in the automotive industry is also widely spread since it has a relative low cost and it is a highly automated process. By combining welding and adhesive bonding, structural designers achieved the following benefits when compared to conventional fastening techniques [61]:

- Increased static strength due to a bigger joining area
- Increased fatigue life by reducing stress concentrations
- Increased stiffness by preventing slip at fasteners
- Improved resistance to corrosion
- Weight savings
- Vibration Damping and noise reduction

In Weitzenböck and D. McGeorge [39], a comparison between spot welding and weld bonding was done and it was report a better crash performance for the latter one. Also, Hayat in [62] compared AB, RSW and adhesive weld-bonding (AWB) joints made of DP 600 Steel and it was found out that, once again, the AWB specimen showed a higher strenght. Gaul and Weber [63] studied weldbonded (spot welding + adhesive) steel SLJ and stated that not only the tensile strength is higher but also the absorbed energy in both quasi-static and impact tests comparatively to spot welding only is higher. The latter parameter is directed correlated with the viscosity of the adhesive used.

Moroni *et al* [64] conducted an experimental campaign involving diferent manufacturing technologies in order to assess their strength, stiffness and energy absorption. In their study, intended to compare resistance spot welding, clinching, riveting, self-piercing riveting and adhesive bonding only joints and their respectuve hybridization (with adhesive), the following conclusion were taken:

- For Hybrid Resistance Spot Welding (HRSW), there is an increase in both strength and stiffness comparatively to the single technologies, while in respect to the energy absorption the increase is of almost 32 J (550%). A reduction in the dependence of temperature and ageing with respect to adhesive bonded joints also occurs.
- For the different hybrid fastened joints (clinching, riveting and self-piercing riveting), there is an increase in stiffness and energy absorption, more noticeble in the last one, comparatively to each of the single techniques used alone. In terms of maximum load, while hybrid techniques show a significant improvent comparatively to the fastened joints, adhesive bonded only joints still have a higher maximum load, meaning that the contribution of the adhesive is more evident due to the weaker fastener joining methods. Due to the last mentioned fact, temperature and ageing dependency of the Hybrid joints are similar to the adhesive bonded only.
- “Tayloring” the joint based on Design of Experiments (DoE) results is possible and very useful to obtain not just a better mechanical performance but also a manufacturing decreased cost, depending on the joint’s purpose.

Other welding techniques, such as Plasma Arc Welding (PAW) [65], Laser Beam Welding (LBW) [66], Metal Inert Gas (MIG) spot welding [67], Magnetic Pulse Welding (MPW) [68] and ultrasonic welding [69], have been study and all of them showed a higher joint stability and a maximum failure shear strength when combined with adhesive, comparatively with the conventional technology alone.

Despite the benefits previously stated in this subsection, fusion welding relies on high heat inputs, which increases the damage around the welded area and on the adhesive. Also, the increase application of lightweight materials, such as aluminium and magnesium alloys, promotes the emergence of new technologies, such as FSW and its variates like FSSW, in which the difference to the former mentioned is the absence of transverse movement.

Chowdhury *et al* [70] conducted a study to understand the influence of adding adhesive to FSSW on aluminium-magnesium joints. Results from tensile and fatigue tests are shown in Figure 2.22.

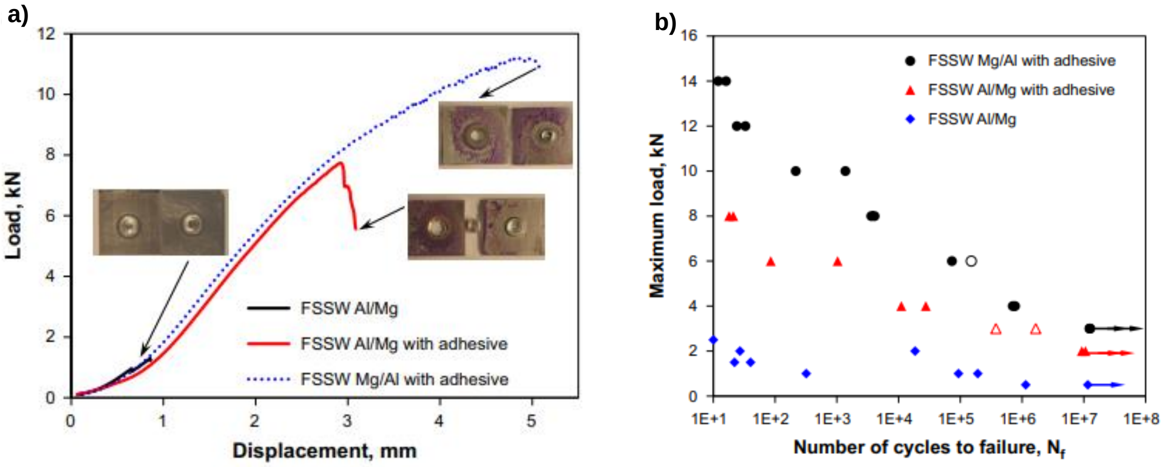

Figure 2.22: Properties of different Al-Mg joints: a) load-displacement curves and b) S-N curves [70].

As expected, hybrid joining resulted in a considerable increase in the joint's overall mechanical performance comparatively to the welded only. For the Hybrid joints, fatigue failure was dependent on the load applied: for higher loads corresponded to a failure through nugget pull out to while for lower loads failure happened in the bottom plate due to concentration stresses in the keyhole. Comparatively to welded only joints, Hybrid ones shown a significant increase, being even bigger the higher the cyclic load was.

Friction stir weld-bonding is another innovative method that is being currently study. The increase use of lightweight metals and dissimilar joints, like aluminium and magnesium, in the transport industry, makes technologies such as FSW desirable. But this technology, in the SLJ configuration, shows a great reduction in mechanical performance comparatively to the base material and so, an application of adhesive layer is seen as the option to overcome certain defects present in this type of joint, such as the hook defect.

The main conclusions from the previous studies [9,71,72] can be summarized in the following points:

- Hybrid joints show an increase up to 60% in tensile strength when compared to FSW only joints;
- Hybrid joints can reach a tensile strength as high as the AB joints, although ductility in far greater in the AB joints;
- Surface treatment is crucial to obtain a strong bond between the adherent and the substrate, with PAA anodization process showing a significatively increase in ductility when compared to sandblasting;
- Mechanical performance of the Hybrid joints at quasi-static loading can reach the performance of the AB joints, at best.

2.4 High strain rate testing

There are some additional considerations that need to be taken into account when the test loading goes from quasi-static to impact solicitations, mainly the effects of inertia and adiabatic softening [73]. That is why it is so important to test materials at different strain rates to quantify properly the change of their properties based on the solicitation of the medium. However, getting mechanical material properties for high strain rates might not be as easy as it looks, since it is hard to obtain noise free data without compromising the information related to the material deformation [74].

Strain rates can be divided into sixteen different orders of magnitude, ranging from creep, which can occur during years, to shock, characterized for nanoseconds spans [75], Figure 2.23.

Universal testing machines under quasi-static load conditions are usually used to mechanically characterize materials under 1D solicitations. As strain rate magnitude increases also the difficulty in create machines capable of reach such strain rate magnitudes increases. Universal testing machines are available and cover strain rates below the 1000 s^{-1} regime, as in the case of low cyclic fatigue specialized machines. Once this regime is passed, available commercial machine is scarce and mostly confined to government and university laboratories [75].

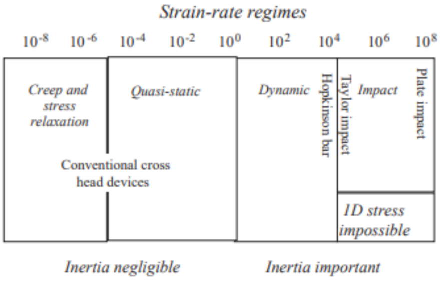

Figure 2.23: Schematic of strain rate regimes (in reciprocal seconds) with correspondent techniques, from [75].

In this thesis the focus will be on an intermediate regime of name dynamic. Some of the possible apparatus used for the experiments are the Drop-Weight (DW) and the Split Hopkinson Pressure Bars (SHPB).

2.4.1 Drop-weight

DW machines use a weight to provide compression load on a specimen. A weight is dropped from the top and it is guided along 1 or more shafts, depending on the size of the machine, striking the specimen before it reaches the limit of the shaft(s). Usually the bottom face of the weight carries a dart to impact the target.

This type of machines has some disadvantages, such as the impossibility of keeping a constant displacement rate throughout the experiment and the fact that trial tests are necessary to reach the right test operating conditions [74].

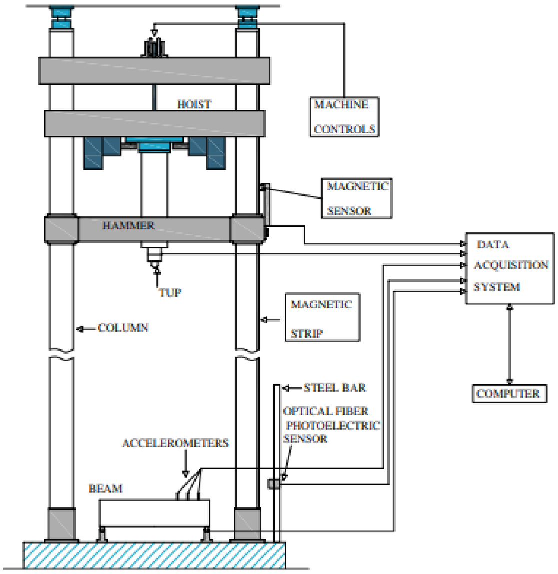

Figure 2.24: Schematic diagram of a DW impact machine for structural concrete, from [76].

Although this type of configuration can only perform compression tests (Figure 2.24), tension tests can be performed with some modification to the structure of the machine, as it will be shown in the next 2 examples.

2.4.1.1 Drop-weight high-speed tensile instrument I

Mott *et al* [77] proposed a modification to an existing Charpy-type pendulum capable of performing mechanical characterization of polymers at high strain ranges. This new machine, adapted from an MTS impact tester, is a derivation of the conventional drop-weight testing machines.

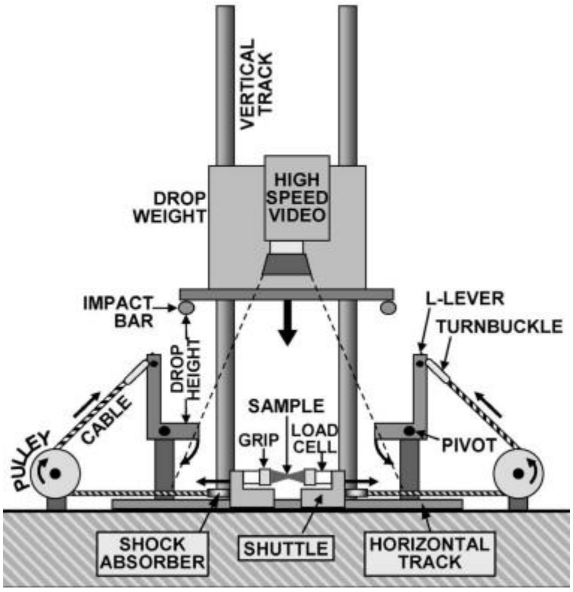

Figure 2.25: Schematic of the DW high-speed tensile instrument I, from [77].

Figure 2.25 shows the schematic of the DW. Underneath the released drop-weight there are 2 impact bars, one in each side, that will hit simultaneously the 2 L-levers. These levers, each one attached to a cable that passes around a pulley, will pull the cables in opposite directions, creating strictly horizontal movement on the shuttles connected to the ends of the specimen. Each test is recorded by a high-speed video digital camera attached to the drop-weight.

Note that to obtain meaningful results, it is necessary for the equipment to be in perfect symmetry, so that the forces applied on each side of the specimen remain equal throughout the experiment. For the maximum available drop-weight, speeds of 26 m/s on the shuttles can be achieved [77].

2.4.1.2 Drop-weight high-speed tensile instrument II

Kleiner *et al* [78] developed a variation of the DW machine mentioned previously. It uses the same principal, in the way that a weight is dropped from the top, but instead of having a rod to guide the weight it has vertical pipe where the weight is dropped.

In order to perform the tensile, the specimen is connected to a plunger on one side and a weight on the other side and, when it reaches a bottom barrier which has a hole with diameter smaller than the plunger, the specimen and the weight pass through it while the plunger abruptly interrupts its movement (Figure 2.26). This will allow the elongation of the specimen until its fracture.

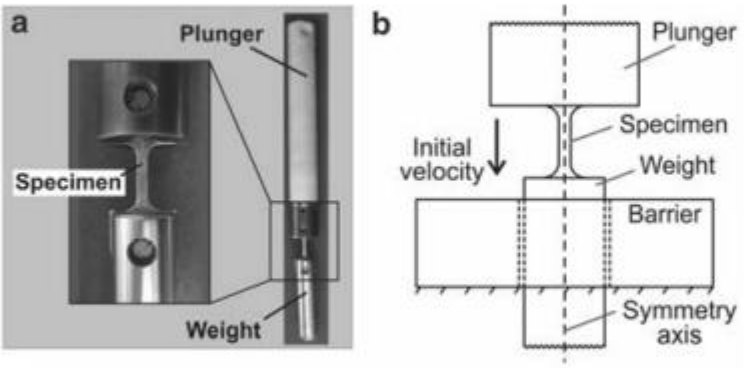

Figure 2.26: a) drop-weight mechanism and b) schematic of the barrier to stop the plunger, adapted from [78].

Each test is recorded by a high-speed camera attached to a mechanism that prevents the plunger from twisting. This system is capable of velocities until 11 m/s with free falling and, if more is needed, a pneumatic aid can be added to propel the plunger [78].

2.4.2 Split Hopkinson pressure bar

In 1872 John Hopkinson performed stress wave experiments in iron wires, fixed at one end and suddenly loaded on the other end, to identify if its fracture takes place near the impulse end or the fixed end [79]. This movement would lead to the development of the first experimental Hopkinson pressure bar technique in 1914, by Bertram Hopkinson, with the objective to measure the shape of a stress pulse in a long elastic bar [80]. Later, in 1949, Kolsky created an apparatus, with two elastic bars instead of one with the specimen in between, that could measure the dynamic stress-strain response of material under a compression loading [81]. From this point forward this apparatus is called Split Hopkinson Pressure Bar (SHPB) or Kolsky bar.

Since then, some features have been had or changed to improve the results obtained. Some of that changes include different type of launch systems, like gas guns and electromagnetic cannon, proper data acquisition systems and capability of reproducing different type of tests, adding to the compression test the tension, torsion and tri-axial loadings.

Although there is not a standardized test due to complexity inherent to data analysis and inertia effects on the specimen, there are some key points shared by all [74]:

- Two long symmetrical bars (one incident and one transmission bar);
- Bearing and alignment fixtures to allow free movement of the bars and maintain optimal axial alignment;
- Launch system to accelerate the striker bar;
- Strain gauges mounted on the bars;
- Data acquisition systems.

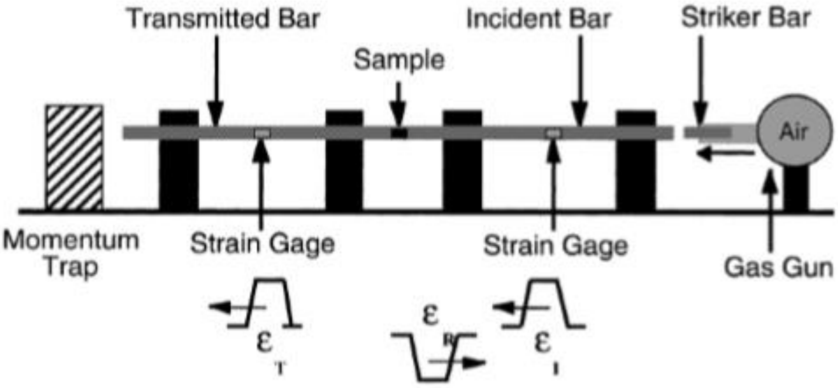

Figure 2.27: Schematic of a SHPB for compression loading, from [74].

In compression loading (Figure 2.27), a sample of the material is sandwiched between the two bars. Then, a striker bar, usually accelerated by a gas gun, hits the incident bar generating an elastic wave pulse. This wave propagates through the bar and, once the end is reached, one part of the wave is reflected and the other is transmitted to the sample. The analysis of these waves using strain-gages allows to obtain the displacements and acting forces on both sides of the specimen.

For the results acquired previously to be valid it is essential that the wave propagation is unidimensional along the pressure bars and that the specimen deformation is uniform.

This method has some clear disadvantages, such as the high operation noise due to the expansion of the air, very high air pressure if high strain-rates are trying to be reached and overall length of the apparatus [74].

2.4.2.1 Split Hopkinson pressure bar in tension

Once again, despite its nature to perform compression tests, SHPB can perform tension tests with some modifications on the geometry of the specimen and its fixation to the bars. There are mainly 3 types of tension bars.

The first one is the top hat specimen [82] in which very few modifications are needed because it uses the same compressive pulses needed for the compression SHPB. The difference is in the transmission bar, in this case hollow with the same cross-sectional area as the incident one. The hardest part on this apparatus is the specimen, which needs to be machined with a top hat shape, as shown in Figure 2.28.

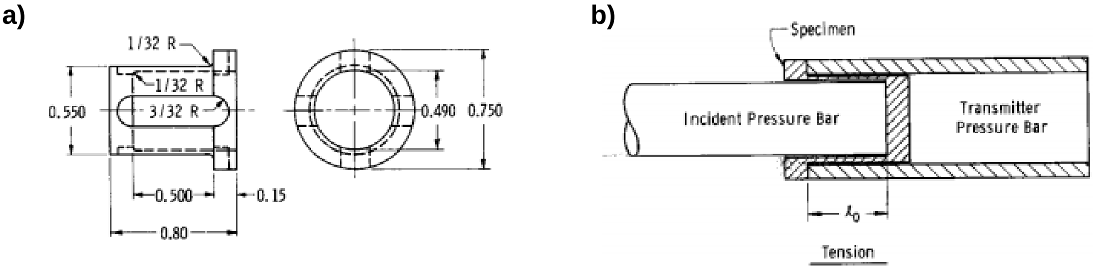

Figure 2.28: a) top hat specimen and b) specimen configuration, adapted from [82].

Another type of tension bar is one that uses a reflective compression pulse [83]. This setup is very similar to the compression one, with the exception being in the area around the specimen. In this case a threaded specimen and, most important, a protective shoulder for the specimen are used, as shown in Figure 2.29.

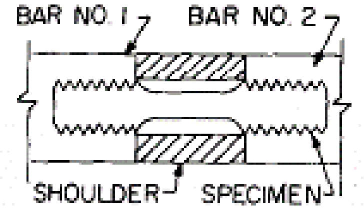

Figure 2.29: Specimen configuration, adapted from [83].

A striker bar hits the bar number 1, generating a compressive pulse until it reaches the specimen. At this point, the shoulder, placed tightly between the pressure bars after the fixation of the specimen, assures the transmission of the entire compressive wave through it, so that the elastic limit of the specimen is not overstepped. Once it reaches the end of the bar number 2, the wave is reflected and travels back as a tensile pulse, reaching the specimen, where it is partially transmitted to it and the rest reflected back to bar number 2.

Finally, there is the direct acting tensile bar where a threaded specimen between the incident and transmission bars is used and it is generated a tensile pulse on the end of the incident bar. This can be achieved by many ways, being the most efficient one the use of a transfer connection attached to the end of the incident bar that will be loaded by a compressive wave transmitted by the loading bar, as shown in Figure 2.30.

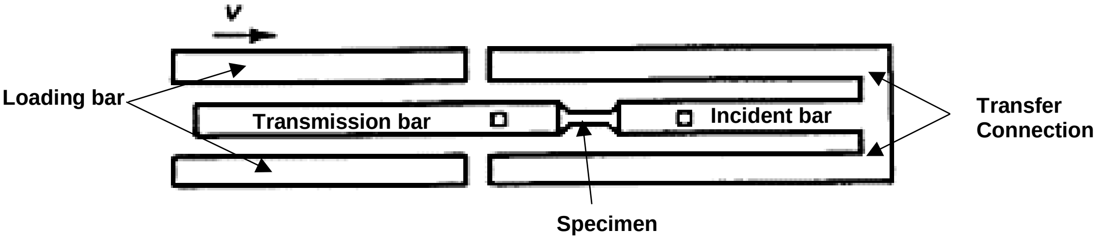

Figure 2.30: Schematic of a direct acting tensile SHPB, adapted from [74].

In this method there is the drawback of covering the specimen, making it difficult implement measurement techniques. Two simple ways to avoid this is to make use of a weight or explosives to impact directly the anvil, instead of having a loading bar. However, this increases the difficulty to achieve a constant pulse amplitude [74].

To overcome those problems, two more viable ways were further developed for loading the incident bar. The first was accomplished through the use of a static loading by having a clamp which only allowed to apply a load to the end of the incident bar that does not have the specimen. Once the clamp is released, the load travels to the other end of the incident bar, specimen and transmitted bar, as seen in Figure 2.31. This method allows the possibility to measure the pre-load applied on the incident bar, making it simple to replicate the experiment done [84].

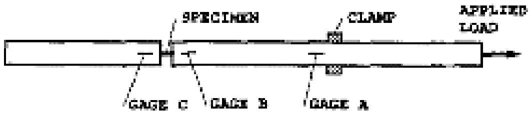

Figure 2.31: Schematic of a static loading tensile SHPB, adapted from [84].

The second one consisted in using a hallow striker bar around the incident bar, Figure 2.32. A fire gun fires the hallow striker bar, traveling along the incident bar until it reaches a flange, creating the tensile wave on the incident bar.

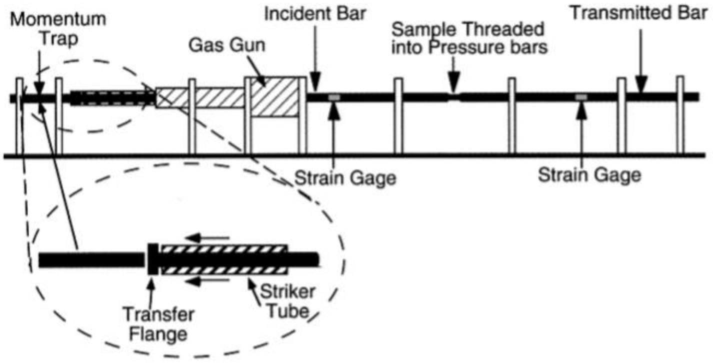

Figure 2.32: Schematic of a dynamic loading tensile SHPB, from [74].

2.4.2.2 Electromagnetic compressive split Hopkinson bar

Silva *et al* [85] developed a prototype for a new compressive split Hopkinson bar, in Figure 2.33. The biggest difference on this prototype is the use of an electromagnetic actuator to propel the striker (ram) bar (see Figure 2.34).

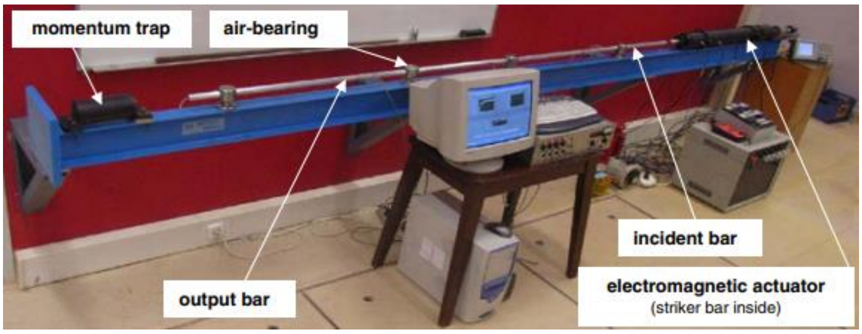

Figure 2.33: Prototype of the electromagnetic compressive split Hopkinson bar, from [85].

This mechanism uses a bank of capacitors (each with 6 mF) to store the energy needed. Once all the capacitors are ready, they will fire simultaneously to its respective coil, generating the pressure needed to accelerate the striker bar. Although the current pulse is in the order of the milliseconds, it is enough to generate velocities on the striker bar up to 18 m/s [86].

The aforementioned mechanism has some clear advantages over the previously mentioned conventional SHPB, namely its high repeatability and flexibility, since it is easy not only to change the striker bars used but also the amount of energy stored in each capacitor, with each one being independent and possible to be switch off, virtually allowing an infinite adjustable range of experimental velocity tests.

Overall performance also improves by reducing the set-up time when compared to conventional compressed air systems.

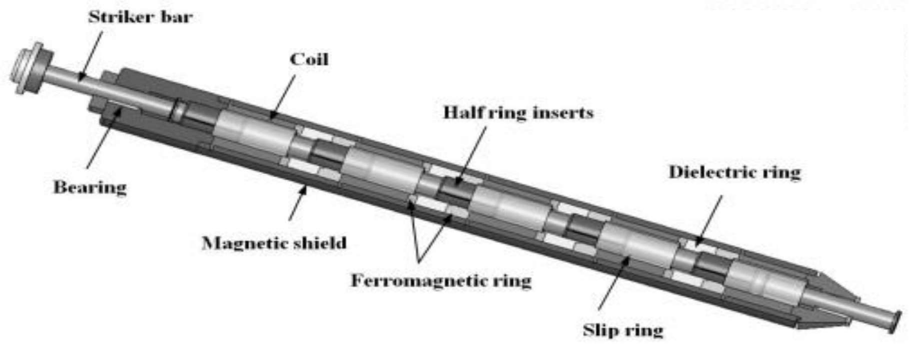

Figure 2.34: Inside of the electromagnetic actuator, based from [85].

This electromagnetic actuator has proved its good performance and good agreement with literature data by performing compression tests on technically-pure Lead to show the impact that strain-rate has on the response of metallic materials [85] and also by successfully demonstrate its capability to perform the mechanical characterization of the materials subjected to metal cutting [86].

Chapter 3

Experimental development

In this chapter, the experimental research conducted during this thesis will be presented. Firstly, a description of the materials is presented, followed by the procedures used to manufacture the different joints. Finally, a description of the equipment and parameters of the tests performed is given.

3.1 Single Lap Joints Manufacturing

Three different types of single lap joints were produced: Friction Stir Welded joints (FSW), Adhesive Bonded joints (AB) and Hybrid joints (FSW+AB). In the case of the Hybrid joints, the method chosen to manufacture them was the “weld-through” method since it is the method that allows an easier industrialization of the process.

3.1.1 Material characterization

3.1.1.1 Base Material

The base material used for all the three type of joints produced (AB, FSW and FSW+AB) was the AA6082-T6 supplied in the form of 2 mm thickness sheets. This is an aluminium alloy from the series AA6XXX, composed mainly by magnesium and silicon, that suffered a T6 heat treatment achieved by solution heating at approximately 530ºC followed by artificial aging at approximately 180ºC. During artificial aging, the material endures precipitation hardening, forming β’’ and β’ phases [87].

The following tables (Table 3.1 and Table 3.2) present the chemical composition and the mechanical properties, respectively. However, during the welding procedure temperatures achieved are enough to change the mechanical properties.

Table 3.1: Chemical composition of aluminium alloy AA6082-T6 [88].

Cr [%]	Cu [%]	Fe [%]	Mg [%]	Mn [%]	Si [%]	Ti [%]	Zn [%]	Others [%]	Al [%]
≤ 0.40	≤ 0.10	≤ 0.50	0.60 - 1.20	0.40 - 1.0	0.70 - 1.30	≤ 0.10	≤ 0.20	≤ 0.15	Balance

Table 3.2: Mechanical properties of aluminium alloy AA6082-T6 [89].

Density [Kg/m^3]	Young’s modulus [GPa]	Ultimate tensile strength [MPa]	Yield tensile strength [MPa]	Elongation at break [%]
2700	69	330	270	9.8

3.1.1.2 Adhesive

The adhesive used for the adhesive bonded and the Hybrid joints (AB, HYB) was the Araldite 420 A/B from Hunstman®. It is a two-component epoxy system capable of curing at room temperature. It is characterized for its high shear and peel strength, toughness and good moisture resistance. If cured at room temperature, it takes 4 to 5 days to achieve 90% of adhesive's full strength and up to 2 weeks to obtain its full strength. Heating will accelerate the process, reducing its curing time to 1h when heated at 120ºC [90].

Table 3.3 presents some properties of both the components by themselves and mixed.

Table 3.3: Adhesive properties, adapted from [90].

Property	Araldite 420 A	Araldite 420 B	Mixture Adhesive
Colour	Yellow	Blue	Dark green
Specific gravity	1.2	1	1.1-1.2
Viscosity at 25ºC [*Pa.s*]	100-300	0.6-1.4	35-45
Gel time	-	-	60
Lap shear strength [*N/mm*^{2}] (Cured at room temperature)	-	-	37

3.1.1.3 Surface Treatment product

For the manufacturing of the Hybrid joints (HYB), the 3M® product AC-130 was chosen for the last step of the surface pre-treatment of the joints. This product is a sol-gel and it is a substitute of anodization. The interaction between the product and the material surface can enhance adhesion properties with results similar to phosphoric acid anodization (PAA) treatment while adding the advantages of being a faster process and reducing the hazardous waste produced in the process [91,92].

3.1.2 Joint geometry

FSW and HYB joints were manufactured with an overlap length of 40 mm in which each initial sheet used had the following dimensions: 300x135x2 mm. For the AB joints an overlap length of 40 mm and 12.5 mm was used, and, in this case, each sheet was previously cut, having the dimensions of 135x25x2 mm and 107.5x25x2 mm, respectively. A 95 mm adherent arm was used for every joint produced. Cross section for the FSW, Hybrid and AB with 40 and 12.5 mm overlap joints are represented in Figure 3.1.

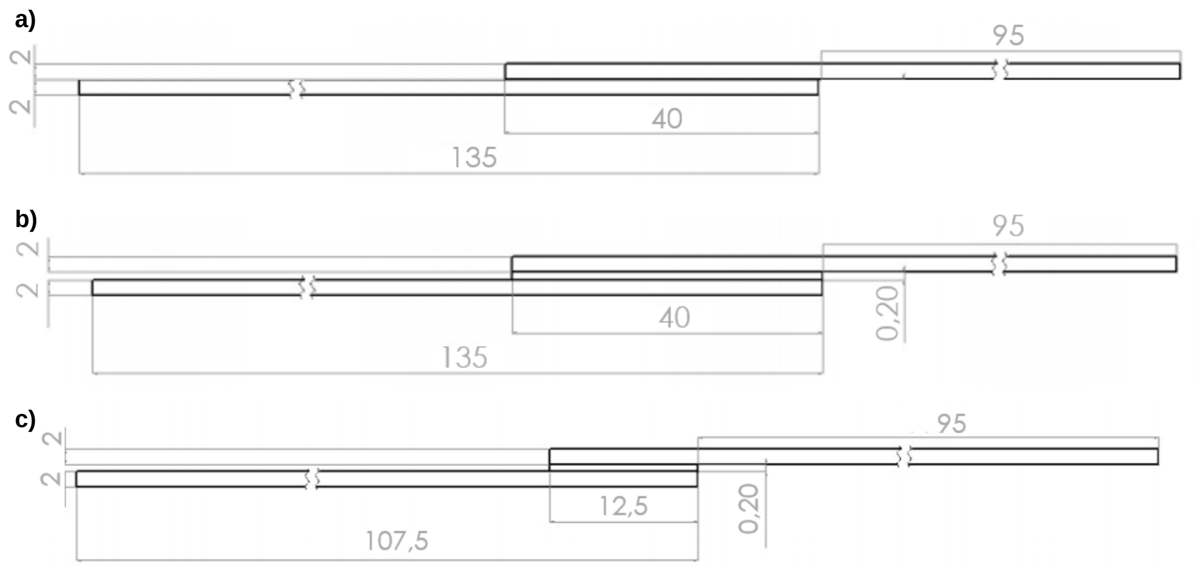

Figure 3.1: Joint cross section (not to scale): a) FSW 40 mm overlap, b) Hybrid and AB 40 mm overlap and c) AB 12.5 mm overlap.

3.1.3 FSW equipment

The machine used to perform both FSW and Hybrid joints was the FSW ESAB® Legio 3UL numeric control machine (Figure 3.2) from the Manufacturing and Process Technology Laboratory at Instituto Superior Técnico.

This machine has 3 degrees of freedom (x,y,z) and can be controlled either by position or force control. A water refrigeration system is used in this machine to keep spindle shaft and the tool from reaching high temperatures during the process which could ultimately compromise the tool's integrity.

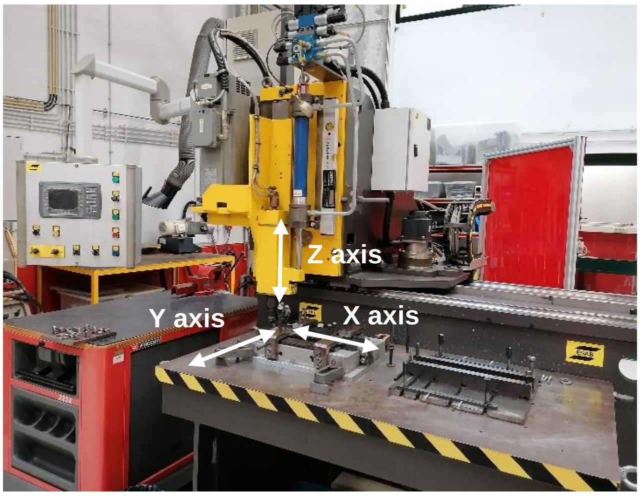

Figure 3.2: FSW ESAB® Legio 3UL numeric control machine.

Figure 3.3 presents the tool, developed at IST [93] and used in this work, which is composed by a shoulder of a 16 mm diameter, with a cylindrical pin with a diameter of 5 mm attached to it. The tool body is made of DIN Ck45 steel and the shoulder and pin are made of AISI H13 tool steel. In this experiment probe length was kept at 3 mm to promote an optimal mixture of the stirring zone and machine's zero referential for Z axis was set to be on top of the top sheet to be weld.

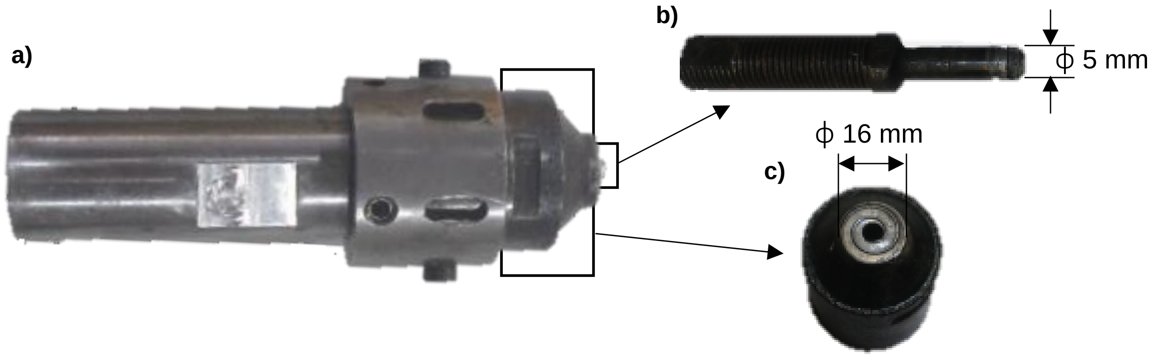

Figure 3.3: FSW tool components: a) tool body, b) tool pin and c) tool shoulder.

3.1.4. FSW and Hybrid joints experimental procedure

The experimental procedure to manufacture Hybrid joints specimens consisted in the following steps:

1. Surface Preparation
2. Clamping and adhesive lay-up
3. FSW process
4. Curing process
5. Specimen cutting

Due to the similarities of the FSW and Hybrid joints procedures both will be described together. Manufacturing FSW joints does not need the adhesive lay-up part from step number two neither step number four, which is the cure of the adhesive.

3.1.4.1 Surface preparation

Each aluminium sheet in this experiment received a surface treatment on the overlap area that consisted in 3 steps. The first one was abrading which is done with 240 grit sandpaper, along the longitudinal, transverse and 45º directions, with the objective of removing the oxides and impurities present on the aluminium surface.

The following step was to degrease the surface with acetone.

For the Hybrid joints, an additional surface chemical treatment was needed to promote better adhesion. The AC-130 sol-gel from 3M was used. This product comes in a 2 component parts, part A and B, that need to be mixed with a glass steering rod. Once it is well mixed, the mixture needs to rest for 30 minutes before it can be applied to the surfaces to be bonded. Once resting period is over, the surface is carefully soaked with this liquid for a minute. After its application, sheets should rest for 60 minutes under ambient conditions and contacts with the surface should be avoided to not damage the coating. A schematic of the process is shown in Figure 3.4.

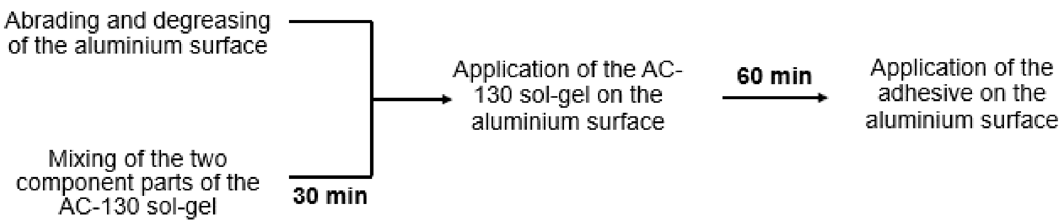

Figure 3.4: Schematic of the surface treatment applied to the Hybrid joints.

3.1.4.2 Clamping and adhesive lay-up

For the manufacturing of the Hybrid joints it is of good practice to start by applying a demoulding coating on the surfaces of the clamping system and shims to prevent the adhesion of the joint. In this case, the release agent used was the Frekote® 770-NC from Loctite®.

Once the bottom aluminium sheet is correctly fixed, the adhesive is applied on its surface. The application is performed with a pistol that has a nozzle mixer on in to combine both parts of the epoxy. To assure a continuous thickness length of the adhesive along the weld, two 0.2 mm thick calibrated metal stripes were position below each shim.

After positioning the top sheet, the clamping system is fastened and the sheets are ready to be welded (Figure 3.5).

Figure 3.5: Clamping system fastened.

Note that this clamping system had the objective of reducing the residual stresses caused by clamping forces and to reduce the distortion and possible movement of the sheets, by applying strong horizontal and vertical clamping forces. It is of extreme importance its use to produce good quality specimens since its function consists in pressing the sheets against each other and keeping them fixed and flat throughout their length, without letting them rise.

3.1.4.3 FSW process

For the FSW process, the set of parameters chosen to produce reliable joints were based on previous literature experiments [9,71,72], and are presented in Table 3.4:

Table 3.4: Parameters used to manufacture FSW and Hybrid joints.

Parameters	Values	
	FSW joints	Hybrid joints
FSW control	Downward force (450 kgf)	Downward force (450 kgf)
Rotational direction	Clockwise	Clockwise
Tilt angle [º]	0	0
Pin length [mm]	3	3
Plunge speed [mm/s]	0.1	0.1
Dwell time [s]	7	14
Welding speed [mm/min]	200	200
Rotational speed [rpm]	1000	1000
Plunge depth (zero at top sheet) [mm]	-3.1	-3.2

The plunging and dwelling stages are performed in position control, allowing a precise penetration of the tool on the sheets by adjusting the load. Once the dwell time is finished, control is switch to force control since it allows to maintain the force throughout the all process, adjusting the position of the tool when misalignments of the sheets or small slopes on the worktable are present.

3.1.4.4 Curing

Although Hybrid joints are subjected to a peak of temperature during the welding phase, a curing time of two weeks at room temperature was still applied so that these joints could achieve full strength.

3.1.4.5 Specimen production

During this experimental work, 2 FSW and 5 HYB joints were produced. The specimens used for the tests were cut according to Figure 3.6.

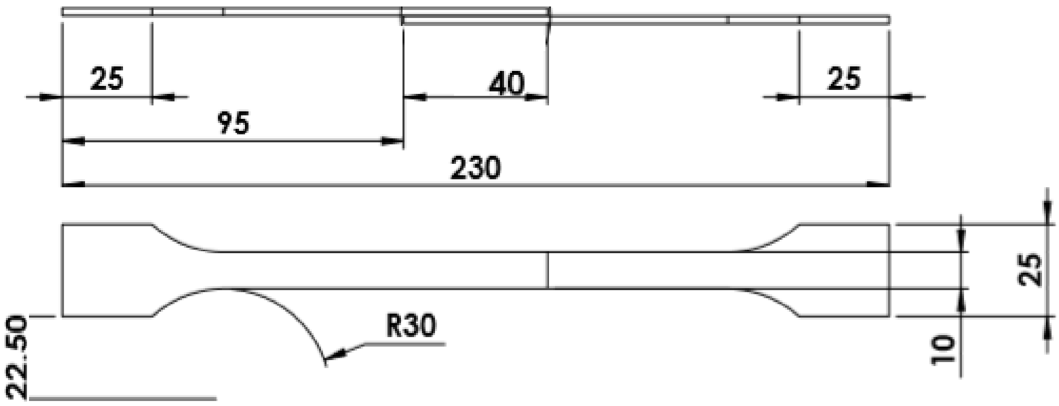

Figure 3.6: Specimen with 40 mm overlap geometry.

3.1.5 Adhesive joints experimental procedure

The experimental procedure to manufacture adhesive joints consisted in the following steps:

1. Surface Preparation
2. Mould preparation
3. Curing
4. Specimen cutting

Adhesive joints with 40 mm overlap were both manufactured at Instituto Superior Técnico (IST) and at Instituto de Ciência e Inovação em Engenharia Mecância e Engenharia Industrial (INEGI). Adhesive joints with 12.5 overlap were only manufactured at the latter site.

3.1.5.1 Surface Preparation

Surface preparation is similar to the one described for the Hybrid joints with the exception that instead of using the 3M® product AC-130 in the last step, phosphoric acid anodizing was used. This surface treatment was performed according to ASTM D3933-98 standard [94]. A bath of phosphoric acid solution with 12 wt% of phosphoric acid and 88 wt% of distilled water was initially prepared inside a tank. An experimental setup was designed to hang the sheets over the bath and allow a partial immersion on it. According to the standard, to anodize *n* parts, *n* + 1 cathodes are needed. In this case, due to the small area of the anodes, big area of the cathode and after trial and error, each anodization anodized 12 sheets using 1 cathode. An AC-to-DC power supply is connected to the anode (aluminium) and to the cathode (stainless steel), as seen in Figure 3.7, producing a constant voltage of 20V and 3A for 20-25 minutes. Inside the tank is also a small pump that promotes stirring and continuous flow of the bath.

Once the time is over, anodized sheets are carefully removed, cleaned with distilled water and dried. To reduced possible contamination sources, anodized sheets are wrapped in aluminium foil. In the standard is suggested the application of the adhesive within 72 hours. In this case, adhesive was always applied within 1 hour.

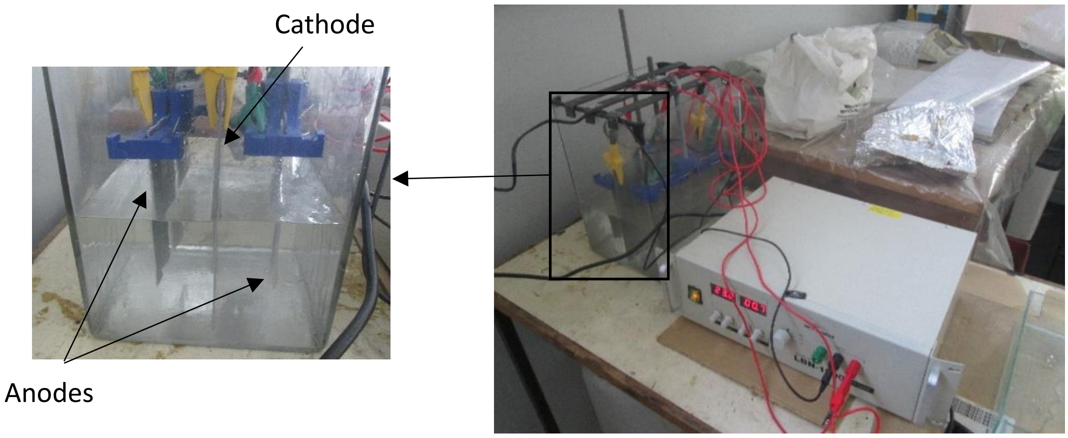

Figure 3.7: PAA experimental set up.

3.1.5.2 Mould preparation

First it is necessary to degrease and apply the release agent Marbocote® HP7 on the surfaces that close the mould and on the shim and spacers to guarantee a complete demoulding upon cure.

To manufacture more efficiently, 6 adhesive bonding joints will be produced in each batch, which corresponds to the full capacity of the mould. Bottom sheets and respective shim are displayed on the top of the bottom mould, restrained by PTFE pins. Adhesive is applied on top of the bottom sheets with the help of a pistol with a nozzle mixer.

After this, top sheets and shims are positioned, and the mould can be closed. Figure 3.8 shows the described apparatus immediately before closing the mould, including the 4 metal stripes used to assure the uniform thickness of the adhesive layer.

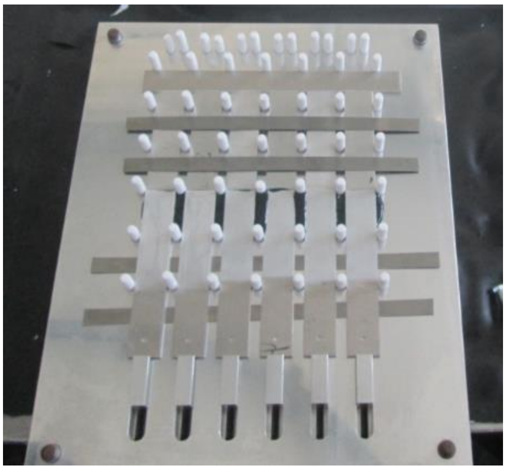

Figure 3.8: Mould positioned right before closing.

Two similar moulds (Figure 3.9) were used to perform the joints since two different laboratories were used to manufacture the joints. At INEGI three batches were produced and at IST two batches. After manufacturing the first batch at IST, due to the cure parameters implemented and problems with the release agent application, it was realized that some modifications needed to be done on the mould in case of the adhesive fails to reach a proper cure or in case of the joint bonds to the mould . So, sixty extra holes were made, with a pillar drilling machine, on the centre of the mould.

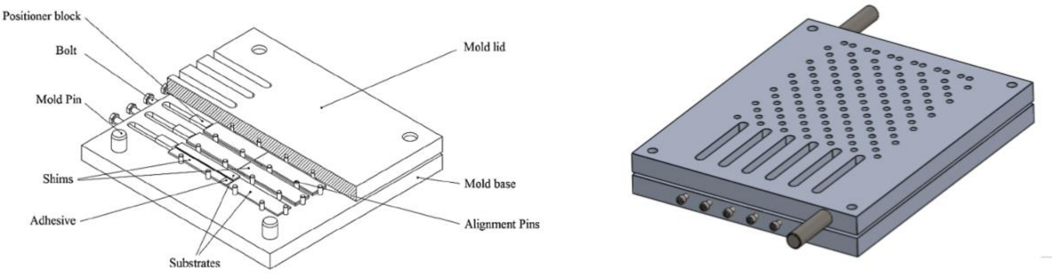

Figure 3.9: Schematic of the first and second moulds, cut view on the left and closed on the right, respectively.

3.1.5.3 Curing

For the batches manufactured at INEGI, curing of the adhesive bonding joints was done in a hot plate hydraulic press, with time, temperature and pressure control (Figure 3.10 a)). For the batches manufactured at IST a hot plate pneumatic press, also with time, temperature and pressure control was used (Figure 3.10 b)). Due to machine restrictions related to the pressure output of this press, the mould was wrapped in a vacuum bag, with two connections connected to a vacuum pump with an auxiliary chamber to try to simulate a vacuum environment and compensate the maximum allowed pressure of the press. Time of the manufacturing was also increased.

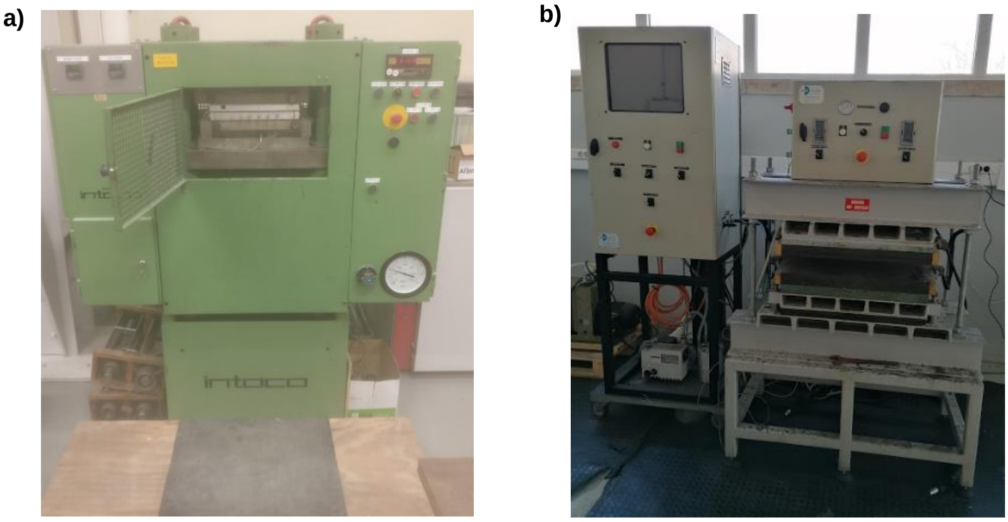

Figure 3.10: Hydraulic and pneumatic hot plate presses, respectively.

In Table 3.5, manufacturing parameters for both presses are detailed. Manufacturing time does not include the first 20~30 minutes that it takes for the plates to reach curing temperature.

Table 3.5: Adhesive joints manufacturing parameters.

Parameters	Hydraulic press	Pneumatic press
Pressure [bar]	11	3.5
Temperature [ºC]	120	130
Time [h;min]	1 h 45 min	2 h

3.1.5.4 Specimen cutting

After removing each joint from the mould, AB with 40 mm overlap specimens used for the tests were cut with the same geometry as the Hybrid ones (see Figure 3.6), whereas AB with 12.5 mm overlap specimens were cut according to Figure 3.11.

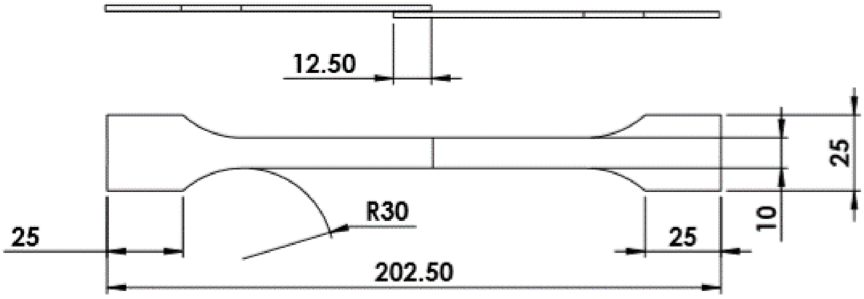

Figure 3.11: Specimen with 12.5 mm overlap geometry.

3.2 Microscopic analysis

To perform microscopic analysis, the FSW and Hybrid specimens were prepared by cutting a cross section sample covering the overlap of the joint and placing it in a mould filled with an epoxy resin mixed with hardener.

After a 24 hour rest the sample is ready for sanding and polishing. On the side of the sample that is going to be observed microscopically, polishing of the surface is done using the Struers® DAP-7 automatic polisher. First it was used sandpaper disks with increasing grit (240-320-600-800-1000-2400-4000). During this stage a lubricant water type is used and every time the sandpaper is switch the sample should rotate 90° so that the polishing is the most uniform possible. After the last disk is used, the sample goes to an ultrasound cleaner so that the residues left from the sandpapers are removed before the final polishing treatment. For this final polishing it was used the 3 μm and 1 μm diamond compound polishers, sequentially, and it was used a diamond suspension as lubricant.

To evaluate the microstructural evolution the samples previously treated were etched with a Keller's reagent, with a composition of 95.5 ml of water, 2.5 ml of nitric acid, 1.5 ml of hydrochloric acid and 0.5 ml of hydrofluoric acid.

The microscope used for the analysis was the Olympus CK40M (Figure 3.12) with increasing magnification values.

Figure 3.12: Olympus CK40M microscope.

3.3 Microhardness test

The samples used for the microscopic analysis were later subjected to a microhardness evaluation with the objective to characterize the mechanical and structural properties of the joint and to aid the development of the numerical simulation. The test consisted in applying indentations with a load of 0.2 HV (1,961 N) during 10 sec, spaced by 0.3 mm on a straight line. A total of two parallel straight lines, that are 1 mm away from the top and from the bottom sheets, respectively, were defined.

The machine used for the analysis was the HMV-2 micro hardness tester from Shimadzu (Figure 3.13).

Figure 3.13: Shimadzu HMV-2 microhardness tester machine.

3.4 Tensile tests

To assess the tensile mechanical properties of the FSW, AB and Hybrid joints at a wide range of strain rate, quasi-static and impact loading tests were performed. Also, adhesive mechanical behaviour at high strain rate was assessed.

3.4.1 Bulk dynamic test

To assess the mechanical behaviour of the adhesive, an SHTB apparatus was used to perform the adhesive bulk tests, at INEGI (Figure 3.14). Bulk specimens were cured at 120 °C for 1 hour, similar to the cure implemented for the AB joints manufactured at INEGI (see section 3.1.5.3).

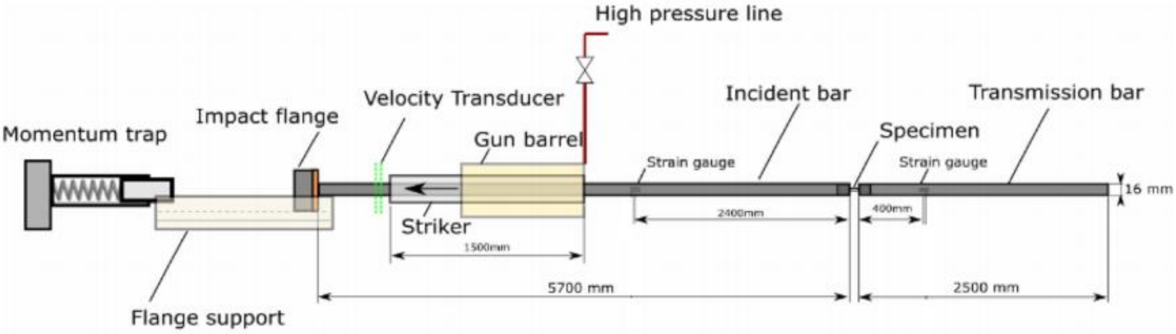

Figure 3.14: Schematic of the split Hopkinson tension bar setup, adapted from [95].

The apparatus is comprised by a striker, an incident and a transmission titanium alloy bars with a diameter of 16 mm. The length of the bars are 1500 mm, 5700 mm and 2500 mm, respectively. Strain gauges are placed within 2400mm and 400mm from the incident bar/specimen and transmission bar/specimen interfaces. Specimen is placed between the incident and transmission bars. A striker hollow bar, supported by a bushing and a pneumatic support with pressurized air to reduce sliding friction on the bar, is propelled by a gas gun at 11 m/s (pressure of 3 bar), hitting the flange of the incident bar and, consequently, tensioning the specimen until failure.

Velocity data is measured with a linear encoder mounted after the pneumatic support and stress-strain curve of the sample is calculated using the equations of the average engineering stress and engineering strain of the specimen, respectively, for 1-wave analysis of the SHPB, given by [96]:

$$\sigma_s(t) = \left(\frac{A_B E_B}{A_{S0}}\right) \times \varepsilon_t(t) \tag{3.1}$$

$$\varepsilon_s(t) = \left(\frac{2c_0}{H_{S0}}\right) 1 \times \int^t \varepsilon_R(t)\, dt \tag{3.2}$$

Where A_B is the cross-sectional area and E_B is the Young's modulus of the pressure bar, A_{S0} and H_{S0} the original cross-sectional area and thickness of the specimen, respectively, c_0 is the bar wave velocity and ε_t and ε_R the strain measured on the bars of the transmitted and reflected pulses, respectively.

Specimens were tested at a strain rate of 267 s^{-1} and geometry of the specimen used is detailed in Figure 3.15.

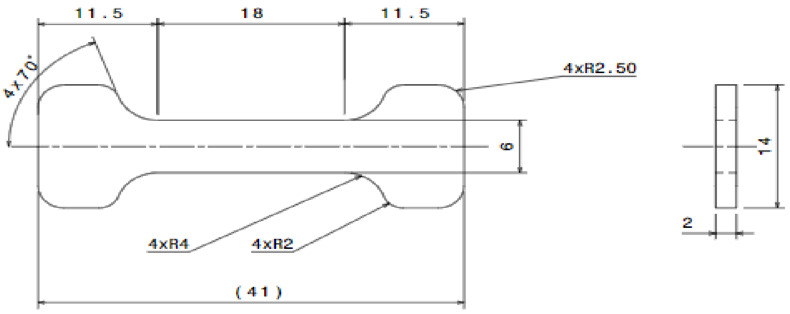

Figure 3.15: Adhesive bulk specimen geometry.

3.4.2 Quasi-static tests

For the quasi-static experiments, tests were performed using the INSTRON® 5566 (Figure 3.16) testing machine equipped with a load cell with a maximum capacity of 10 kN. For each experiment, two 2 mm thick shims were used to align the specimen with the machine loading axis, avoiding the formation of a bending moment.

All joints were tested at a constant displacement rate of 1 mm/min. AB joints with a 40 mm overlap manufactured at IST were also tested at 100 mm/min.

Figure 3.16: INSTRON® 5566 testing machine.

For the base material specimens, INSTRON® 3369 (Figure 3.17) testing machine equipped with a load cell with a maximum capacity of 50 kN was used. Tests were performed at 1 mm/min and 100 mm/min displacement rates.

Figure 3.17: INSTRON® 3369 testing machine.

3.4.3 Impact tests

A purpose made testing device was made to perform the impact experiments, as seen in Figure 3.18. The electromagnetic actuator introduced and explained in section 2.4.2.2 was used to propel a striker bar. The striker bar hits a transmission bar that slides on top of 3 guides. While one of the ends of the specimen is restrained, the other one is fixed with a bolt to the top of the transmission bar. This system allows the pulling of the specimen in only one direction, executing a tensile test at much higher speeds than the quasi-static ones.

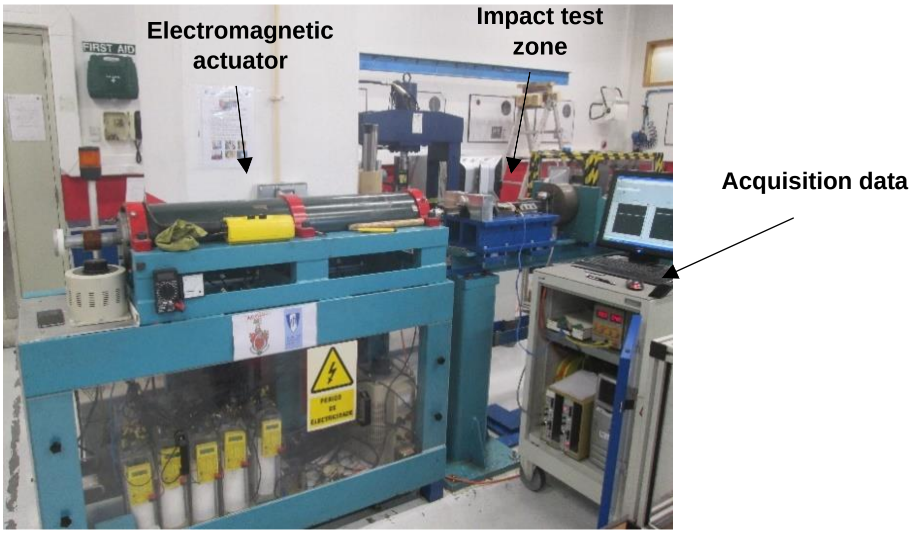

Figure 3.18: Impact test apparatus.

Specimen load and displacement data was acquired by a load cell and a displacement transducer, respectively (Figure 3.19). Displacement data and duration of the test were later used to compute velocity’s impact.

Tests were performed for various velocities by changing the energy stored in each capacitor. For some experiments, an additional mass was inserted inside the striker bar so that the impact had a higher energy and was able to fracture the specimen for the same test velocity.

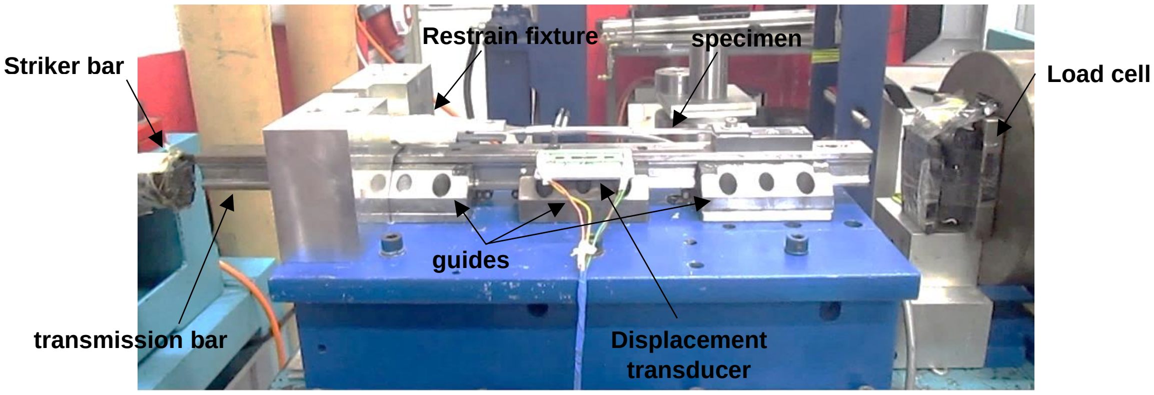

Figure 3.19: Impact test zone.

Chapter 4

Experimental Results

In this chapter, results obtained during the experimental studies are presented and discussed. In the first half of these chapter characterization of the materials and the FSW and Hybrid joints is done. The second half of these chapter addresses the quasi-static and the impact tests for the AB, FSW and Hybrid joints.

4.1 Base Material characterization

Base material specimens were tested to understand the joint efficiency of the manufactured joints. BM specimens were tests at 1 mm/min and 100 mm/min displacement rates, and with the grain on the longitudinal (LT) and long transverse (TL) directions.

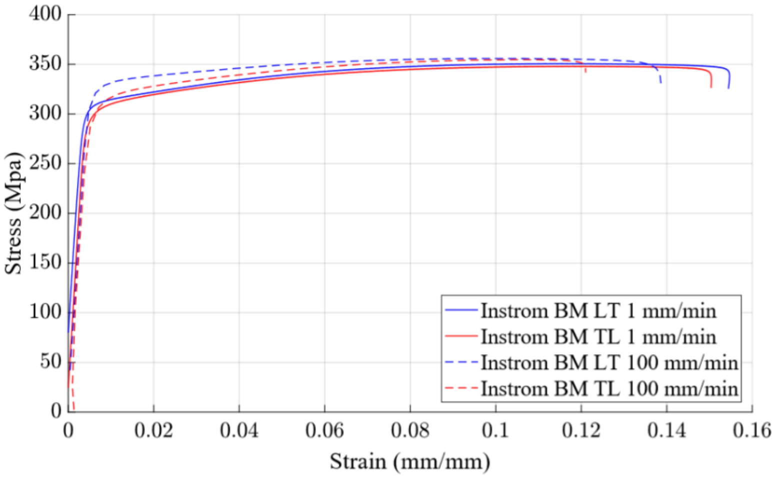

Figure 4.1: Representative load displacement curves for BM specimens at 1 mm/min and 100 min/min.

From the Figure 4.1 and Table 4.1 it is possible to conclude that, for this type of aluminium, grain direction does not play a significant role on the specimen's performance, with differences in maximum load below 1%. Ductility differences reached 8%, although might not be totally accurate since specimens fractured almost always on the limits of the clip gauge. Another point to keep in mind is that, while AA6082-T6 showed low strain rate sensitivity for flow stress, with differences below 2% in the UTS when going from $10^{-4}\ s^{-1}$ to $10^{-2}\ s^{-1}$, which is coherent with literature [97], rate sensitivity for ductility was found to be around 12%, which is a considerable value but could have partially been due the under-measurement of the elongation at break, given that most specimens rupture occurred on the limits of the clip gauge, which can have caused pressure points to fracture.

Table 4.1: Characteristics of the lap shear strength tests of the different joints.

Joint	Maximum load [N]	Maximum displacement [mm]	UTS [MPa]
BM LT	$7141.83 \pm^{30.32}_{56.57}$	$10.38 \pm^{1.25}_{0.99}$	$348.41 \pm^{2.34}_{3.79}$
BM LT 100	$7198.19 \pm^{62.31}_{84.57}$	$8.97 \pm^{1.45}_{1.80}$	$352.89 \pm^{4.56}_{7.57}$
BM TL	$7076.03 \pm^{50.14}_{40.07}$	$11.08 \pm^{0.26}_{0.43}$	$348.00 \pm^{1.32}_{1.40}$
BM TL 100	7240.91 ± 65.44	9.40 ± 0.18	354.95 ± 0.27

4.2 Adhesive mechanical characterization

Mechanical performance of the adhesive was assessed in tensile tests on bulk adhesive specimens cured at 120ºC. A SHPB was used to perform these tests at a strain rate of 267 s^{-1}. A representative stress-strain curve for these results was compared with the curves obtained previously for lower strain rates on a tensile machine, as seen in Figure 4.2.

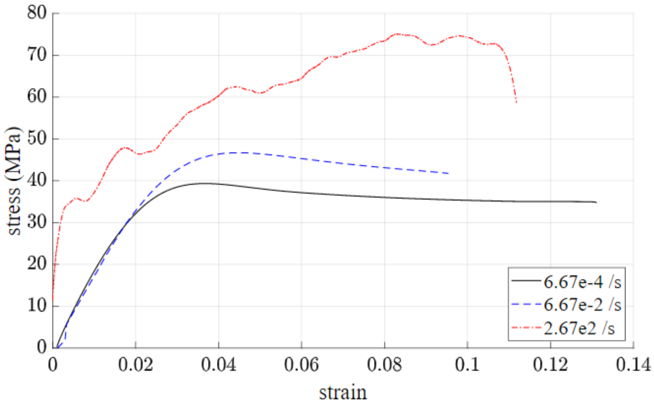

Figure 4.2: Representative stress-strain curves for the tensile bulk test.

The combination of these results allowed the estimation of the UTS values in a strain rate range up to the magnitude of the $10^2\ s^{-1}$ (Figure 4.3). From this tests, it was noticed that, although strengthening of the adhesive is increasing in an exponential trend with the increase of the strain rate, ductility is highest for lower strain rates and continuously decreases up until strain rates in the magnitude of the $10^{-2}\ s^{-1}$. At this point, trend seems to invert and starts to rise again, although it is difficult to reach a conclusion due to the scatter present in the strain at failure measurements.

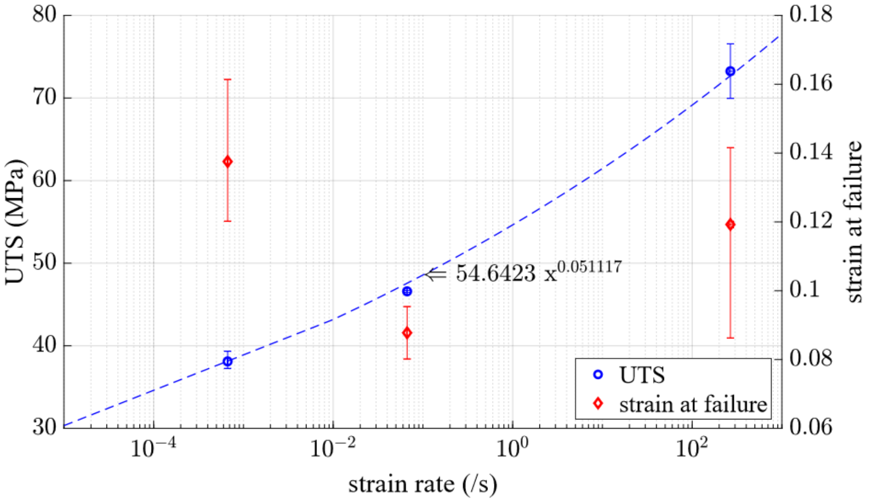

Figure 4.3: Adhesive's UTS and strain failure strain rate dependency.

4.3 Microstructural evaluation

As discussed before, FSW is a process where thermal cycles mixed with plastic deformation lead to recrystallization of the base material, which results in grain refinement and a change in the welded material properties. The welded material will have different zones with different mechanical properties that influence weld behaviour. A representation of the new zones is shown in Figure 4.4.

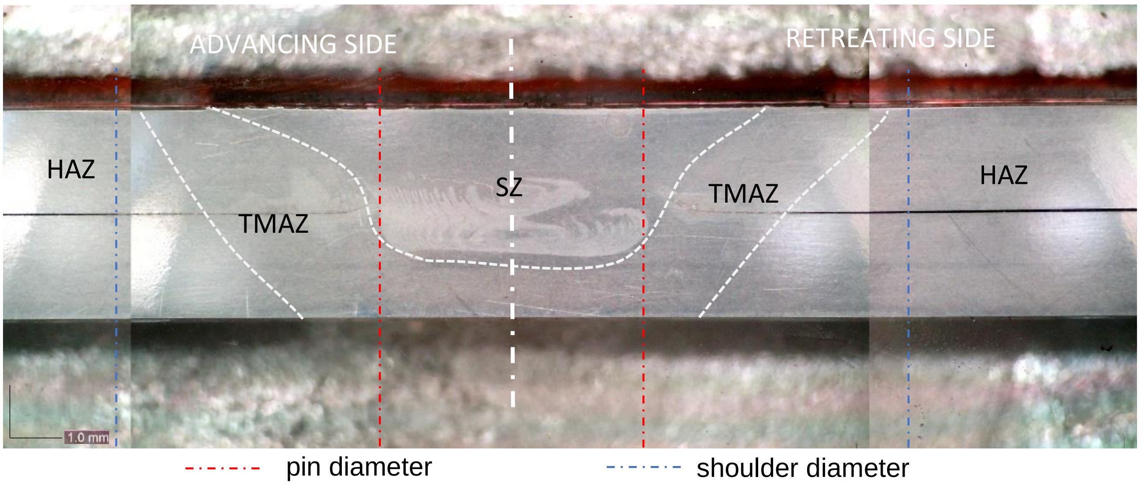

Figure 4.4: Representative macrostructure of AA6082-T6 FSW SLJ.

To better visualize the microstructure and detect possible defects, microscopic observation of the joint cross section was done. Figure 4.5 and Figure 4.6 highlight key points from the joints manufactured.

All manufactured FSW and Hybrid joints presented two main defects, previously mentioned in section 2.1.1, which will lead to stress concentration. Effective sheet thickness (EST) reduction of the top sheet is a direct consequence of both defects, impacting negatively in the joint's overall performance.

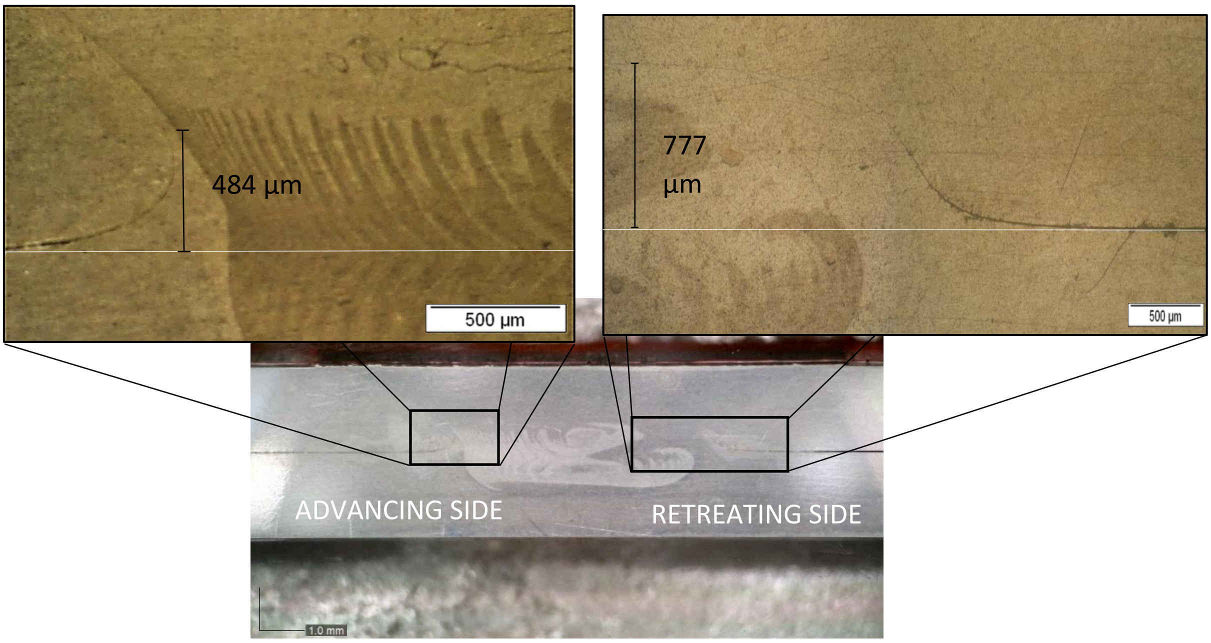

Figure 4.5: Representative overall view of the centre of the FSW joint and key points.

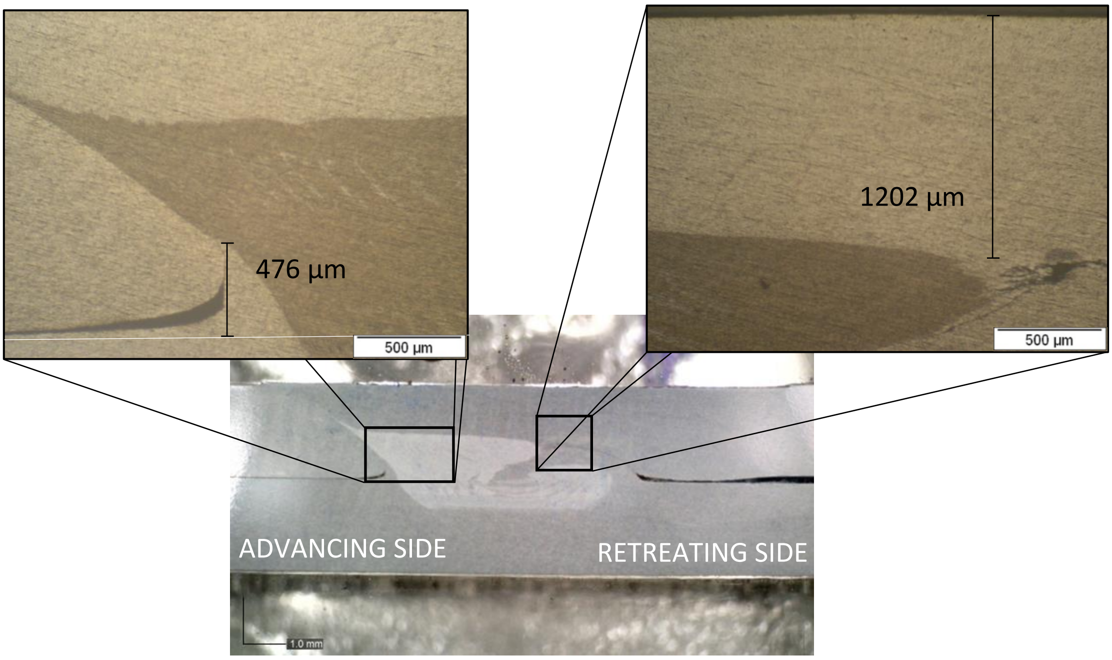

Figure 4.6: Representative overall view of the centre of the Hybrid joint and key points.

The first one is called hook defect and appears on the advancing side of the TMAZ. Similarly to what is found in the literature [9,30,98], the hook defect is facing upwards in the cross-section, indicating that there is an upward flow trend on this side of the weld. As the hook is progressing further into the top sheet, it starts gaining some curvature, also suggesting a sideward flow, which is corroborated by the grain orientation around the TMAZ/SZ area.

The second defect is called cold lap defect and appears on the RS. This defect starts in an upward direction in the TMAZ and, once it reaches near the TMAZ/SZ boundary, it starts a sideward movement, penetrating the SZ. Once again, it suggests an upward flow trend that is later countered by a downward flow with the purpose of filling the cavity at the bottom of the pin.

Although size of the hook and top plate thinning defects are similar for both FSW and Hybrid joints, the latter joints seem to have these defects filled with adhesive, which will reinforce these crack-like zones and result in a joint with an increased overall strength and ductility.

In Figure 4.6 it is also possible to observe that despite the use of calibrated metal stripes between the bottom and top sheets, adhesive layer thickness shows thinning towards the weld bead. Although this occurs mainly due to the axial force applied in the welding process, this feature may be a result of the lower reproducibility of the clamping conditions since the system used to manufacture these joints is mechanical. Nevertheless, in the Hybrid joints adhesive layer will still connect the free overlap area that exists between the top and bottom sheets of the FSW joints.

An unseen defect, called micro voids, is also mostly likely present in the Hybrid joints. This defect is characterized by the presence of adhesive residues that remained in the SZ upon the expulsion of the adhesive from this zone during the process.

4.4 Microhardness profile

After performing the microscopic analysis, microhardness was measured in the same specimens using a microhardness machine. Indentations were made along two lines located at the mid-thickness of the top and bottom sheets. Results for both FSW and Hybrid joints are presented in Figure 4.7.

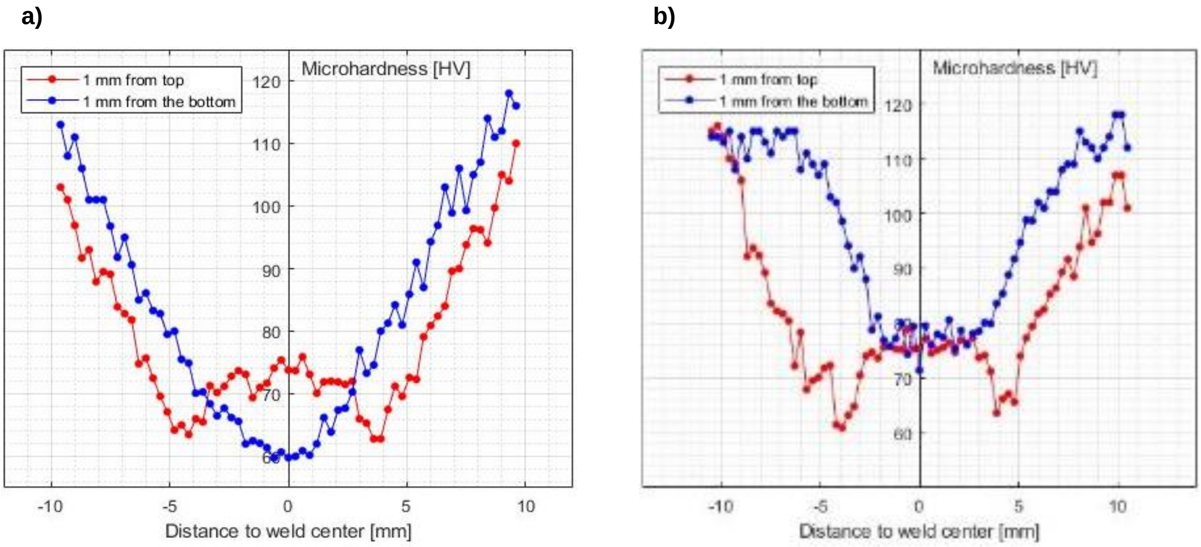

Figure 4.7: Microhardness curves of the FSW-1 and Hybrid-3 cross sections, respectively.

It is possible to notice that, in both joints, the top sheet follows the typical “W” shape hardness profile characteristic of heat treatable aluminium alloy welds. A significant hardness decrease is seen in the HAZ and TMAZ, with some values even reaching about 50% of the base material (typical values around 110 HV). This is consistent with the literature, indicating that the thermal cycles that the joints experience during the FSW lead to a softening and, consequently, a hardness decrease due to the dissolution and coarsening of the strengthening precipitates [99].

From previous works [9], temperature reached in the manufacturing of the these joints using the same parameters is reported to be higher than 200ºC, which leads to the loss of the T6 condition of the aluminium (temperatures higher than 200ºC) [100] and explains the softening experienced in these joints. This loss is characterized by the dissolution of the main strengthening precipitate β’’ and, when cooling, precipitation of the precipitate β’ with a lower strength, originating nucleation sites for the precipitates.

From Figure 4.7 it is also possible to conclude that the top sheet of the cross section has lower overall hardness values, which means that this region is the most affected during the welding process. This was already expected since the thermal cycle is more intense on the shoulder zone, leading to smaller recrystalized grains. This difference between the overall hardness values is more evident on the Hybrid joints since there is an adhesive layer in between the upper and bottom sheets with a much lower thermal conductivity value, preventing most of the dissipation of heat from the top to the bottom sheet. Near the centre line the inverse happens, with the hardness values being higher on the top sheet, which indicates a bigger influence of the stirring pin near its tip.

Although the lowest hardness values were noticed in the TMAZ on the AS, which also corresponds to the area of fracture zone, there is no significant difference in hardness between the AS and RS.

4.5 Single lap shear tests

To evaluate the mechanical performance of each type of joint manufacture, a series of lap shear test at 1 mm/min crosshead speed were done. For the FSW and the Hybrid joints, due to the appearance of the hook defect in the manufacturing process, the loading was always done on the advancing side of the top plate. The valid load-displacement curves obtained for both joints, as well as for adhesive bonded with 40 mm and 12.5 mm overlap joints are detailed in Figure 4.8.

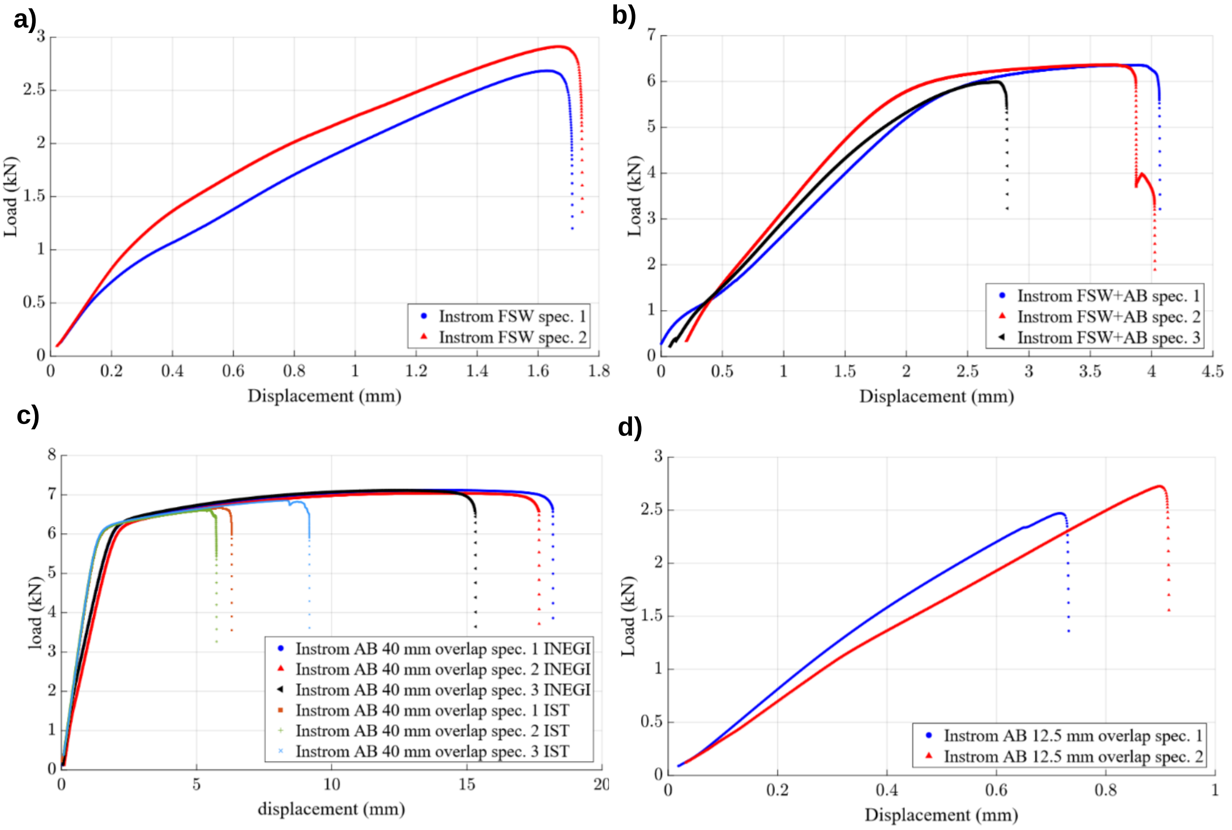

Figure 4.8: Load-displacement curves: a) FSW, b) Hyb and c) AB with 40 mm overlap and d) AB with 12.5 mm overlap specimens.

Table 4.2 shows the values of the average maximum load, maximum displacement and UTS for the FSW, Hybrid and adhesive bonded with 12.5 mm and 40 mm overlap joints, followed by Figure 4.9 which compares the representative load displacement curves for the different type of joints mentioned previously.

Table 4.2: Characteristics of the lap shear strength tests of the different joints.

Joint	Maximum load [N]	Maximum displacement [mm]	UTS [MPa]
FSW	2796.60 ± 112.50	1.73 ± 0.02	139.83 ± 5.62
FSW + AB	$6237.59 \pm {}^{123.22}_{243.45}$	$3.55 \pm {}^{0.43}_{0.82}$	$311.88 \pm {}^{6.16}_{12.17}$
AB 40 mm IST	$6712.09 \pm {}^{142.67}_{90.45}$	$7.07 \pm {}^{2.10}_{1.33}$	$335.60 \pm {}^{7.13}_{4.52}$
AB 40 mm INEGI	$7089.83 \pm {}^{28.17}_{52.35}$	$16.99 \pm {}^{1.15}_{1.73}$	$354.49 \pm {}^{1.41}_{2.62}$
AB 12.5 mm	2597.34 ± 125.90	0.86 ± 0.10	129.87 ± 6.30

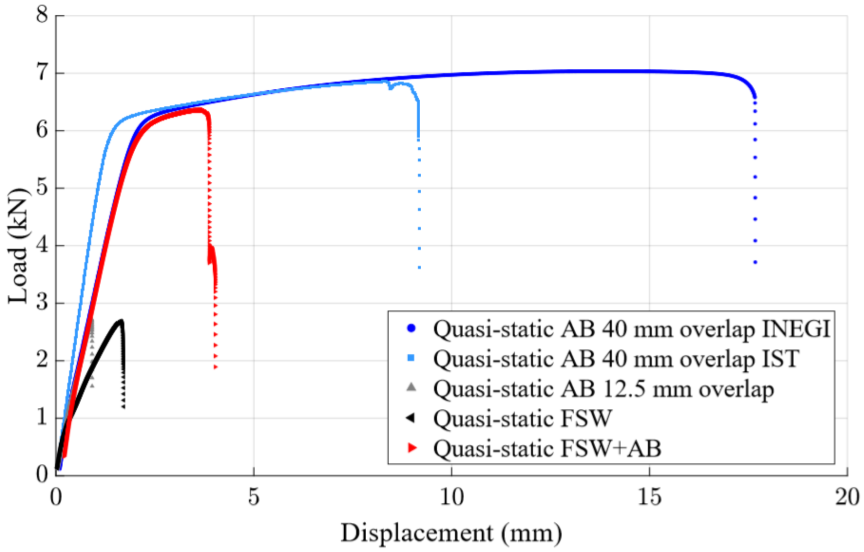

Figure 4.9: Representative load displacement curves of FSW, Hybrid and adhesive bonded with 12.5 mm and 40 mm overlap joints.

FSW joints were the ones with the lowest performance for the same overlap length of 40 mm, as expected. This is a direct consequence of the hook defect observed in the welds produced. In all the joint tests, this defect led to a fracture initiated on the advancing side, with the hook defect propagating until it reached the top aluminium sheet. A fracture's example is presented in Figure 4.10.

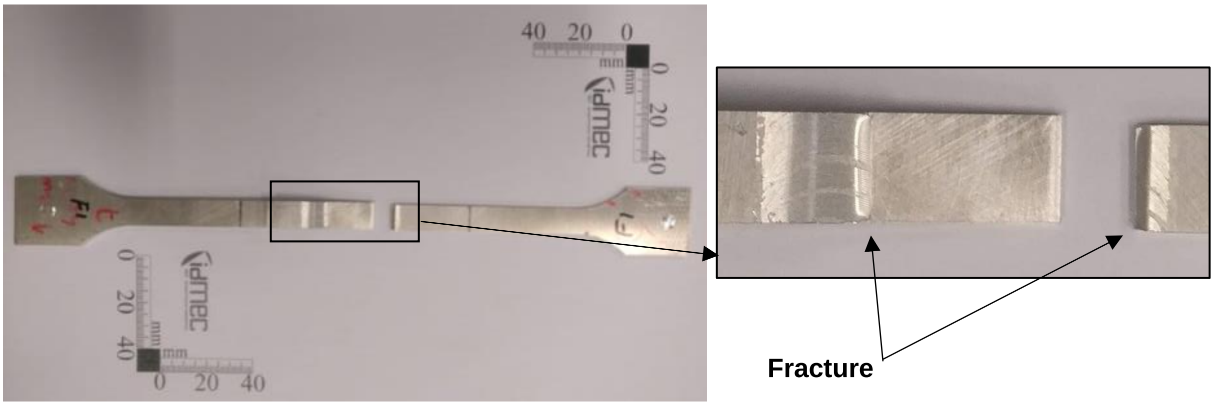

Figure 4.10: FSW-1 specimen fracture zone.

Adhesive bonded joints with a 40 mm overlap manufactured at INEGI registered the best overall performance. Highest strength and ductility are achieved in this type of joints and fracture occurs always in the adherent, as seen in Figure 4.11, which indicates that the joint is stronger than the aluminium base material. When the overlap is reduced to 12.5 mm, strength and ductility of the joints are greatly reduced, with its values dropping 39% and 94%, respectively. However, in this case, failure occurs in the adhesive/aluminium interface, which indicates not only that surface treatment was not as efficient as it should have been, as it can be seen in Figure 4.12, but also that with a reduction of the overlap adhesive cannot sustain as much damage as before.

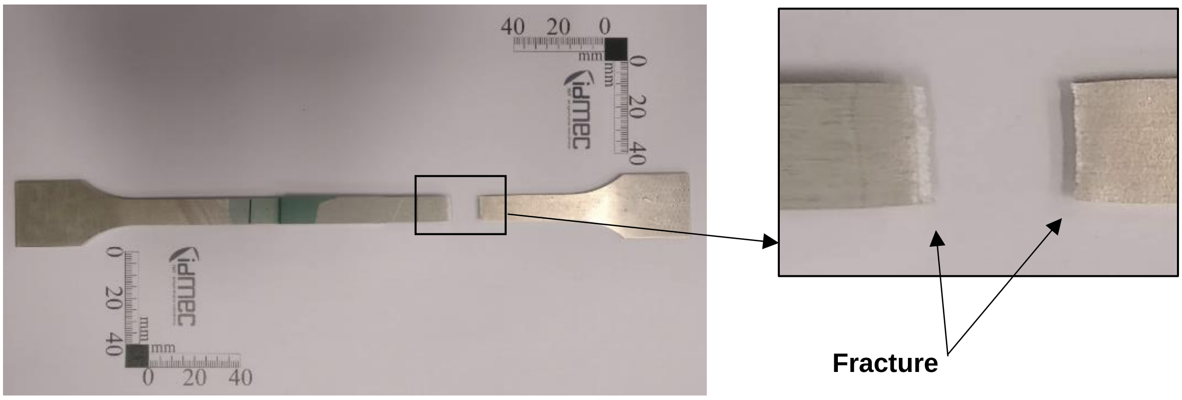

Figure 4.11: AB-2 specimen (INEGI) fracture zone.

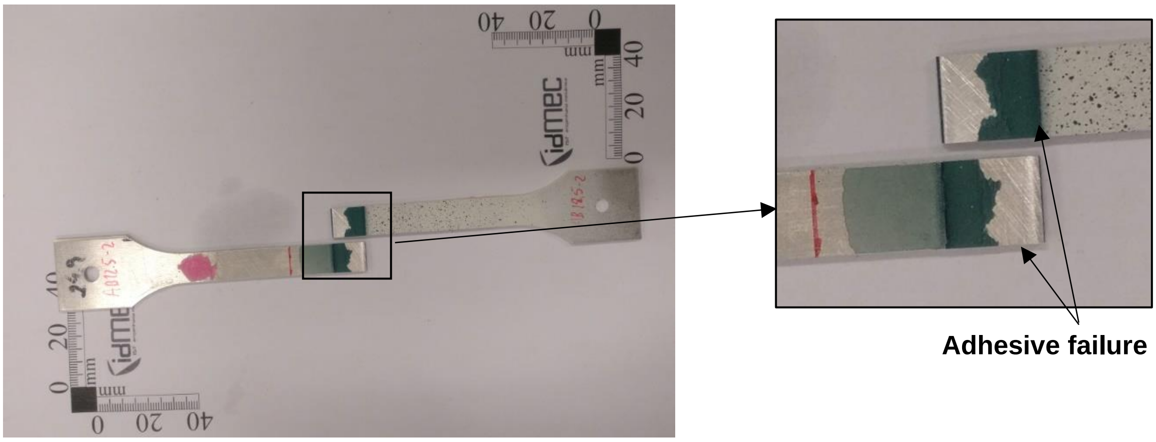

Figure 4.12: AB12.5-2 specimen failure zone.

Adhesive bonded joints with a 40 mm overlap manufactured at IST showed lower strength and ductility in comparison to the ones manufactured at INEGI. Reduction in strength was around 5% and can be explained due to the different manufacturing conditions of this batch. The vacuum pump used did not have enough capacity to remove all the air inside de bag around the mould, which would not allow to reach the desired vacuum environment, leading to a softer adhesive layer.

Also, by looking at the failure zone, this time around, it happened on the adhesive/aluminium interface, with most of it being adhesive, suggesting that surface treatment did not achieve its full capacity and, consequently, carrying capacity of the adhesive is greatly reduced. This was the main contribution for the reduction of almost 60% in ductility.

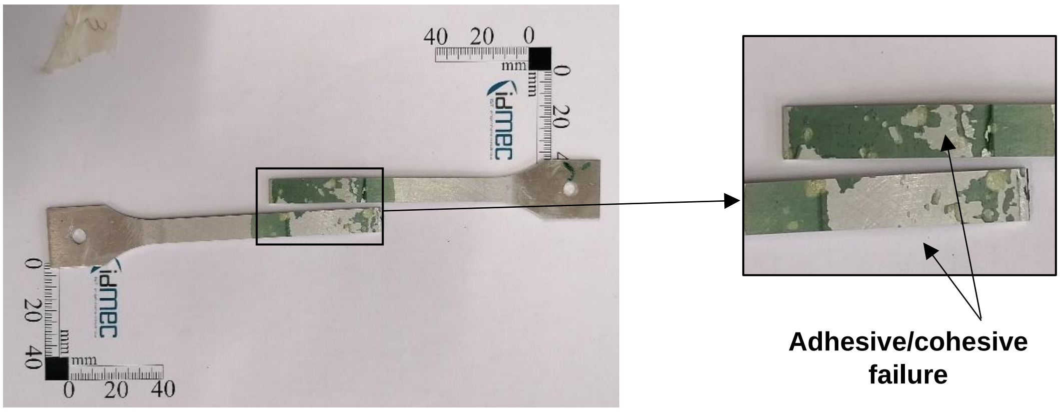

Figure 4.13: AB-3 specimen (IST) failure zone.

Hybrid joints, being a combination of two processes, presented an intermediate performance. When compared with FSW only overlap joints, the addition of the adhesive represented a great improvement both in strength and ductility, reaching 118% and 133%, respectively, when best performing specimens for both techniques are compared.

When compared to the adhesive bonded joint with 40 mm overlap, a slightly decrease in performance was noticed, reaching a reduction of about 11% and 77% in strength and ductility, respectively. In this case, contrary to what happened to the adhesive bonded with 40 mm overlap joints, fracture of the adhesive occurs.

Although most of the joints shown a similar failure mechanism, with a simultaneous failure of the adhesive layer, that loses its carrying capacity, and the aluminium around the HAZ and TMAZ in the advancing side, some specimens were still able to carry a lower load through the joint before the final fracture of the aluminium, after the adhesive part failed. Adhesive carries most of the loading of the joint and the existence of stress concentration at the edges of the overlap leads to a faster breakage of the adhesive. To some extent this can even be seen as a damage tolerance point when designing these joints.

Failure of the adhesive was adhesive/cohesive, which indicates that the adhesive was not performing at its full potential (Figure 4.14).

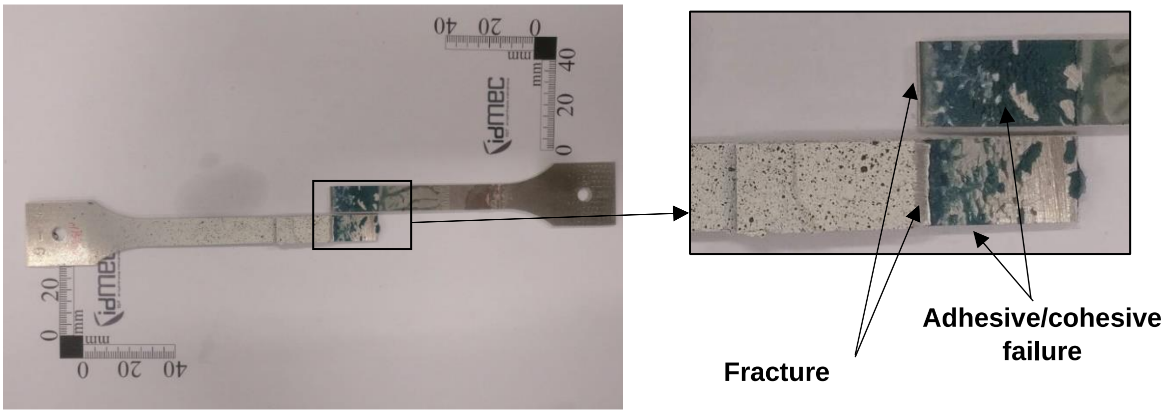

Figure 4.14: Hyb-3 specimen fracture zone.

Due to laboratory availability, only AB joints with a 40 mm overlap manufactured at IST were studied at 100 mm/min. Load-displacement curves obtained for these joints are represented in Figure 4.15.

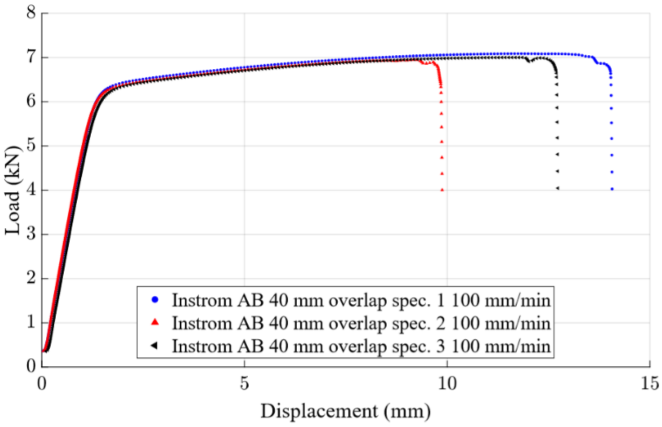

Figure 4.15: Load-displacement curves of the AB with 40 mm overlap specimens at 100 mm/min.

Figure 4.16 compares the representative load displacement curves for the AB joints manufactured at IST. AB joints showed an increase of around 15 MPa in the UTS, with an increase in strain rate from $10^{-4}\ s^{-1}$ to $10^{-2}\ s^{-1}$, averaging a maximum load of 7013.69 $\pm\,^{74.31}_{63.01}$. Ductility also rose 73%, with a mean maximum displacement of 12.22 $\pm\,^{1.84}_{2.35}$. Despite all these, from the joint fracture is possible to see that surface treatment has not reached its full capacity, which led to an inconsistent adhesive/substrate bond (Figure 4.17), similarly to what occurred for 1 mm/min displacement rate.

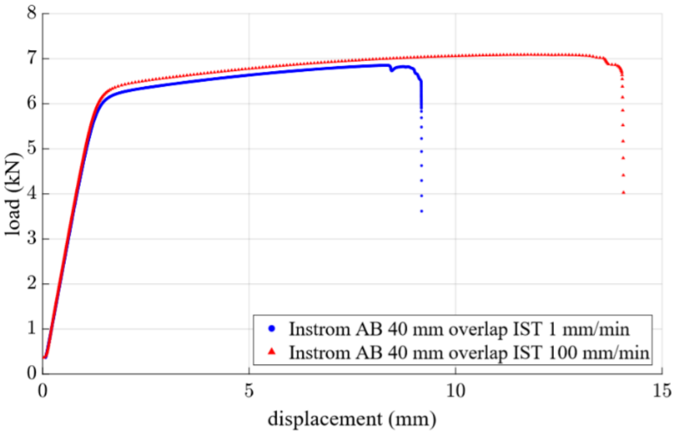

Figure 4.16: Representative load displacement curves of the adhesive bonded specimens at different strain rates.

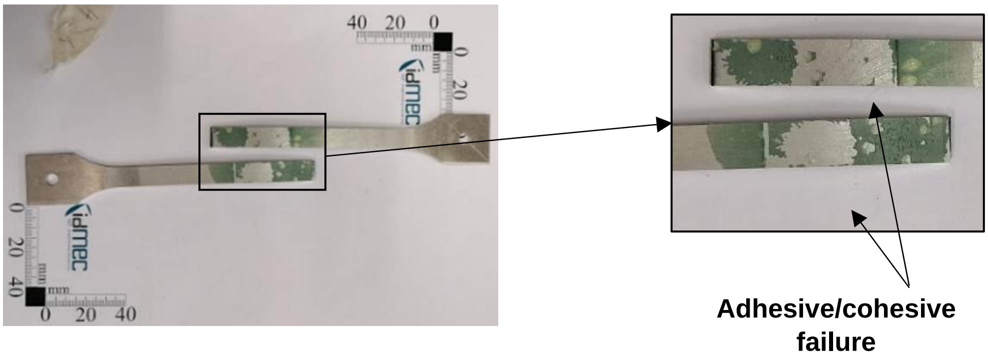

Figure 4.17: AB-1 specimen failure zone, at 100 mm/min.

Joint efficiency was obtained by calculating the ratio between the remote stress of the joint (calculated using the ultimate load and the remote area, $10 \times 2 = 20\ mm^2$) and the ultimate tensile strength of the base material, Figure 4.18. Application of the adhesive layer on the Hybrid joint attenuates some of the defects characteristic from the FSW process, leading to a substantial improvement comparatively to the FSW joints of around 49 %, that was already expected to achieve a lower performance since hook defect and mechanical property changes due to heat input were too high.

All the 40 mm overlap adhesive joints had a performance superior to the Hybrid ones, with the best manufacture AB joints even reaching a 102.4% joint efficiency, which represents a small improvement comparatively to the solely use of an aluminium specimen, corroborated by the fracture zone of these specimens (adherent). Also, it was noticed an increase in efficiency (≈ 3%) when increasing the strain rate of the adhesive joint, which indicates a strain hardening on the adhesive part. As for the AB-12.5, the overlap length is not enough for the adhesive to carry stresses, resulting in a low performance, as expected.

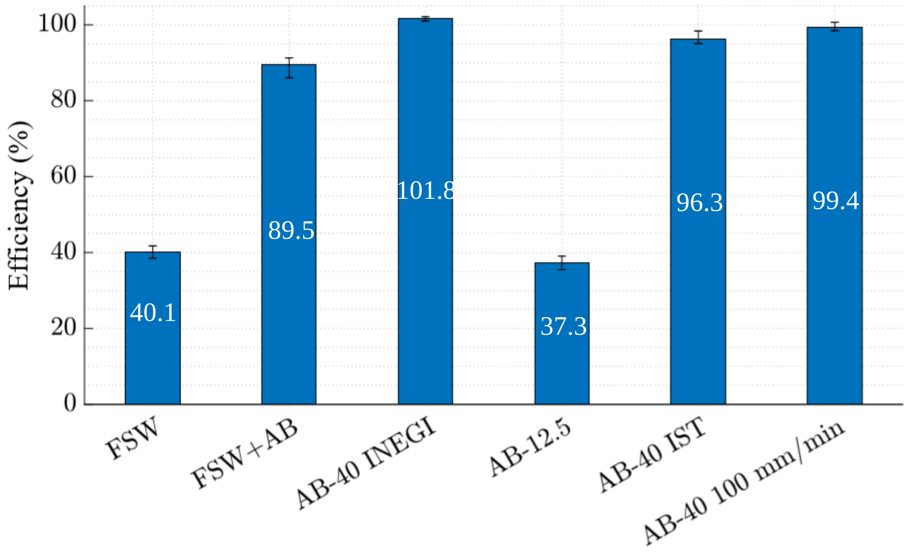

Figure 4.18: Efficiency of each joint type manufactured.

4.6 Impact tests

In order to assess the behaviour of the joints under high strain-rate, impact loadings, specimens were tested under these conditions. Although many specimens have been tested, only a few were considered valid. Many difficulties were encountered along the away that would not allow reaching valid results: acquisition data failure, capacitors failing to fire on request, insufficient impact energy (resulting in non-fractured specimens), and occurrence of multiple impacts until fracture of the specimens (adulterating both displacement and load measurements).

In Table 4.3, test conditions for each valid specimen (impact velocity and impactor mass) are detailed, as well as the maximum load, maximum displacement, UTS and type of failure.

Table 4.3: Characteristics of the impact tests of the different valid specimens.

Specimen	Impact velocity [m/s]	Impactor mass [Kg]	Specimen failure type	Maximum load [N]	Maximum displacement [mm]	UTS [MPa]
FSW-1	6	7	Through hook defect	3977.58	2.18	198.88
FSW-2	4	7	Through hook defect	3722.30	1.99	186.12
FSW-3	7	7	Through hook defect	3480.68	2.16	174.03
Hybrid-3	12	7	Adherent	6723.42	24.48	336.17
Hybrid-6	9	7	Adherent	6794.79	27.70	339.74
Hybrid-8	9	10	Premature failure	6187.28	6.38	309.36
AB12.5-1	2	7	Adhesive/ cohesive	3264.45	1.56	163.22
AB12.5-2	3	7	Adhesive/ cohesive	2836.61	1.73	141.83

Valid tests of adhesive bonded joints with 40 mm overlap could not be obtained, mostly because the impact energy was not enough to fail the joint on a single impact. This would lead to a progressive failure of the joint instead of a first impact failure, which was the objective of the present study. One way to surpass this could be accomplished by adding more mass in the striker bar so that impact's energy could be higher.

Load-displacement curves for the AB joints with 12.5 mm overlap are represented in Figure 4.19 and, in Figure 4.20, a comparation with quasi-static tests is shown.

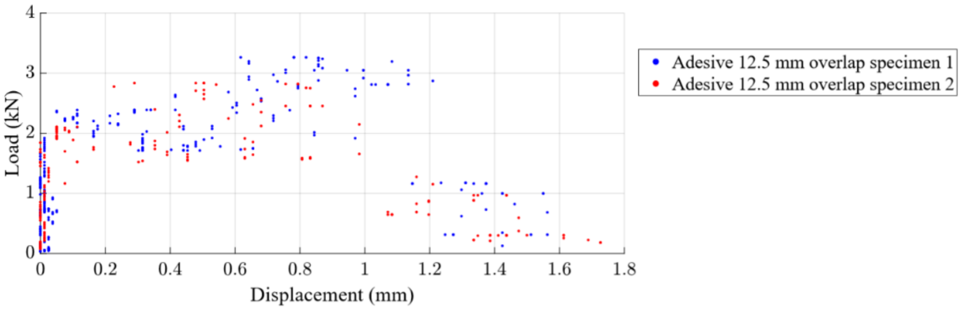

Figure 4.19: Load-displacement curves of the AB 12.5 mm overlap specimens.

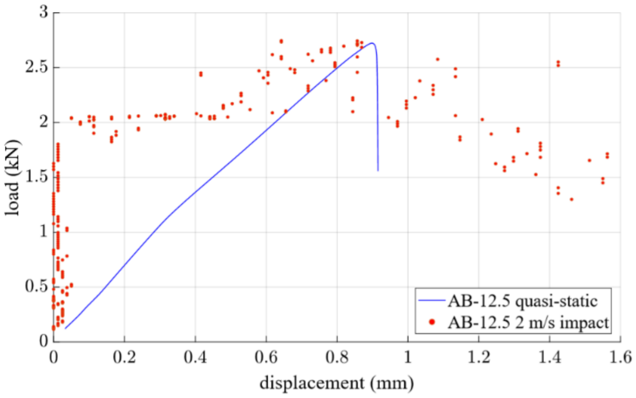

Figure 4.20: Representative load displacement curves for AB-12.5 specimens at different strain rates.

AB joints with 12.5 mm overlap continue to be the lowest performing joints. Although joint strength is almost the same for both tests, ductility increased on average 100%, which shows the energy absorption potential of the adhesive under impact. However, an adhesive type failure is still the reason for the joint's failure, showing again that surface treatment can be improved (Figure 4.21).

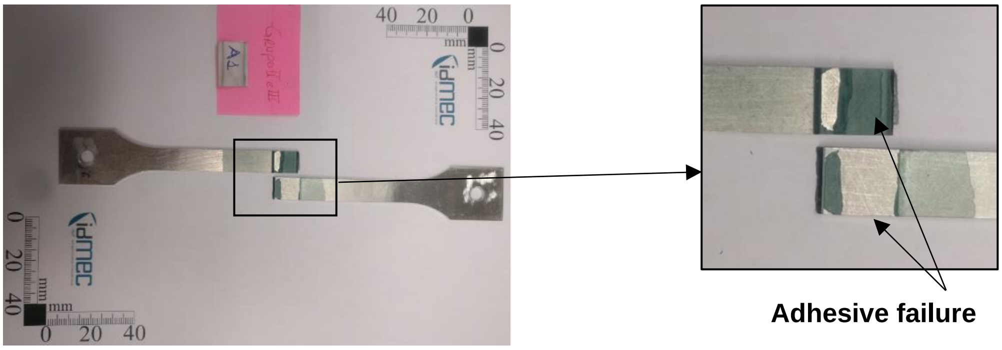

Figure 4.21: AB12.5-1 specimen failure zone.

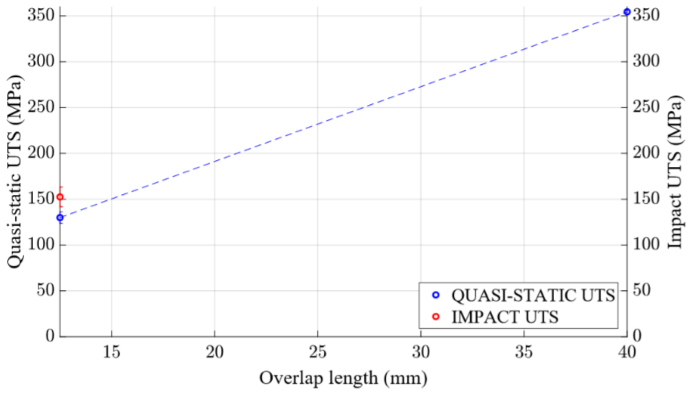

Figure 4.22: Overlap length influence on the adhesive joint behaviour, using a linear interpolation.

In Figure 4.22 it is possible to see influence of the overlap length on the adhesive joints. For the quasi-static tests, the increase in the overlap from 12.5 mm to 40 mm corresponds to an increase in strenght of 170%. Through a linear interpolation, the 40 mm overlap seems to be almost the minimum overlap possible to achieve a joint's strenght similar to the base material. For the impact tests, although a comparision between overlap lengths is not possible to be done, due to the reasons previously explained, it is possible to see that, despite the increase in strength from quasi-static to impact tests of the AB joint for a 12.5 mm overlap, an increase in scatter from 6.3 MPa to 10.7 MPa also occurs.

Load-displacement curves from the FSW and Hyb joints are shown in Figure 4.23. This data, obtain with the acquisition system, has no filter in it.

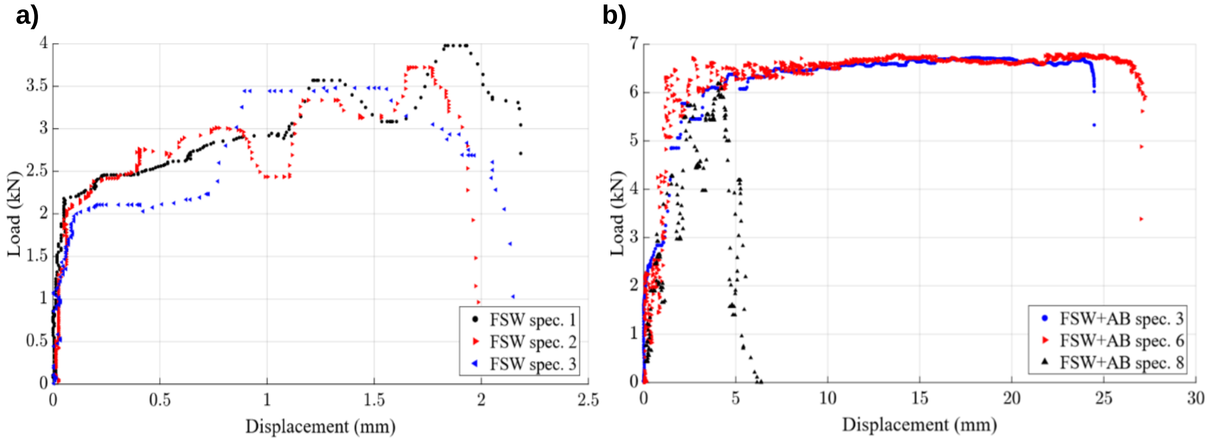

Figure 4.23: Load-displacement curves: a) FSW and b) Hybrid.

All FSW joint fractures occurred through the hook defect. This was already expected, as explained in the previous section. Figure 4.24 shows the effect that this defect has the immediate moment before starting to propagate.

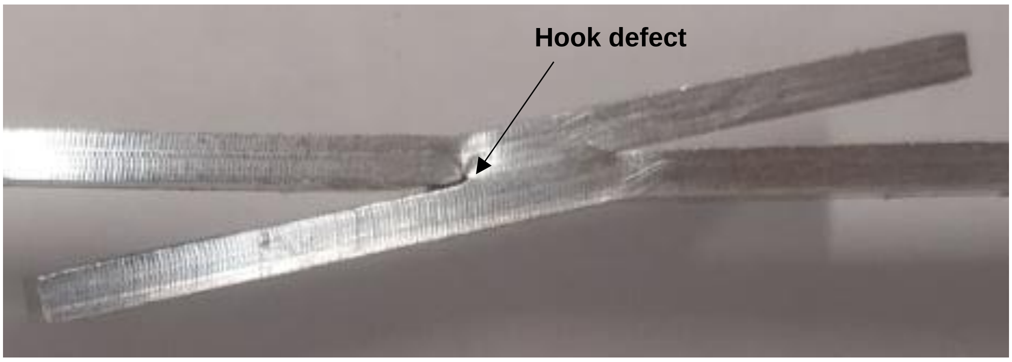

Figure 4.24: FSW joint failure mechanism.

For the Hybrid joints, there is a clear difference between the best performing and the worst performing joints, with the former fracturing in the adherent and the latter fracturing through the adhesive layer. This can most likely be explained either by differences in the surface treatment or even by heat input difference when welding. Surface treatment is made manually and so, consistency of the process can suffer some variations even if it is done by the same person, which can lead to different interfacial strengths between joints. As for the second one, refrigeration system of the FSW machine was off, which may have caused a greater variation in the heat input not only on the same weld but also for the next welds to be made, resulting in a change in the material properties of the joint. Figure 4.25 and Figure 4.26 show the two type of failures, and it is also possible to notice the significant increase in ductility that the joint has when it fractures in the adherent.

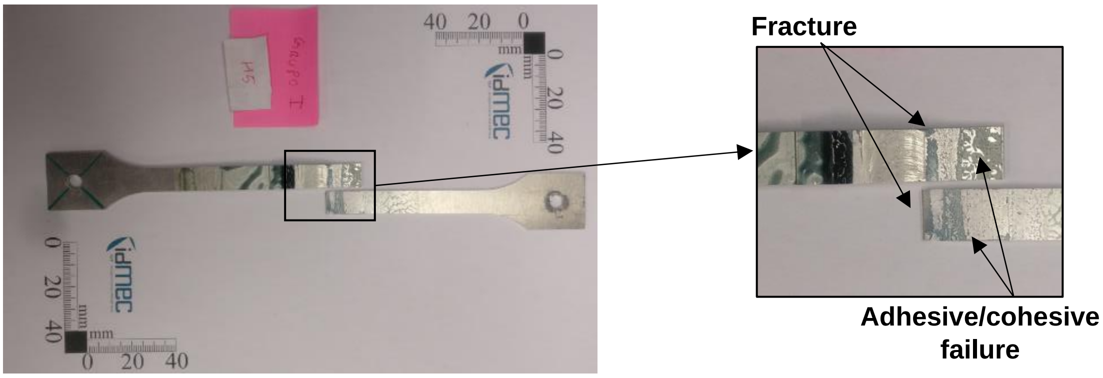

Figure 4.25: Hyb-5 specimen fracture zone.

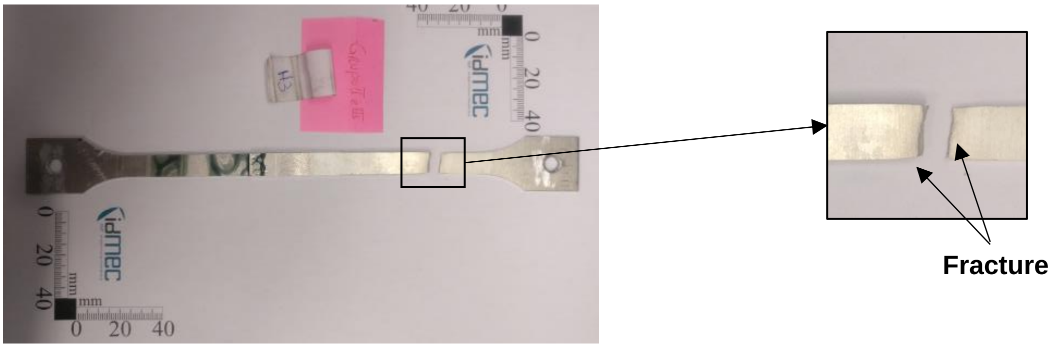

Figure 4.26: Hyb-3 specimen fracture zone

In Figure 4.27, a comparison between quasi-static and impact tests for FSW and Hybrid joints is shown. A moving average filter was carefully chosen to smooth out the impact curves by removing some of the noise present without significantly effecting the output results obtained from the original signal.

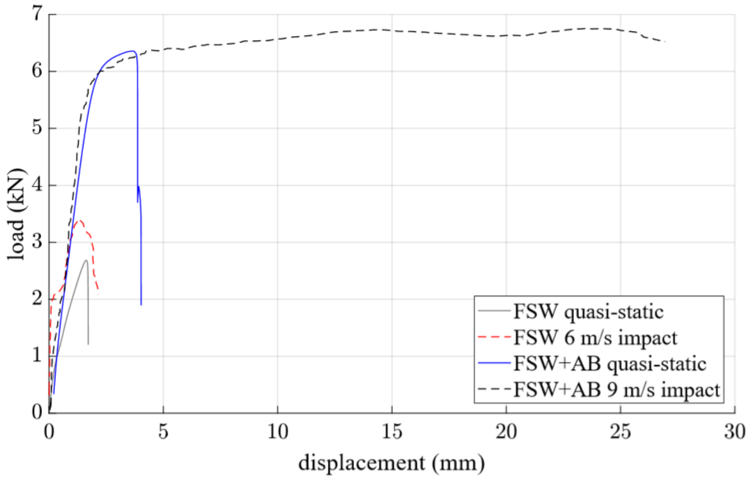

Figure 4.27: Representative load displacement curves for FSW and Hyb specimen at different displacement rates.

In the FSW, joint strength values reached a 32% increase. In [97] Chen *et al* found that AA6082-T6 shows a clear rate sensitivity in the range of $0.001{\sim}1\ s^{-1}$, being the later value the order of magnitude of these experiments. This is coherent with the results presented and may also indicate the strain rate dependency of the other zones, with different mechanical properties, in the centre of the joint. Ductility also shows an average increase of 22%.

For the Hybrid joints, although only a slight increase in joint strength is obtained (≈ 9%), a substantial increase in ductility, around 680%, is noticed. This can be explained by the high ductility of the adhesive in use, which for withstanding impact loadings is of extremely importance since it is related directly with the capability of absorbing the energy of the impact. Difference in energy absorption, estimated by calculating the area beneath the load-displacement curve, can be seen in Figure 4.28.

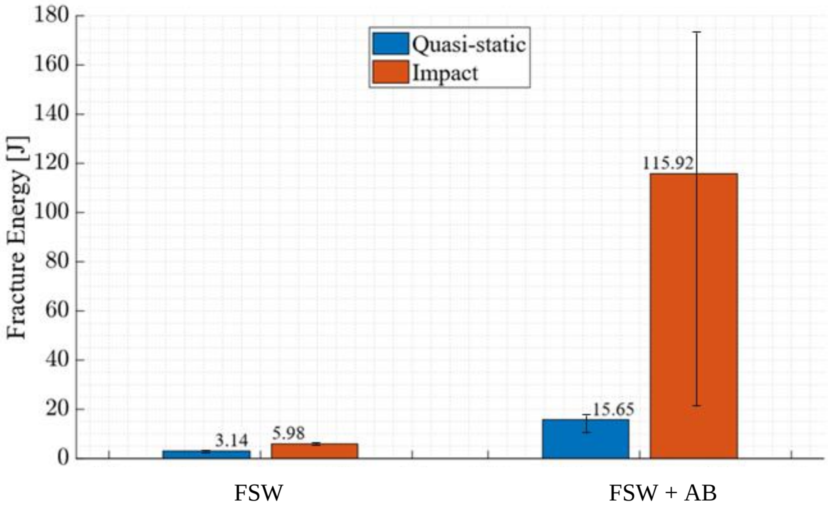

Figure 4.28: Fracture energy comparison between quasi-static and impact events.

At a quasi-static rate, Hybrid joints increase the energy absorbed by 400% comparatively to the FSW one's. Increasing the velocity of the test results in an improvement of 388% of the energy absorbed by the Hybrid joint in comparison to the results from the quasi-static. Although scatter in FSW joints is small (≈6%) for both tests, scatter in the Hybrid joints reach 60% and 80% for quasi-static and impact tests, respectively. This might be explained by the inconsistent surface treatment, since in the joints with lower absorbed energy the fracture occurs in the adhesive, whereas in the ones with a higher energy absorbed, with values reaching 174 J, fracture occurs in the adherent. Also, although the change in the velocity of the impact tests, from 6 to 9-12 m/s, seems relatively small, it might have some impact on these results since changes in the strain rate of the adhesive might be significative for the adhesive to change its behaviour. Nevertheless, these two fracture types are particular important since it can represent a turning point in the joint's behaviour, where the fracture condition is no longer the adhesive but instead the aluminium adherent.

The amount of energy absorbed can be backed up by the velocity variation during the impact, which is shown in Figure 4.29. It is possible to see that velocity is almost constant in the FSW experiments, whereas in the Hybrid one's velocity decreases up until fracture.

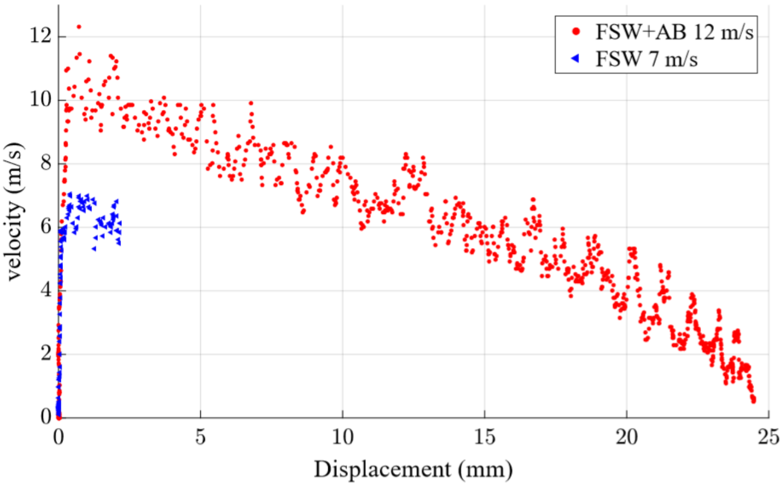

Figure 4.29: Representative velocity displacement curves for FSW and Hyb specimen.

Chapter 5

Numerical analysis

Considering the complexity of the different loads present on these types of welds, a finite element model (FEM) was built. These types of model are an important aid to predict a joint's performance during its service.

This chapter will start by presenting the material characterization and corresponding techniques used, followed by a short explanation of the path used to implement the numerical models developed in this thesis. Finally, a comparison between the experimental and the numerical results is provided.

5.1 Aluminium characterization and modelling behaviour

As described in section 2.1.1, in the FSW process 3 new zones (SZ, TMAZ and HAZ), other than the aluminium base material, appear and each has its own mechanical properties that need to be considered in the FE model. Braga [9] performed tensile tests and acquired the strain values using Digital Image Correlation (DIC).

In the Figure 5.1 it is possible to observe that each region of the weld has its own hardening behaviour. In order to extrapolate these results, it was required to used isotropic hardening laws, namely the Swift and Voce laws:

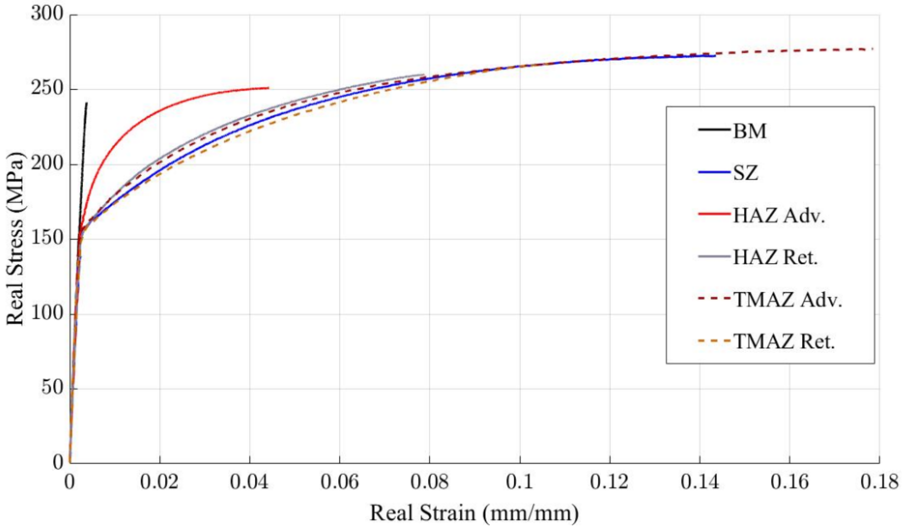

Figure 5.1: Real stress vs real strain curves for the 6 different zones of the material [9].

- Swift law $$\sigma_s = K\left(\varepsilon_0 + \bar{\varepsilon}_p\right)^n \tag{5.1}$$

- Voce law $$\sigma_s = \sigma_0 + Q\left(1 - e^{\left(-\beta\bar{\varepsilon}_p\right)}\right) \tag{5.2}$$

Where $\bar{\varepsilon}_p$ is the equivalent plastic strain, ε_0 is the yield strain, K and n are the Swift law material constants and σ_0 is the yield stress, Q and β are the Voce law material constants.

The extrapolation results are presented in Table 5.1:

Table 5.1: Hardening law material constants for the different material zones, adapted from [9].

	BM	**HAZ Adv.**	**HAZ Ret.**	**TMAZ Adv.**	**TMAZ Ret.**	**SZ**
$\boldsymbol{\varepsilon_0}$	**0.006**	**0.0047**	**0.0043**	**0.0044**	**0.0043**	**0.0043**
$\boldsymbol{\sigma_0}$	**278.8**	**183.4**	**161**	**162.5**	**159.7**	**160.4**
$\boldsymbol{K}$	**438.4**	**394.7**	**412.7**	**387.8**	**408.1**	**385**
$\boldsymbol{n}$	**0.0934**	**0.1341**	**0.1779**	**0.1561**	**0.1859**	**0.1654**
$\boldsymbol{R^2_{Swift}}$	**0.982**	**0.967**	**0.999**	**0.984**	**0.996**	**0.979**
$\boldsymbol{Q}$	**91.31**	**67.24**	**408.2**	**113.3**	**123**	**116.2**
$\boldsymbol{\beta}$	**19.06**	**109**	**32.2**	**26.33**	**20.44**	**24.08**
$\boldsymbol{R^2_{Voce}}$	**0.993**	**0.997**	**0.999**	**0.998**	**0.999**	**0.999**

It is possible to observe that the extrapolation used is coherent with the original real stress vs plastic strain data due to the high values of the determination coefficients (R^2). For aluminium alloys it is preferred the use of the Voce law because it accounts for a hardening saturation level, commonly present in these type of alloys, although its fitting sometimes might lead to an underestimation of the strain [73].

In order to predict more accurately the plastic behaviour and subsequent failure of the aluminium adherent, a ductile damage criterion is also necessary. The model chosen, the Gurson-Tvergaard-Needleman (GTN) model, originally proposed by Gurson [101] and modified later by Tvergaard and Needleman [102], takes into account not only void nucleation and growth of microscopic voids but also the coalescence resultant from the necking of the ligament between two neighbouring voids, in the ductile metal. The failure on the metal will occur once the damage variable (porosity) deteriorates sufficiently the stiffness and the strength of the metal.

The GTN model describes the yield function as the following [102]:

$$\Phi = \left(\frac{\bar{\sigma}}{\sigma_0}\right) + 2q_1 f^* \cosh\left(-q_2 \frac{\sigma_h}{\sigma_0}\right) - \left(1 + q_3 {f^*}^2\right) \tag{5.3}$$

Where $\bar{\sigma}$ is the Von Mises equivalent stress, σ_0 the original yield stress and σ_h the hydrostatic pressure. For material parameters, accordingly to [102], $q_1 = 1$, $q_2 = 1$ and $q_3 = q_1^2 = 2.25$. These values are applicable to most metal materials and have shown good agreement with aluminium in [9].

Coalescence between two neighbouring voids occurs either by spreading of slip planes between cavities or by necking of the ligament when their size reaches the order of magnitude of their spacing [102]. Having in mind that f is the void volume fraction, and that it can take the values between 0 and 1, being $f = 0$ a fully dense material and $f = 1$ a completely voided material, a function f^* is created to describe the evolution of the void volume fraction:

$$f^* = \begin{cases} f & f \leqq f_c \\ f_c + \dfrac{\bar{f}_F - f_c}{f_F - f_c}(f - f_c) & f_c < f > f_F \\ \bar{f}_F & f \geqq f_F \end{cases} \tag{5.4}$$

Where f_c is the critical void volume fraction and f_F is the value of void volume fraction at final fracture, where material loses the capacity to carry stress along it. Values of f_c and f_F are 0.012 and 0.15, respectively and according to [103]. $\bar{f}_F$ follows the following relation:

$$\bar{f}_F = \frac{q_1 + \sqrt{q_1^2 + q_3}}{q_3} \tag{5.5}$$

To finally complete the model, the gradual change in the void volume fraction should account not only the growth of existing voids but also the nucleation of the newer ones:

$$\dot{f} = \dot{f}_{growth} + \dot{f}_{nucleation} \tag{5.6}$$

Where:

$$\dot{f}_{growth} = (1 - f)\, \dot{\varepsilon}^{\rho l} \tag{5.7}$$

And

$$\dot{f}_{nucleation} = \frac{f_N}{S_N\sqrt{2\pi}} \exp\left\{ -0.5 \left[\frac{\bar{\varepsilon}_m^{\rho l} - \varepsilon_N}{S_N} \right]^2 \right\} \dot{\varepsilon}_m^{pl} \tag{5.8}$$

With $\dot{\varepsilon}^{\rho l}$ as the plastic strain rate, $\dot{\varepsilon}_m^{pl}$ the plastic strain rate for the fully dense matrix, f_N the volume fraction of the nucleated voids, ε_N the mean nucleation strain and S_N the standard deviation. The values of ε_N, S_N and f_N are 0.15, 0.10 and 0.01, respectively and according to [103].

5.1.1 Isotropic hardening laws for the adhesive joints

Since tensile properties were assessed experimentally for the base material in the present work, extrapolation of these results was performed using both isotropic hardening laws. Results are shown in Table 5.2

Table 5.2: Hardening law material constants for base material.

	$\boldsymbol{\varepsilon_0}$	$\boldsymbol{\sigma_0}$	$\boldsymbol{K}$	$\boldsymbol{n}$	$\boldsymbol{R^2_{Swift}}$	$\boldsymbol{Q}$	$\boldsymbol{\beta}$	$\boldsymbol{R^2_{Voce}}$
BM	0.006	311.4	484.3	0.0982	0.982	111.2	12.35	0.999

A comparison between these laws and the laws from [9], with the same GTN parameters mentioned previously included as well, is presented in Figure 5.2.

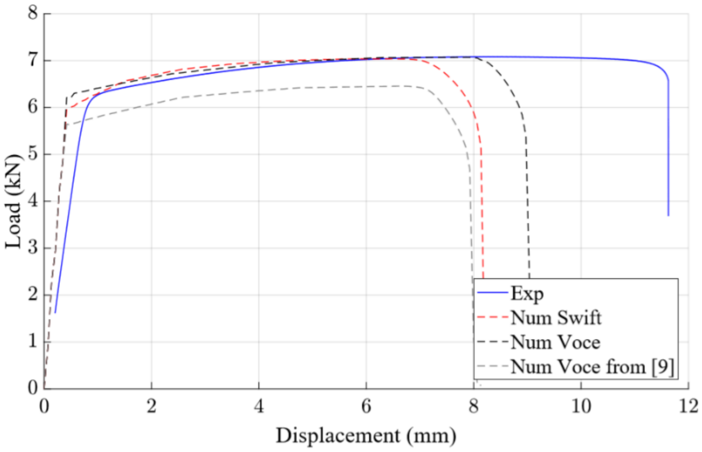

Figure 5.2: Experimental and numerical load-displacement curves for the base material.

From Figure 5.2 it is possible to see that the isotropic hardening law that better models the behaviour of the base material is the Voce law from the present study. Although a good prediction of strength is obtained, further developments should be done in the future to the GTN model to increase accuracy of the model in terms of ductility, since the values used were based from literature [103].

Having this into account, the adhesive models will be modelled using this Voce law, whereas the FSW and the Hybrid joints will use the Voce law from [9] since in the present study no experimental measurements were taken for the HAZ, TMAZ and SZ zones.

5.2 Adhesive modelling behaviour

To model the adhesive layer on both adhesive bonding and Hybrid joints, it was opted to use a technique called Cohesive Zone Modelling (CZM). CZM utilizes the relationship between peel stress, σ, and shear stress, τ, to simulate the elastic behaviour and subsequent softening due to the degradation of the material properties.

This method can be used with different cohesive law shapes and the one chosen for these simulations was the trapezoidal traction separation law, not only because of the adhesive relatively high ductility [104] but also because of the more accurate results proven from previous experiments [9,105]. Figure 5.3 shows the 3 loading stages of the CZM (elastic damage, damage initiation and damage propagation) represented by linear relations, where t_s^0 and δ_s^0 are the shear cohesive strength and the correspondent displacement, respectively, δ_s^s is the shear stress softening onset displacement and δ_s^f is the shear failure displacement. The same is applied for normal loading, substituting in the nomenclature the subscripted s for a n. Note that the total area below the trapezoid corresponds to the fracture toughness in tension (G_I or G_n^c) or in shear (G_{II} or G_s^c).

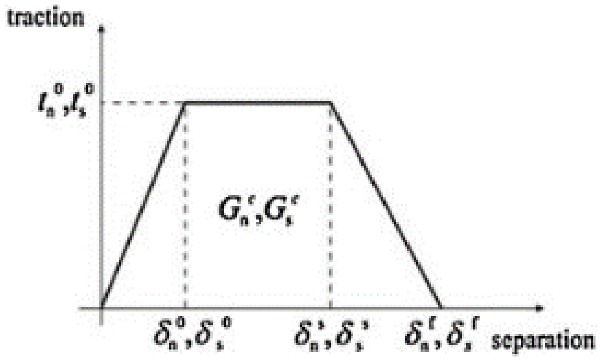

Figure 5.3: CZM with trapezoidal shape [90].

Having this into account, elastic damage can be defined by the following constitutive matrix which relates current stress and strain:

$$t = \begin{Bmatrix} t_n \\ t_s \end{Bmatrix} = \begin{bmatrix} K_{nn} & K_{ns} \\ K_{ns} & K_{ss} \end{bmatrix} \cdot \begin{Bmatrix} \varepsilon_n \\ \varepsilon_s \end{Bmatrix} \tag{5.9}$$

Where the subscripts n and s stand for normal and shear, respectively, and $\boldsymbol{K}$ is the stiffness matrix, with $K_{nn} = E$, $K_{ss} = G$ e $K_{ns} = 0$.

For the damage initiation criteria, it was used the quadratic nominal stress criterion:

$$\left\{ \frac{\langle t_n \rangle}{t_n^0} \right\}^2 + \left\{ \frac{t_s}{t_s^0} \right\}^2 = 1 \tag{5.10}$$

Macaulay brackets ⟨ ⟩ are used on the first term because normal (pure compression) stresses do not cause damage initiation. After the fulfilment of equation 5.11, softening occurs due to the beginning of the degradation of the material properties, following the damage evolution law below:

$$t_n = \begin{cases} (1 - D)T_n & T_n > 0 \\ T_n & T_n < 0 \end{cases} \tag{5.11}$$

$$t_s = (1 - D)T_s \tag{5.12}$$

Where T_n and T_s are the current undamaged normal and shear traction, respectively, and D is the scalar stiffness degradation, floating between 0 and 1, which corresponds to no damage and full damage, respectively. Once again, compressive stress won't cause damage propagation. Value of D can be obtain through the following equation [105]:

$$\begin{cases} d_{n,s} = 1 - \dfrac{\delta_{n,s}^0}{\delta_{n,s}} & if \quad \delta_{n,s}^0 < \delta < \delta_{n,s}^s \\ d_{n,s} = 1 - \dfrac{m\delta_{n,s} + b}{K_{nn,ss}\delta_{n,s}} & if \quad \delta_{n,s}^s < \delta < \delta_{n,s}^f \end{cases} \tag{5.13}$$

Where first part is for the constant stress region (constant portion of the CZM law) and second part is for the softening region (decaying portion of the CZM law), in which m and b values correspond to the linear equation of the decaying straight line.

Lastly, a linear power law is used to predict the complete separation:

$$\frac{G_n}{G_n^c} + \frac{G_s}{G_s^c} = 1 \tag{5.14}$$

Where G_n and G_s correspond to the normal and shear fracture toughness (dissipated energy), respectively.

Mechanical properties used to model the adhesive (Araldite 420) for the quasi-static tests in the present work were previously characterized by Braga [9] and are shown in Table 5.3. Young's modulus (*E*) and tensile strength σ_u were obtained by performing bulk tensile tests, shear strength (*G*) and shear stress τ_u were measured through adherent shear tests (TAST), fracture toughness in mode I (G_I^c) was obtained in double cantilever beam (DCB) test and fracture toughness in mode II (G_{II}^c) estimated numerical in end notch flexure (ENF) tests. It is possible to notice that mechanical properties change substantially depending on the cure employed.

Table 5.3: Araldite 420 mechanical properties, adapted from [9].

Cure Temperature	*E* [GPa]	*G* [MPa]	σ_u [MPa]	τ_u [MPa]	G_I^c [N/mm]	G_{II}^c [N/mm]
Room Temperature	1.57	600	30	22.5	3	9
120ºC	1.73	665	40	28	3	9

For the mechanical properties used in the impact test, tensile strength was taken from Figure 4.3 from section 4.2. Shear strength, for numerical purposes, was considered to be proportional to the relation between tensile strength and shear strength at lower strains, for 120 °C (1.43 relation was used).

5.3 Overlap joints modelling

The finite element analysis was performed using the ABAQUS® software package. Models for the FSW, Hybrid and adhesive bonded with 40 mm and 12.5 mm overlap joints were made. Analysis of the models were done using the explicit method. Comparatively to the implicit method, the explicit one can be faster to calculate each increment since it advances the kinematic state based on the previous one, which allows the computation to be less intense. However, size of the increment needs to be sufficiently small so that errors are not allowed to grow, since this method continuous to increment whether the equilibrium conditions are fulfilled or not, which can lead to incorrect results. Time increment in the ABAQUS dynamic explicit method is governed by the smaller element present in the mesh. This method can be used for both quasi-static and dynamic simulations, as long as that for quasi-static simulations the kinematic energy corresponds to less than 5% of the internal energy in the all system [106].

For the aluminium, the material Young's modulus (69 GPa) and Poisson's ratio (0.33) were entered, as well as mass density (2700 kg/cm^3 $\mathrm{kg/cm^3}$, only used for impact simulations). Plastic properties were inputted in a tabular form (Yield stress and plastic strain), based on the isotropic hardening law (Voce law) detailed in section 5.1 and subsection 5.1.1. Values for the GTN $(f_c, f_F, \varepsilon_N, S_N, f_N)$ were entered using the porous metal plasticity option, using the same values mentioned in section 5.1 as well.

For the adhesive, elastic properties were also given (a Young's modulus of 1.73 GPa and a shear modulus of 665 MPa), and quads damage for traction separation was used to implement the cohesive trapezoidal law detailed in section 5.2, with the values mentioned in section 5.2 for σ_u, τ_u, G_I^c and G_{II}^c at 120ºC inputted as well, for the quasi-static-simulation. For the impact simulation, σ_u is computed according to Figure 4.3 (estimative of the strain rate experienced by the adhesive is done by performing the simulation without the damage variable), τ_u is found by considering the same relation between it and σ_u at quasi-static and impact loading (σ_u =1.43τ_u) and the rest of the variables remain the same. Mass density is also given for impact simulations.

In order to improve the accuracy of the numerical models created, size of each material zone in the model was set based on optical microscopy analysis and microhardness measurements (see Figure 4.5, Figure 4.6 and Figure 4.7). In Figure 5.4 it is possible to see the geometry of the different zones of the FSW and Hybrid joints numerical models. An approximation of the hook defect is also included in the models by adding a zero-thickness defect (non-connected elements) feature, due to the high impact that this geometry has in the joint's performance.

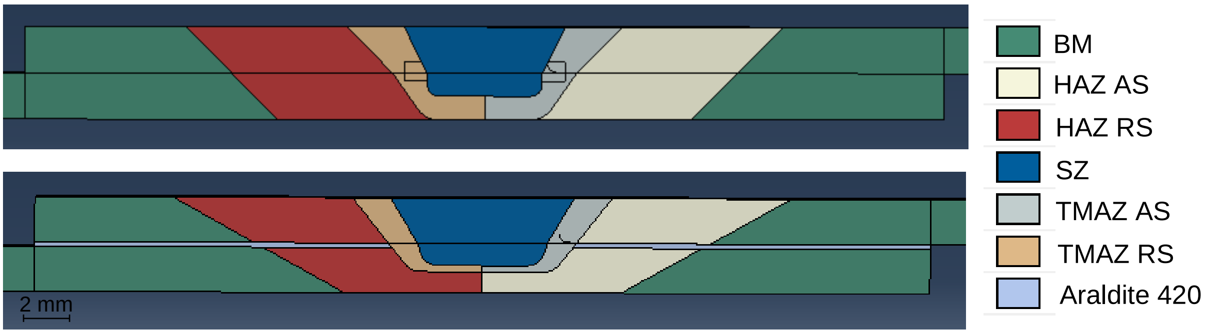

Figure 5.4: Representation of the different zones of the FSW and Hybrid numerical models, respectively.

To numerically reproduce the real experiment conditions, some boundary conditions needed to be defined (Figure 5.5). For the bottom sheet of the joint a restrain type boundary condition was introduced, whereas for the top plate it was set either a displacement or a predefined velocity field along the loading axis, depending on if the simulation was for quasi-static or impact events, respectively. An additional condition of symmetry along the loading axis was also defined, so that computational effort was the lowest possible.

For the impact numerical experiments, an extra mass was added with the predefined velocity field, so that the striker's mass could be taken into account.

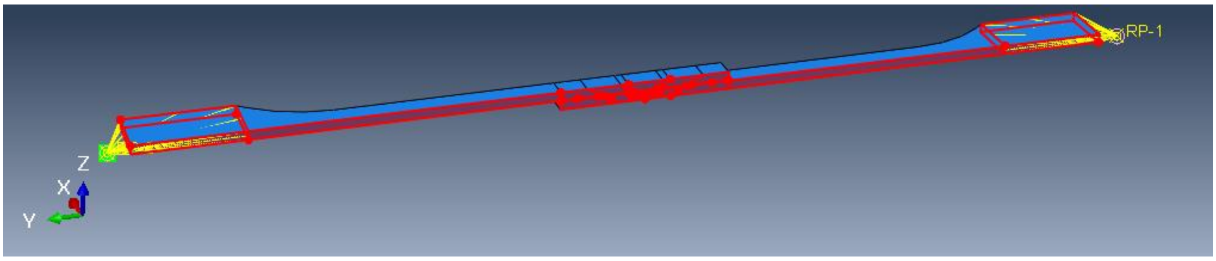

Figure 5.5: Representative boundary conditions and mass element (green) for the impact simulation.

An 8-node three-dimensional cohesive element (COH3D8) was used to define the adhesive, whereas for the remaining zones of the aluminium, continuum three-dimensional 8-node element (C3D8R), with reduced integration and hourglass control were implemented (Figure 5.6).

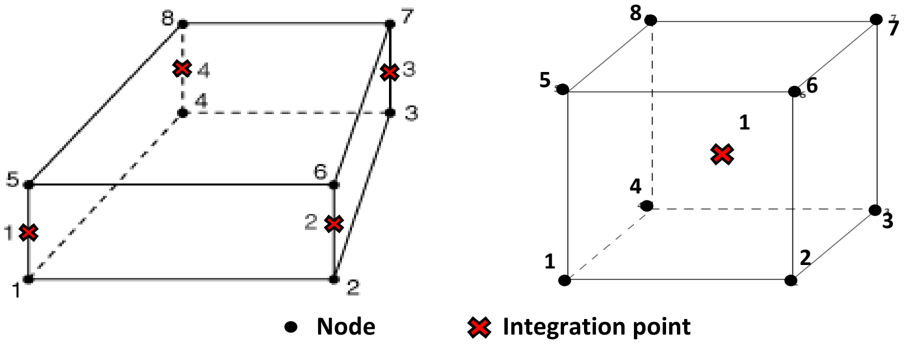

Figure 5.6: Different type of elements used: COH3D8 and C3D8R, respectively.

Meshes for the different models were built with the objective of reducing the computation time without compromising the results. Global element seeds were set to a length of 0.5 mm, whereas for the overlap part, seed edges were used to increase the accuracy in this zone, ranging from .1 mm to 0.4 mm. For the adhesive layer, elements were set with a 0.1 mm length and a 0.2 mm height, so that only 1 element was present in the stack direction of the adhesive.

5.4 AB-12.5 SLJ

Figure 5.7 shows a comparison between the experimental and numerical results obtained for the AB joints with a 12.5 mm overlap.

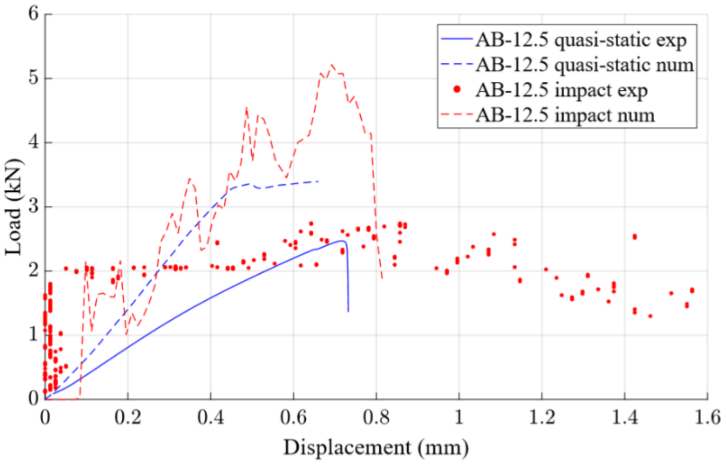

Figure 5.7: Experimental and numerical load displacement curves of the AB-12.5 specimens.

For the quasi-static experiments, numerical model over predict strength of the joint. This result is most likely due to the poor surface treatment verified on these joints, which weakens the bond between the substrate and the adhesive, leading to premature failure. A significant stiffness difference between experimental and numeric is also noticeable since machine compliance is not taken into account.

Ductility is almost the same, although is it possible to see that there is plasticization of the joint in the numerical results, whereas in the experimental one's joint deforms almost only elastic. Adhesive model only accounts for adhesive failure and considers perfect adhesion between the adhesive and the substrate, which may not be completely true in this case. The fact that they have such a close ductility might be due to the slipping that occurred in these tests, as explain in the previous chapter.

For the impact experiments, this time around, joint's strength is overpredicted. This might be either by the influence that the aluminium has at this strain rate, which is not accounted in this, or by the overestimation of the adhesive strength. Ductility is underpredicted, which might indicate that damage model of the adhesive might not be adequate for this strain rate magnitude. Despite all the aspects mentioned, significant noise is present in the experimental curve, which makes it difficult to establish a comparison between experimental and numerical impact tests, being a point to improve.

5.5 AB-40 SLJ

A comparison between the experimental and numerical results obtained for the AB joints with a 40 mm overlap is shown in Figure 5.8. It is possible to see that both numerical curves present a stiffer joint behaviour. Lap joints do not allow the use of conventional clip gauges due to the eccentric load path of the geometry. Due to this, measuring of the displacement was made directly on the cross head of the machine, which may also contribute to the disparity found in the displacement values since the cross-head LVDT used to measure the displacement does not eliminate the slack existent in the machine.

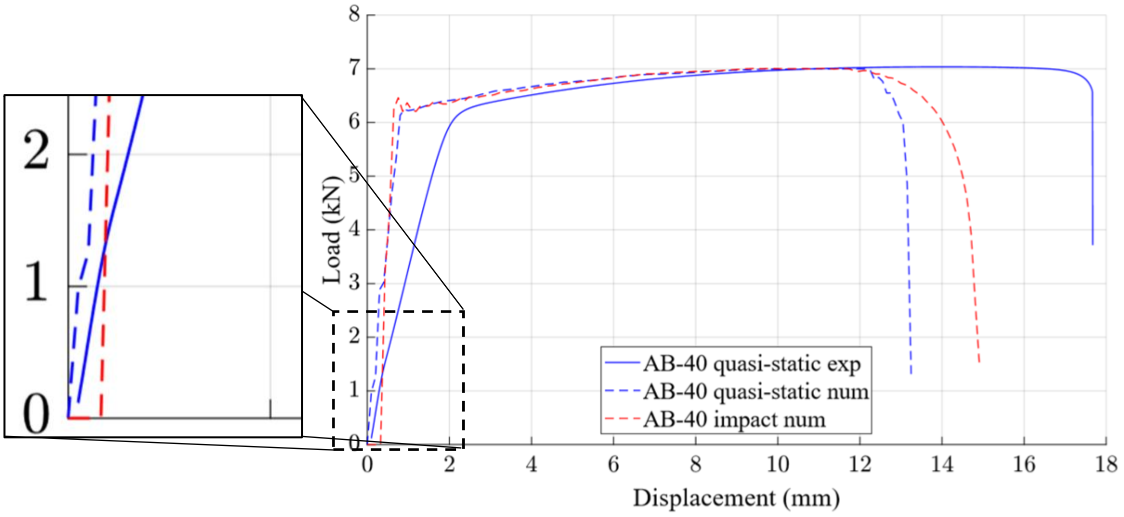

Figure 5.8: Experimental and numerical load displacement curves of the AB-40 specimens.

In the quasi-static experiments, while strength was accurately predicted, ductility of the joint was underpredicted. Ductility of the joint might have been higher experimentally due to the clamping system slipping, which is possible to see in the magnification in Figure 5.8 with the stiffness change. Failure mode was well predicted, with the joint failing in the adherent, away from the overlap. Nevertheless, due to the underprediction mentioned before, aluminium damage model should be reviewed since it was based on the literature [103].

For the impact tests, despite a comparison between experimental and numeric could not be made, since no valid results were obtained for this joint, it is possible to notice in the latter that the ductility of this joint increases with the increase in the strain rate, which was expected due the high ductility characteristic of this type of adhesive.

5.6 FSW SLJ

A comparison between the experimental and numerical results obtained for the FSW joints is shown in Figure 5.9.

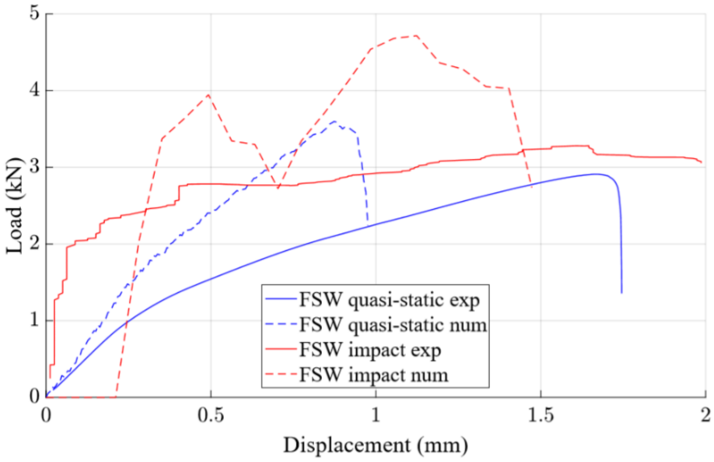

Figure 5.9: Experimental and numerical load displacement curves of the FSW specimens.

Stiffness in simulation is significantly higher than experimentally. Due to lack of laboratory availability it was not possible to repeat the experimental tests which ultimately lead to this accentuated difference, indicating the influence that the slipping of the clamping system has in the results.

For the quasi-static tests, strength in the numerical model is overpredicted, whereas for ductility the opposite happens. There are some aspects that might influence the results, such as the lack of representation of the residual stresses resultant from the welding process, which might influence stress-strain behaviour of the joint, especially in the welding zone were these are higher, or the modelling of the different welded zones as rigidly set when, in reality, the microstructural evolution is gradual between the boundaries. Although this is a reasonable approximation, it shows limitations since there is an abrupt change in the material properties of these zone, leading to stress gradients that push the fracture of the joint to be in these boundary changes.

For the impact tests, significant noise is present in the experimental curve which makes it hard to compare both curves. Despite this, an overprediction and underprediction of the strength and ductility of the joint, respectively, may indicate that this material can be rate sensitive around the range of strains tested.

Fracture in this case was also well predicted for both cases, being initiated in the hook defect (Figure 5.10).

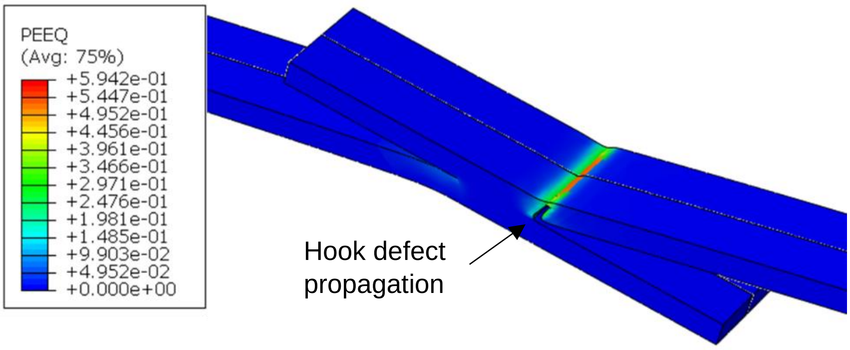

Figure 5.10: Failure location of the FSW joint model for both quasi-static and impact events.

5.6 Hyb SLJ

A comparison between the experimental and numerical results obtained for the Hybrid joints is shown in Figure 5.11.

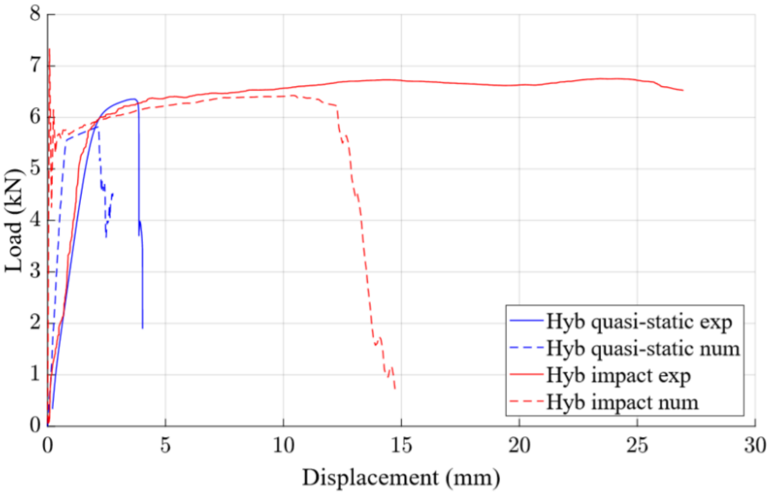

Figure 5.11: Experimental and numerical load displacement curves of the Hybrid specimens.

Quasi-static results show that, although both strength and ductility of the numerical model is lower comparatively to the experimental one, failure type mode is the same: it starts with the majority of the adhesive failing simultaneously, initiated at the tip of the joint, where peeling stresses are higher, and it shortly followed by the failure of the aluminium adherent in the transition zone between HAZ and TMAZ, Figure 5.12 a).

When strain rate is increased, strength prediction of the joint starts to get close from the experimental, even though change in strength between the different rates is not significative, and two types of failure are obtained. For velocities up to 6 m/s, joint failure is similar to the quasi-static failure, with the adhesive failing first and the aluminium failing shortly after, whereas for velocities above 9 m/s failure of the joint is similar to the adhesive bonded joint, which occurs in the adherent, away from the overlap (Figure 5.12 b)). This may indicate that a transition in the adhesive behaviour occurs around these velocities. Ductility in this case is underpredicted, which might indicate that a study to characterize adhesive fracture at high strain rates should be done in the future, similarly to the one done in [9] for quasi-static.

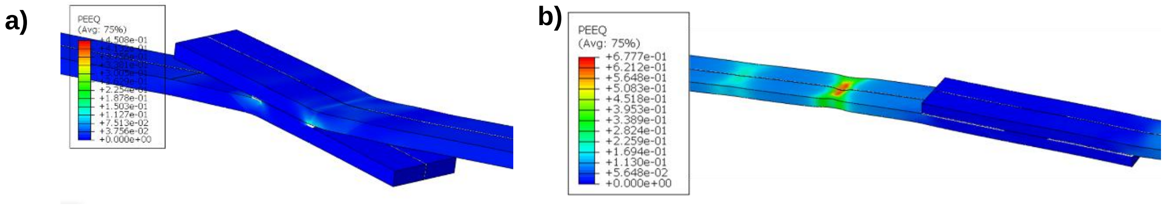

Figure 5.12: Hybrid joint model failure: a) in quasi-static and b) for impact velocities above 9m/s .

When comparing Hybrid and FSW simulations, similar conclusion to the experimental tests can be withdrawn, Figure 5.13. Adhesive addition to the FSW process substantially improves strength and ductility of the joint, and the effect of the hook defect, which is the main cause of premature failure of the FSW joints, starts to get less evident.

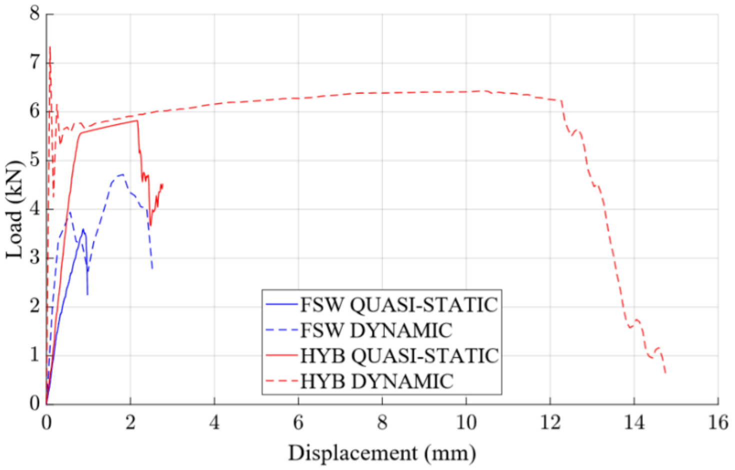

Figure 5.13: Experimental and numerical load displacement curves of the FSW and Hybrid specimens.

Chapter 6

Conclusions and Future Works

6.1 Concluding Remarks

The main objectives proposed for this Master thesis were to study and benchmark FSW, AB and FSWB under quasi-static and impact loading, and to perform numerical analyses of each joint for the same loading conditions.

Regarding the static strength, lap shear strength tests were made so that static mechanical properties of the 3 type of joints could be obtained and compared. It was found out that Hybrid joints performed consistently better than the FSW only joints, with an average joint efficiency of 89.5% comparatively to the 40.1% in the FSW ones. Although in both joints, recrystallization of the base material and introduction of crack-like defects occur, it effects FSW only joints to a bigger extent. Microscopy analysis allowed to confirm that the interface defects found in FSW joints seemed to be covered with adhesive in the Hybrid joints. As a result, the adhesive layer present in the Hybrid joints allows for a better stress distribution and diminishes the impact of the defects, resulting in a higher fracture strength and ductility. Nevertheless, fracture of both joints occurs through the hook defect, with the Hybrid joints fracture starting from the edge of the adhesive. Despite the aforementioned improvement, static mechanical performance of Hybrid joints is still short when compared to the AB joints with a 40 mm overlap, with the best performing joint achieving a 102.4% joint efficiency. The continuous layer of the adhesive present in the AB joints allows an uniformization of the stress distribution, resulting in a fracture through the adherent and, consequently in the joint with the highest strength, ductility and toughness, Smaller 12.5 mm overlap AB joints were also manufactured but failure in these joints was totally adhesive, which resulted in the poorest joint performance (37.3%). By drawing a linear interpolation between these two lengths, it seems that any reduction in the 40 mm overlap will lead to significant decrease in performance of these joints, changing from a through adherent failure to a through adhesive failure.

After gathering the static mechanical properties of the joints, impact tests were further conducted to assess the lap shear strength of the joints at higher strain rates. Valid results for the AB joint were not possible to be obtained, mostly because there was not enough impact energy. AB joint with 12.5 mm, although showing a small increase in average strength, ductility suffered a significant increase (≈100%), which indicates the capability of the adhesive part of the joint of absorbing the energy of the impact. Hybrid joints, in this case, where the best performing joints. Although strength increase only by 9%, ductility increased almost 680%, which, once again, shows the capability that the adhesive has in absorbing the energy of the impact and improvement drastically the behaviour of the joint when compared to the FSW joints. Fracture of the Hybrid joints for velocities up to 6 m/s was similar to the quasi-static (started through the adhesive), whereas for velocities above 9 m/s fracture occurred in the adherent. This might indicate that not only a change in the adhesive behaviour happens around these strain rates but also that, with an improvement in the surface treatment, Hybrid joints might have a behaviour closer to the AB joints, always with a lower ductility due to the lower adhesive length present in the joint.

Concerning the numerical analysis, a finite element model of each specimen was made and compared against the experimental results. A general conclusion from this comparison was that aluminium damage model and hardening material laws for the HAZ, TMAZ and SZ zones should be reviewed since they were based from the literature. CZM at impact loading should also be assessed, since only information regarding the adhesive tensile strength at high strain rate was known, which can be the cause for the differences observed between experimental and numeric. The new parameters of the Voce law shown a good correlation for the base material, predicting accurately the base material strength. In general accuracy of the models was not achieved. There are some reasons behind this, which ultimately lead to simplifications used in the models, such as the simplification of the microstructural evolution along the joint, which was rigidly set in this case, or even the omission of the residual stresses introduced with the FSW process. For the Hybrid joints, parameters inputted for the adhesive also were hard to predict because, even though curing occurs at room temperature for these joints, during the FSW process a semi cure occurs, due to the temperatures involved in this process, which might increase the mechanical performance of the adhesive part (less moisture). For impact loadings, FSW and AB-12.5 models presented the most disparities. Experimental curves were with considerable noise, which made hard its comparison. For quasi-static, a better estimation of the curves was achieved. FSW strength overestimation was mainly due to experimental clamping slippage, whereas for the AB-12.5 overestimation could be explained by numerically considering perfect adhesion. For the AB, comparison was only possible at quasi-static loading and the difference was mainly attributed to the aluminium damage model. Hybrid joints were most accurate for impact loadings, with an accurately prediction of strength.

6.2 Future work

Considering that the joining process studied in this project is still relatively new, further research is required to achieve the industrialization of the process. Some of the future works that can be done are:

- Improve the apparatus used to perform the impact experiments in order to reduce scatter of results, which was significant in the current study. Some points to consider are designing of a clamping system to guarantee the correct fixation of the specimens, revision of the acquisition system and addition of a filter to reduce noise in the date and ensuring fracture of the specimen at first impact.
- If conditions described in the point above are fulfilled, studies at high strain rate should be conducted once again. To improve the accuracy and understanding of the strain fields, Digital Image Correlation (DIC) measurements should also be taken simultaneously with the tests.
- A DoE could also be implemented to understand if there are different parameters that improve joints performance at high strain rates, other than the already used ones from the quasi-static experiments.

- Development of more precise FEM models to allow a more realistic prediction of the joint’s behaviour. To accomplish this, material models used in this work should be reviewed and shear strength and fracture toughness in mode I and II adhesive properties at high strain rate should be assessed.
- Expose joints to different environmental conditions and understand the impact it has on the behaviour of the joints when adhesive is present. These conditions could be, for example, humidity or large gradient of temperature, and it would allow to understand the true capability of implement these joints in realistic transportation industry environments.
- Study different surface treatment, including different primers, to improve the adhesion strength in both adhesive bonded and Hybrid joints. A cure at 120ºC for 1 hour, similar to the adhesive bonded joints, should also be implemented in the Hybrid joint to understand the impact it has in the mechanical performance of the joint at high strain rates.
- Study the effect that different post-weld heat treatment temperatures have in the Hybrid joint’s mechanical performance.
- Expand FSWB study to other materials used or suitable to be used in the aeronautic and automotive industries, such as the AA2024, AA5754, AA7075 or the Ti-6Al-4V.
- Feasibility assessment of FSWB in the production of tailor welded blankets to increase the attractiveness of this application for the automotive industry. With this in mind, combination of adhesive with FSSW could also be interesting to study.

References

[1] U.S. Department Of Energy (2015) Quadrennial Technology Review: An Assessment of Energy Technologies and Research Opportunities. *Quadrennial Technology Review*. (September), 1–505.

[2] Heuss, R., Müller, N., van Sintern, W., Starke, A., and Tschiesner, A. (2012) Advanced Industries: Lightweight, heavy impact. .

[3] Smith, Brett, Adela Spulber, Shashank Modi, and T.F. (2017) Technology Roadmaps: Intelligent Mobility Technology, Materials and Manufacturing Processes, and Light Duty Vehicle Propulsion. .

[4] Mishra, R.S. and Ma, Z.Y. (2005) Friction stir welding and processing. *Materials Science and Engineering R: Reports*. 50 (1–2), 1–78.

[5] Thomas, M.W. (1991) Friction Stir Butt Welding, International Patent Application PCT/GB92/02203 and G.B. Patent Application 9125978.8, 1991.

[6] Liu, X.C., Sun, Y.F., Morisada, Y., and Fujii, H. (2018) Dynamics of rotational flow in friction stir welding of aluminium alloys. *Journal of Materials Processing Technology*. 252 643–651.

[7] Nandan, R., DebRoy, T., and Bhadeshia, H.K.D.H. (2008) Recent advances in friction-stir welding - Process, weldment structure and properties. *Progress in Materials Science*. 53 (6), 980–1023.

[8] Jene, T, Dobmann, G, Wagner, G, Eifl er, D. (2008) Monitoring of the Friction Stir Welding process to descrive parameter effects on joint quality. *Welding in the World*. 52 (9–10), 47–53.

[9] Braga, D.F.O. (2018) Innovative structural joining for lightweight design, MIT-Portugal, FEUP, 2018.

[10] Fujii, H., Maeda, M., and Nogi, K. (2003) Tensile properties and fracture locations of friction-stir welded joints of 6061-T6 aluminum alloy. *Journal of Materials Science Letters*. 22 1061–1063.

[11] Liu, H.J., Maeda, M., Fujii, H., and Nogi, K. (2003) Tensile properties and fracture locations of friction-stir welded joints of 1050-H24 aluminum alloy. *Journal of Materials Science Letters*. 22 41–43.

[12] Liu, H.J., Fujii, H., Maeda, M., and Nogi, K. (2003) Tensile properties and fracture locations of friction-stir-welded joints of 2017-T351 aluminum alloy. *Journal of Materials Processing Technology*. 142 (3), 692–696.

[13] Maeda, M., Liu, H., Fujii, H., and Shibayanagi, T. (2005) Temperature field in the vicinity of FSW-tool during friction stir welding of aluminium alloys. *Welding in the World*. 49 (3–4), 69–75.

[14] Wu, T., Zhao, F., Luo, H., Wang, H., and Li, Y. (2019) Temperature monitoring and material flow characteristics of friction stir welded 2A14-t6 aerospace aluminum alloy. *Materials*. 12 (20),.

[15] Schneider, J.A., Nunes, A.C., Chen, P.S., and Steele, G. (2005) TEM study of the FSW nugget in AA2195-T81. *Journal of Materials Science*. 40 (16), 4341–4345.

[16] Murr, L.E., Liu, G., and Mcclure, J.C. (1998) A TEM study of precipitation and related microstructures in friction-stir-welded 6061 aluminium. *Journal of Materials Science*. 33 (5),

1243–1251.

[17] Colligan, K. (1999) Material flow behavior during friction stir welding of aluminum. *Welding Journal (Miami, Fla)*. 78 (7), 229-s.

[18] Huang, Y., Wang, Y., Wan, L., Liu, H., Shen, J., dos Santos, J.F., et al. (2016) Material-flow behavior during friction-stir welding of 6082-T6 aluminum alloy. *International Journal of Advanced Manufacturing Technology*. 87 (1–4), 1115–1123.

[19] Guerra, M., Schmidt, C., McClure, J.C., Murr, L.E., and Nunes, A.C. (2002) Flow patterns during friction stir welding. *Materials Characterization*. 49 (2), 95–101.

[20] Krasnowski, K., Hamilton, C., and Dymek, S. (2015) Influence of the tool shape and weld configuration on microstructure and mechanical properties of the Al 6082 alloy FSW joints. *Archives of Civil and Mechanical Engineering*. 15 (1), 133–141.

[21] Richter-Trummer, V., Suzano, E., Beltrão, M., Roos, A., dos Santos, J.F., and de Castro, P.M.S.T. (2012) Influence of the FSW clamping force on the final distortion and residual stress field. *Materials Science and Engineering A*. 538 81–88.

[22] Jauhari Tahir Khairuddin, Jamaluddin Abdullah, Z.H. and I.P.A. (2012) Principles and Thermo-Mechanical Model of Friction Stir Welding. in: Weld. Process. Dr. Rad. Kovacevic, pp. 191–216.

[23] A. K. Lakshminarayanan, V.B. (2008) Process parameters optimization for friction stir welding of RDE-40 aluminium alloy using Taguchi technique. *Transactions of Nonferrous Metals Society of China*. 18 548–554.

[24] Sreenivas, P., Anil Kumar, R., and Sreejith, P.S. (2017) Effect of applied axial force on FSW of AA 6082 - T6 aluminium alloys. *International Journal of Mechanical Engineering and Technology*. 8 (1), 88–99.

[25] Prasad, M.V.R.D. and Kumar Namala, K. (2018) Process Parameters Optimization in Friction Stir Welding by ANOVA. *Materials Today: Proceedings*. 5 (2), 4824–4831.

[26] Verma, S., Gupta, M., and Misra, J.P. (2019) Effect of pin-profiles on thermal cycle, mechanical and metallurgical properties of friction stir–welded aviation-grade aluminum alloy. *Proceedings of the Institution of Mechanical Engineers, Part B: Journal of Engineering Manufacture*.

[27] Elangovan, K. and Balasubramanian, V. (2008) Influences of tool pin profile and welding speed on the formation of friction stir processing zone in AA2219 aluminium alloy. *Journal of Materials Processing Technology*. 200 (1–3), 163–175.

[28] Zhang, Y.N., Cao, X., Larose, S., and Wanjara, P. (2012) Review of tools for friction stir welding and processing. *Canadian Metallurgical Quarterly*. 51 (3), 250–261.

[29] Lumley, R.N. (2010) Fundamentals of aluminium metallurgy: Production, processing and applications. .

[30] Threadgill, P.L., Leonard, A.J., Shercliff, H.R., and Withers, P.J. (2013) Friction stir welding of aluminium alloys. 1718 (August), 49–93.

[31] Ji, S., Meng, X., Zeng, Y., Ma, L., and Gao, S. (2016) New technique for eliminating keyhole by active-passive filling friction stir repairing. *Materials and Design*. 97 175–182.

[32] Magalhães, V.M., Leitão, C., and Rodrigues, D.M. (2018) Friction stir welding industrialisation and research status. *Science and Technology of Welding and Joining*. 23 (5), 400–409.

[33] Lohwasser, D. and Chen, Z. (2010) Friction stir welding: From basics to applications. Woodhead Publishing Limited, .

[34] Friction stir welding of airframe structures, https://www.twi-global.com/who-we-are/who-we-work-with/industry-sectors/aerospace/joining-of-airframe-structures/friction-stir-welding-of-airframe-structuresm [2019-12-10].

[35] European Aluminium Association (2013) Applications – Car body – Body components. *The Aluminium Automotive Manual*. 1–24.

[36] 2013 Accord featuring first use of new Honda emissions aftertreatment catalyst and new technology to weld together steel and aluminum, https://www.greencarcongress.com/2012/09/accord-20120906.html, [2019-12-12].

[37] Apple slims down iMac 40% with “friction-stir welding” & ditching the disc drive, https://appleinsider.com/articles/12/10/24/apple-slims-down-imac-40-with-friction-stir-welding-ditching-the-disc-drive, [2020-03-13].

[38] Banea, M.D. and Da Silva, L.F.M. (2009) Adhesively bonded joints in composite materials: An overview. *Proceedings of the Institution of Mechanical Engineers, Part L: Journal of Materials: Design and Applications*. 223 (1), 1–18.

[39] Weitzenböck, J.R. and McGeorge, D. (2011) Science and Tecknology of Bolt-Adhesive Joints. *Advanced Structured Materials*. 5 (March), 23–49.

[40] da Silva, L.F.M., Öchsner, A., and Adams, R.D. (2018) Handbook of Adhesion Technology. Second Edi Springer Reference, .

[41] Gardiner, G., Is the BMW 7 Series the future of autocomposites?, https://www.compositesworld.com/articles/is-the-bmw-7-series-the-future-of-autocomposites, [2019-11-10].

[42] Alexander, R., Understanding Adhesive Failures, http://tombrowninc.com/blog/understanding-adhesive-failures/, [2019-11-16].

[43] Rudawska, A. (2019) The influence of curing conditions on the strength of adhesive joints. *The Journal of Adhesion*. 0 (0), 1–21.

[44] Harris, J.A. and Adams, R.D. (1985) An assessment of the impact performance of bonded joints for use in high energy absorbing structures. *Proceedings of the Institution of Mechanical Engineers, Part C: Journal of Mechanical Engineering Science*. 199 (2), 121–131.

[45] Yokoyama, T. and Nakai, K. (2015) Determination of the impact tensile strength of structural adhesive butt joints with a modified split Hopkinson pressure bar. *International Journal of Adhesion and Adhesives*. 56 13–23.

[46] Goglio, L. and Rossetto, M. (2008) Impact rupture of structural adhesive joints under different stress combinations. *International Journal of Impact Engineering*. 35 (7), 635–643.

[47] Goda, Y. and Sawa, T. (2011) Study on the effect of strain rate of adhesive material on the stress state in adhesive joints. *Journal of Adhesion*. 87 (7–8), 766–779.

[48] Yildiz, S., Andreopoulos, Y., and Delale, F. (2019) Mode I characterization of toughened epoxy adhesive joints under shock-wave loading. *International Journal of Adhesion and Adhesives*. 90 (February), 71–87.

[49] Silva, M.R.G., Marques, E.A.S., and da Silva, L.F.M. (2016) Behaviour under impact of mixed adhesive joints for the automotive industry. *Latin American Journal of Solids and Structures*. 13 (5), 835–853.

[50] Jeenjitkaew, C., Luklinska, Z., and Guild, F. (2010) Morphology and surface chemistry of kissing bonds in adhesive joints produced by surface contamination. *International Journal of Adhesion and Adhesives*. 30 (7), 643–653.

[51] Correia, S., Anes, V., and Reis, L. (2018) Effect of surface treatment on adhesively bonded aluminium-aluminium joints regarding aeronautical structures. *Engineering Failure Analysis*. 84 (October 2017), 34–45.

[52] da Silva, L.F.M., Ochsner, A., and Pirondi, A. (2011) Hybrid Adhesive Joints. .

[53] Kelly, G. (2006) Quasi-static strength and fatigue life of hybrid (bonded/bolted) composite single-lap joints. *Composite Structures*. 72 (1), 119–129.

[54] Kweon, J.H., Jung, J.W., Kim, T.H., Choi, J.H., and Kim, D.H. (2006) Failure of carbon composite-to-aluminum joints with combined mechanical fastening and adhesive bonding. *Composite Structures*. 75 (1–4), 192–198.

[55] European Aluminium Association (2015) EAA Aluminium Automotive Manual – Joining - Hybrid joining techniques. *The Aluminium Automotive Manual*. 1–18.

[56] Sadowski, T., Golewski, P., and Zarzeka-Raczkowska, E. (2011) Damage and failure processes of hybrid joints: Adhesive bonded aluminium plates reinforced by rivets. *Computational Materials Science*. 50 (4), 1256–1262.

[57] European Aluminium Association (2013) Application of car body structure. *The Aluminium Automotive Manual*. 6 (2011), 1–84.

[58] Sadowski, T., Balawender, T., Śliwa, R., Golewskp, P., and Kneć, M. (2013) Modern hybrid joints in aerospace: Modelling and testing. *Archives of Metallurgy and Materials*. 58 (1), 163–169.

[59] AN aircrafts - AN-24, https://www.antonov.com/en/history/an-24, [2019-11-18].

[60] Singh, S. and Misra, J.P. (2017) WELD-BONDING A STATE OF ART REVIEW. in: 3rd Int. Conf. Recent Develpment Eng. Sci. Humanit. Manag., Chandigarhpp. 118–126.

[61] Messler, R.W. (2004) Joining of Materials and Structures: From Pragmatic Process to Enabling Technology. Elsevier Butterworth–Heinemann, .

[62] Hayat, F. (2011) Comparing Properties of Adhesive Bonding, Resistance Spot Welding, and Adhesive Weld Bonding of Coated and Uncoated DP 600 Steel. *Journal of Iron and Steel Research International*. 18 (9), 70–78.

[63] Gaul, H. and Weber, G. (2011) Technology of Weld-Adhesive Joints. in: Adv. Struct. Mater., Springer, pp. 37–77.

[64] Moroni, F., Pirondi, A., and Kleiner, F. (2010) Experimental analysis and comparison of the strength of simple and hybrid structural joints. *International Journal of Adhesion and Adhesives*. 30 (5), 367–379.

[65] Jiang, J. and Zhang, Z. (2008) The study on the plasma arc weld bonding process of magnesium alloy. *Journal of Alloys and Compounds*. 466 (1–2), 368–372.

[66] Wang, H.Y., Liu, L.M., Zhu, M.L., and Wang, H. (2007) Laser weld bonding of A6061Al alloy to AZ31B Mg alloy. *Science and Technology of Welding and Joining*. 12 (3), 261–265.

[67] Liu, L. and Ren, D. (2011) A novel weld-bonding hybrid process for joining Mg alloy and Al alloy. *Materials and Design*. 32 (7), 3730–3735.

[68] Peng, D., Liu, Q., Li, G., and Cui, J. (2019) Investigation on hybrid joining of aluminum alloy sheets: magnetic pulse weld bonding. *The International Journal of Advanced Manufacturing Technology*.

[69] Lionetto, F., Balle, F., and Maffezzoli, A. (2017) Hybrid ultrasonic spot welding of aluminum to carbon fiber reinforced epoxy composites. *Journal of Materials Processing Technology*. 247 289–295.

[70] Chowdhury, S.H., Chen, D.L., Bhole, S.D., Cao, X., and Wanjara, P. (2013) Lap shear strength and fatigue behavior of friction stir spot welded dissimilar magnesium-to-aluminum joints with adhesive. *Materials Science and Engineering A*. 562 53–60.

[71] Braga, D.F.O., De Sousa, L.M.C., Infante, V., Da Silva, L.F.M., and Moreira, P.M.G.P. (2015) Aluminium friction-stir weld-bonded joints. *Journal of Adhesion*. 92 (7–9), 665–678.

[72] Braga, D.F.O., Maciel, R., Bergmann, L., da Silva, L.F.M., Infante, V., dos Santos, J.F., et al. (2018) Fatigue performance of hybrid overlap friction stir welding and adhesive bonding of an Al-Mg-Cu alloy. *Fatigue and Fracture of Engineering Materials and Structures*. (June), 1–9.

[73] Yoon, J.W. (2018) Modeling and Simulation of the Forming of Aluminum Sheet Alloys.

Metalworking: Sheet Forming. 14 792–826.

[74] Medlin, H.K. and D., Ed. (2000) ASM Handbook Volume 8: Mechanical Testing and Evaluation. ASM International, .

[75] Field, J.E., Walley, S.M., Proud, W.G., Goldrein, H.T., and Siviour, C.R. (2004) Review of experimental techniques for high rate deformation and shock studies. .

[76] Zhang, X.X., Ruiz, G., and Yu, R.C. (2008) A new drop weight impact machine for studying the fracture behaviour of structural concrete. *WIT Transactions on the Built Environment*. 98 (December 2014), 251–259.

[77] Mott, P.H., Twigg, J.N., Roland, D.F., Schrader, H.S., Pathak, J.A., and Roland, C.M. (2007) High-speed tensile test instrument. *Review of Scientific Instruments*. 78 (4),.

[78] Kleiner, M., Tekkaya, A.E., Demir, O.K., Risch, D., and Psyk, V. (2009) A drop-weight high-speed tensile testing instrument. *Production Engineering*. 3 (2), 175–180.

[79] Hopkinson, J. (1872) On the rupture of iron wire by a blow. *Proc. Literary and Philosophical Society of Manchester*. 11 40–45.

[80] Hopkinson, B. (1914) A Method of Measuring the Pressure Produced in the Detonation of High Explosives or by the Impact of Bullets. *Philosophical Transactions of the Royal Society of London*. 213 437–456.

[81] H. Kolsky (1949) An Investigation of the Mechanical Properties of Materials at very High Rates of Loading. *Proceedings of the Physical Society. Section B*. 676–700.

[82] Lindholm, U.S. and Yeakley, L.M. (1968) High strain-rate testing: Tension and compression. *Experimental Mechanics*. 8 (1), 1–9.

[83] Nicholas, T. (1981) Tensile testing of materials at high rates of strain. *Experimental Mechanics*. 21 (5), 177–185.

[84] Staab, G.H. and Gilat, A. (1991) A direct-tension split Hopkinson bar for high strain-rate testing. *Experimental Mechanics*. 31 (3), 232–235.

[85] Silva, C.M.A., Rosa, P.A.R., and Martins, P.A.F. (2009) An innovative electromagnetic compressive split Hopkinson bar. 281–288.

[86] Silva, C.M.A., Rosa, P.A.R., and Martins, P.A.F. (2012) Electromagnetic Cam Driven Compression Testing Equipment. *Experimental Mechanics*. 52 (8), 1211–1222.

[87] Prabhukhot, A.R. and Prasad, K. (2015) Effect of Heat Treatment on Hardness of 6082-T6 Aluminium Alloy. *International Journal of Scientific & Engineering Research*. 6 (12), 38–42.

[88] Matweb, http://www.matweb.com/search/DataSheet.aspx?MatGUID=fad29be6e64d4e95a241690f1f6e1eb7&ckck=1, [2019-09-10].

[89] Makeitfrom, https://www.makeitfrom.com/material-properties/6082-T6-Aluminum, [2019-09-10].

[90] Spacematdb, www.spacematdb.com/spacemat/manudatasheets/araldite-420-tds-v1.pdf, [2019-09-10].

[91] Heatcon, https://www.heatcon.com/wp-content/uploads/2015/08/HCS2407_AC-130-TDS.pdf, [2019-09-10].

[92] Bento, T. (2018) Smart Hybrid Friction Stir Welded Joints for Aerospace Design Applications, 2018.

[93] Santos, T. and Vilaça, P. (2008) Ferramenta Não Consumível Modular Ajustável e Refrigerável para Soldadura e Processamento por Fricção Linear, Patente N^{o}104072, 2008. (in Portuguese)

[94] ASTM (2010) Standard Guide for Preparation for Aluminum Surfaces for Structural Adhesives Bonding (Phosphoric Acid Anodizing). D3933-98 (Reapproved), 1–5.

[95] Shamchi, S.P., Queirós de Melo, F.J.M., Tavares, P.J., and Moreira, P.M.G.P. (2019) Thermomechanical characterization of Alclad AA2024-T3 aluminum alloy using split Hopkinson tension bar. *Mechanics of Materials*. 139 (September), 103198.

[96] Gama, B.A., Lopatnikov, S.L., and Gillespie, J.W. (2004) Hopkinson bar experimental technique: A critical review. *Applied Mechanics Reviews*. 57 (1–6), 223–250.

[97] Chen, X., Peng, Y., Peng, S., Yao, S., Chen, C., and Xu, P. (2017) Flow and fracture behavior of aluminum alloy 6082-T6 at different tensile strain rates and triaxialities. *PLoS ONE*. 12 (7), 1–28.

[98] Krasnowski, K. (2014) Fatigue and static properties of friction stir welded aluminium alloy 6082 lap joints using triflute-type and smooth tool. *Archives of Metallurgy and Materials*. 59 (1), 157–162.

[99] Mishra, R.S., Mahoney, M.W., and Company, R.S. (2007) Friction Stir Welding and Processing. .

[100] Moreira, P.M.G.P., Santos, T., Tavares, S.M.O., Richter-Trummer, V., Vilaça, P., and de Castro, P.M.S.T. (2009) Mechanical and metallurgical characterization of friction stir welding joints of AA6061-T6 with AA6082-T6. *Materials and Design*. 30 (1), 180–187.

[101] Gurson, A.L. (1977) Continuum theory of ductile rupture by void nucleation and growth. *Journal of Engineering Materials and Technology*. 99 (76), 2–15.

[102] Tvergaard, V. and Needleman, A. (1984) Analysis of the cup-cone fracture in a round tensile bar. *Acta Metallurgica*. 32 (1), 157–169.

[103] Hval, M., Thaulow, C., Lange, J.H., Høydal, S.H., and Zhang, Z.L. (1998) Numerical modeling of ductile fracture behavior in aluminum weldments. *Welding Journal (Miami, Fla)*. 77 (6), 208-s-217-s.

[104] Da Silva, L.F.M. and Campilho, R.D.S.G. (2012) Advances in Numerical Modeling of Adhesive Joints. Springer, .

[105] Fernandes, R.L. and Campilho, R.D.S.G. (2017) Testing different cohesive law shapes to predict damage growth in bonded joints loaded in pure tension. *Journal of Adhesion*. 93 (1–2), 57–76.

[106] Inc, A. (2005) Abaqus Lecture 5 - Quasi-static analysis.